12-2016

Speleogenesis and Delineation of Megaporosity and Karst Geohazards Through Geologic Cave Mapping and LiDAR Analyses Associated with Infrastructure in Culberson County, Texas

Jon T. Ehrhart
Stephen F. Austin State University, jontehrhart@gmail.com

Speleogenesis and Delineation of Megaporosity and Karst Geohazards Through Geologic Cave Mapping and LiDAR Analyses Associated with Infrastructure in Culberson County, Texas

Speleogenesis and Delineation of Megaporosity and Karst Geohazards Through Geologic Cave Mapping and LiDAR Analyses Associated with Infrastructure in Culberson County, Texas

By

Jon Ehrhart, B.S.

Presented to the Faculty of the Graduate School of

Stephen F. Austin State University

In Partial Fulfillment

Of the requirements

For the Degree of

Master of Science

STEPHEN F. AUSTIN STATE UNIVERSITY

(December 2016)

Speleogenesis and Delineation of Megaporosity and Karst Geohazards Through Geologic Cave Mapping and LiDAR Analyses Associated with Infrastructure in Culberson County, Texas

By

Jon Ehrhart, B.S.

APPROVED:

_____
Dr. Kevin Stafford, Thesis Director

_____
Dr. Wesley Brown, Committee Member

_____
Dr. Melinda Faulkner, Committee Member

_____
Dr. Joseph Musser, Committee Member

_____
Richard Berry, D.M.A.
Dean of the Graduate School

ABSTRACT

The Gypsum Plain region of the Delaware Basin hosts approximately 1800 km^2 of the Castile Formation outcrop. A myriad of karstic developments from closed sinkholes to large multi-kilometer cave systems have been documented within the region. Karst studies on the distribution and speleogenetic evolution within Castile strata began within the last decade with ever increasing data resolution. In this study, a combination of both physical field surveys and analyses of high resolution (~30 cm accuracy) LiDAR data was used to create a theoretical model for karst development across the region. This idealized model considers speleogenetic formation type variations (hypogene and epigene), the density of karstic features based on lithology variations, and the connection between the local hydrostratigraphic setting and the regional hydrogeological framework. Field studies included physical mapping of 20 km^2 of the Gypsum Plain from the Castile's western outcrop to where it dips into the subsurface to the east. These surface surveys involved the recording of all surfically-expressed karstic phenomena and the mapping of all enterable caves so that the speleogenetic evolution could be analyzed. The way in which hypogene and epigene caves are surfically expressed across the region indicates that many of the caves have been affected by either multi-stage epigenetic development or multi-stage hypogenetic development with epigenetic overprinting. Through the use of the methods outlined above, surficial karst manifestations vary across the region, from hypogenetic exposures in the west and epigenetic phreatic / vadose exposures in the east. Additionally, supplementary LiDAR data was used to create digital elevation models (DEM) so that the effectiveness of physical field surveys versus remote sensing techniques could be determined. Previous works in the area by

Stafford et al., (2008b) determined that remote sensing preserved only 36% of all karstic features found through physical field surveys. Given today's advancements in remote sensing accuracy, this study determined that on average LiDAR analysis identifies almost seven times more karstic features than physical surveys over a given area.

ACKNOWLEDGEMENTS

I would first like to thank my thesis advisor Dr. Kevin W. Stafford whose office was always open and who truly went above and beyond to help me complete this research. I want to thank you for your excellent guidance and providing me with the opportunity to work with you at Stephen F. Austin State University. In addition, I would like to thank the Texas Department of Transportation and the Department of Geology at Stephen F. Austin State University for their support and funding of this research. I would like to acknowledge all of those who helped with field work and keeping me sane during late nights in the office: Aaron Eaves, Ashley Landers, Adam Majzoub, Lillian O'Shay, Jessica Shields, Nikota Welch, and Ingrid Eckhoff. You have all made my time here at SFA much more enjoyable and not only do you make good field assistants but great friends as well, thank you! No list of acknowledgments would be complete without mentioning my parents Janice and Rick Ehrhart who have always supported me in all that I do. I would not be where I am today without your wise counsel and unending encouragement.

TABLE OF CONTENTS

ABSTRACT …… i

ACKNOWLEDGEMENTS …… iii

TABLE OF CONTENTS ……..... iv

LIST OF FIGURES ……. vi

PREFACE…….…… xi

SPELEOGENETIC MODEL OF EVAPORITE KARST OCCURRENCES OF THE GYPSUM PLAIN UTILIZING KARST MAPPING AND LIDAR ANALYSES IN CULBERSON COUNTY, TEXAS, USA …… 1

- ABSTRACT ……. 1
- INTRODUCTION……... 3
  - STUDY AREA……...……..4
  - GEOLOGIC SETTING…….……. 6
- METHODOLOGY…… 9
- KARST MORPHOLOGY ……. 11
  - EPIGENE KARST …….. 11
  - HYPOGENE KARST…….……...15
- SPELEOGENETIC MODEL OF THE GYPSUM PLAIN…….....20
- CONCLUSIONS……25
- ACKNOWLEDGEMENTS……...28
- REFERENCES ..……..29

APPENDIX (A) DETAILED LITERATURE REVIEW ……..31

- LOCATION ……..……..……..32
- GEOLOGIC SETTING & BASIN EVOLUTION…….35

GUADALUPIAN SERIES STRATIGRAPHY…….54
OCHOAN SERIES STRATIGRAPHY…….62
KARST AND SPELEOLOGY ……..…….……..66
GIS LIDAR ……..…….……75
REFERENCES ……..78
APPENDIX (B) DETAILED METHODOLOGY…….83
KARST SURVEY……..84
GIS LiDAR AND DEM……90
REFERENCES ..……..……..107
APPENDIX (C) CAVE AND KARST INVENTORY ……...108
CAVE MAP DESCRIPTIONS……109
VITA ……..148

LIST OF FIGURES

Figure 1: Regional map displaying the generalized location of Permian strata outcrops within the Gypsum Plain (Modified from Stafford et al., 2008a) …….5

Figure 2: Stratigraphic section from the Shelf (North) to Delaware Basin (South) of lithologic units within the study area (adapted from Scholle et al., 2004) …….……..7

Figure 3: Cave maps that represent the epigene vadose (Nikad & JC Gypsum Hole), epigene phreatic (Lillcher & Death Tube), and hypogene (Wiggley & Fissure) developments that were surveyed across the study area in both plan and profile views. ……...13

Figure 4: Epigenetic and Hypogenetic morphological features found throughout the study area: A) Large hypogene dome (Fissure Cave); B) Soil suffosion chamber (Upper Death Tube Cave); C) Brecciated zone (Breccia Pipe); D) Phreatic tube overprinted by entrenchment (Lillcher Cave); E) Lower dome structures in relict passage (Fissure Cave); F) Epigene vadose entrenchment (JC) Gypsum Hole Cave); G) Elliptical phreatic tube (Death Tube Cave) …….……..17

Figure 5: Idealized model of karst development across the Gypsum Plain (Pbc = Bell Canyon Formation, Pcs = Castile Formation, Pru = Rustler Formation, Qal = Quaternary Alluvium): Top graph displays the frequency of surface karst manifestations per square kilometer identified by surface walks (red) and LiDAR analyses (blue); Middle diagram displays the cross-sectional relationship between Castile Formation and its bounding formations. Lower diagrams display a representation of the variability in karst development type (ie. hypogene /epigene) across the study area. ……..22

Figure 6: LiDAR analyses. A) discrepancies in karst manifestation identification of surface walks (green stars) and LiDAR analyses (red); B) LiDAR and DEM analyses enhance identification of depressions surrounded by dense vegetation (small isolated depressions in red).; C) 3D view of LiDAR point cloud data of the entrances into Lillcher Cave with simplified cave map from survey data (orange) (vertical exaggeration is 2X). ……..27

LIST OF APPENDIX FIGURES

Figure A1: Physiographic regions of Texas. ……..32

Figure A2: Location of the study area and Castile / Rustler formation outcrops (Stafford et al., 2008a) …….34

Figure A3: Major sedimentary basins within west Texas and southern New Mexico. ……35

Figure A4: Displays the location of the Transcontinental Arch during the late Cambrian ……...36

Figure A5: Displays the shallow Early Ordovician Sea and subsequent deposition of the Ellenberger Formation ……37

Figure A6: Theoretical view of the Oauchita thrust front during the Early Permian (www2.nau.edu) ……40

Figure A7: Delaware / Tobosa basin with associated channels and uplifts (Adams, 1965)……...43

Figure A8: Delaware Basin cross section with lithologic units (Scholle et al., 2004) …….46

Figure A9: Laminated Varves of the Castile formation (Scholle et al., 2004) …….48

Figure A10: Paleotectonic map of western North America from late Jurassic to late Cretaceous; showing the position of the trough, Delaware Basin, and Farallon thrusting (Dickinson, 1981) ……...52

Figure A11: Stratigraphic section from the Shelf (North) to Delaware Basin (South) of lithologic units within the study area (adapted from Scholle et al., 2004) ……54

Figure A12: Illustrating sediment flow into the Delaware Basin during a LST (sepmstrata.org) ……..59

Figure A13: Illustrating the spatial distribution of karstic depressions derived from GIS analysis (Stafford et al., 2008b) …….…..70

Figure A14: Typical ceiling cupola in a series of domal ceiling features. (black bar is 1 meter) (Dead Bunny Hole, Culberson Co. TX) (Stafford et al., 2008a) ……..71

Figure A15: Diagram illustrating the process in which blanket-dissolution breccias form through the dissolution of halite where arrows represent fluid movement (Stafford, 2015) …..…72

Figure A16: Diagram illustrating the process in which breccia pipes form through the dissolution of halite where arrows represent fluid movement (Stafford, 2015) …….……73

Figure A17: Photograph taken in road cut off of highway RM652 displaying a fragmented calcitized zone of the Castile Formation that is likely a result of a breccia pipe. ……73

Figure A18: Diagram illustrating the process in which multi-return LiDAR is obtained (ucanr.edu) ……76

Figure B1: Raw plan view of a field sketch of a central chamber in Lillcher Cave ……85

Figure B2: Walls cave software showing data input panel and output cave skeleton plot in 3D ..86

Figure B3: Walls skeleton plot overlain with digitized drawing of field sketches in XaraXtreme5……...87

Figure B4: Displaying final cave map output of Lillcher Cave……..88

Figure B5: Image of DEM overlain with traverse tracks in blue and karstic features in white…..89

Figure B6: Index map of study area showing LAS grid along RM652 in Culberson County……90

Figure B7: Las Dataset Toolbar options as seen in ArcMap for Desktop V. 10.3.1 ……..92

Figure B8: Sample section of the study area showing the “Point Display” - elevation view and point density (Note: This is only displaying 25% of point cloud data in the current extent and is filtered to “all returns”) ……...93

Figure B9: Sample section of the study area showing the “Surface Display” - elevation view and topography (Note: This is only displaying 25% of point cloud data in the current extent and is filtered to “all returns”) ……94

Figure B10: Sample section of the study area showing the “Surface Display” slope view with topography inclination in degrees (Note: This is only displaying 25% of point cloud data in the current extent and is filtered to “all returns”) ……95

Figure B11: Parameters used for the creation of the DEM Raster where Value Field = Elevation → Triangulation = Natural Neighbor → Thinning Type = No Thinning, → Output Data Type = Float → Sampling Type = Cell Size → Sampling Value = .5 ……97

Figure B12: Sample of the output of the “LAS Dataset to Raster” tool. Displays segments of the DEM that were created for the entire 55 kilometer study area ……...98

Figure B13: Model workflow for finding sinks and their associated attributes (depth, length, width, etc.) ……..99

Figure B14: Areas within the DEM that are classified as artificial depressions (black) due to the damming of water at culverts (left) and bridges (right). The green outline in the left diagram denotes an actual hydrological sink with internal drainage ……100

Figure B15: A) Fill difference DEM displaying depressions & their depths. B) Fill difference DEM converted to an integer displaying depressions and their depths (excluding values below the RMSE of the dataset, 10cm). C) Polygons of depression derived from the ‘Raster to Polygon’ tool. D) Polygon of depression buffered to .5 meters, dissolved, and smoothed for aesthetics. E) Polygon of depression overlying the original depression depth DEM and statistics for the polygon calculated into a table with the ‘Zonal Statistics as Table’ tool. This table displays the maximum/mean depth and area of the depression. F) Polygon of the maximum geometry of the original polygon that contains attributes such as, the length of the major and minor axis, and orientation of the major axis. V) Represents a culmination of all the previous steps; Displays the buffered & dissolved depression polygon, with the attributes from step (F) and (E), joined by the use of the ‘Field Join’ tool ……..……103

Figure B16: Filtered output shapefile of karstic features within the study area determined by LiDAR analyses and open conduits / cave identified through field survey (blue) …….……104

Figure B17: A) – raster map of the spatial density of sinkholes identified through LiDAR analyses that have been proportionally weighted by the maximum depth of individual sinkhole polygons delineated. Density is measured in units of meters per square kilometer. B) raster map of the spatial density of sinkholes identified through LiDAR analyses that have been proportionally weighted by the area of coverage of individual sinkhole polygons delineated. Density is measured in units of square meters per square kilometer. C) raster map

of the spatial density of karst features identified through traverse-based surface surveys. Density is measured in units of individual features per square kilometer ……..……..…105

Figure B18: 3D view of LiDAR point cloud data of the entrances into Lillcher Cave with an illustration of a cave map from survey data (orange) shown with 2X vertical exaggeration …..106

Figure C1: drafted cave map of Lillcher Cave ……109

Figure C2: drafted cave map of Death Tube Cave ……114

Figure C3: drafted cave map of Fissure Cave ……..118

Figure C4: drafted cave map of Wiggley Cave ……..….121

Figure C5: drafted cave map of Valley Cave. ……..123

Figure C6: drafted cave map of Frac Soil Cave ……124

Figure C7: drafted cave map of Skylight Fracture Cave ……..125

Figure C8: drafted cave map of Broken Rock Cave ……126

Figure C9: drafted cave map of Gnome Cave ……..127

Figure C10: drafted cave map of Sidedoor pit Cave ……..128

Figure C11: drafted cave map of Cat Widow Caves ……...……129

Figure C12: drafted cave map of The Hole Cave ……131

Figure C13: drafted cave map of Mousey Hole Cave ……..132

Figure C14: drafted cave map of Nikad Cave ……..133

Figure C15: drafted cave map of Rockwall Cave ……134

Figure C16: drafted cave map of JC Gypsum Hole Cave ……136

Figure C17: drafted cave map of Paleochannel Caves ……137

Figure C18: drafted cave map of Bridge Cave ……138

Figure C19: drafted cave map of Airport Cave ……140

Figure C20: drafted cave map of Pothole Complex Caves ……..141

Figure C21: drafted cave map of Water Tank Cave ……142

Figure C22: drafted cave map of Jon’s Sink Cave ……143

Figure C23: drafted cave map of Horizontal Tube Complex Caves ……144

Figure C24: drafted cave map of Fracture Cave Complex ……..145

Figure C25: A) – raster map of the spatial density of sinkholes identified through LiDAR analyses that have been proportionally weighted by the maximum depth of individual sinkhole polygons delineated. Density is measured in units of meters per square kilometer. B) raster map of the spatial density of sinkholes identified through LiDAR analyses that have been proportionally weighted by the area of coverage of individual sinkhole polygons delineated. Density is measured in units of square meters per square kilometer. C) raster map of the spatial density of karst features identified through traverse-based surface surveys. Density is measured in units of individual features per square kilometer ……..147

PREFACE

The Gypsum Plain has been an area affected by dissolution throughout geologic history; this dissolution has resulted in the formation of a highly karstic and cavernous region. The karstic nature of the Gypsum Plain and the understanding of evaporite karst within the region has undergone increased study within the past decade; it is by no means fully understood but will likely be further studied and investigated. This paper investigates the east to west variability in evaporite karst occurrences across the Gypsum Plain; where the author forms a conceptual model of karst development across the region based on the observations of past and current research. This research was accomplished as a multi-part investigation of both speleogenetic development variations and potential geohazards related to infrastructure across northern Culberson County, Texas. Over the past decade, the Delaware Basin has become an increasingly more popular area for oil and gas exploration. The resulting increase in big rig traffic has caused accelerated road failure throughout the Gypsum Plain. Although not the primary objective, karst geohazards related to infrastructure were considered for a separate geohazard study in partnership with the Texas Department of Transportation. In addition to conceptual model creation, the ability to delineate potential hazardous zones and conduit orientations helped to identify the most dangerous locations in hopes of preventing future collapse or even catastrophic failure of the road base. Investigating the speleogenetic evolution and diagenesis of the karst in the region with respect to epigene and hypogene processes was completed to identify locations with heightened potential for dissolution and ion mobilization across the region. This study evaluates / delineates the orientation, type, and abundance of evaporite karst through a two-pronged approach; firstly,

through the use of traditional cave mapping / physical land surveys and secondly through remote sensing and the use of spatial density analyses utilizing LiDAR (Light Detection and Ranging). In addition to the following research below, supplementary in-depth reviews of previous literature, detailed methodology used, and detailed results of investigation are located within appendix A, B, and C, respectively.

Speleogenetic Model of Evaporite Karst Occurrences of the Gypsum Plain Utilizing Karst Mapping and LiDAR Analyses in Culberson County, Texas, USA

ABSTRACT

The Gypsum Plain region of the Delaware Basin hosts approximately 1800 km^2 of the Castile Formation outcrop. A myriad of karstic developments from closed sinkholes to large multi-kilometer cave systems have been documented within the region. Karst studies on the distribution and speleogenetic evolution within Castile strata began within the last decade with ever increasing data resolution. In this study, a combination of both physical field surveys and analyses of high resolution (~30cm accuracy) LiDAR data was used to create a theoretical model for karst development across the region. This idealized model considers speleogenetic formation type variations (hypogene and epigene), the density of karstic features based on lithology variations, and the connection between the local hydrostratigraphic setting and the regional hydrogeological framework. Field studies included physical mapping of 20 km^2 of the Gypsum Plain from the Castile's western outcrop to where it dips into the subsurface to the east. These surface surveys involved the recording of all surfically-expressed karstic phenomena and the mapping of all enterable caves so that the speleogenetic evolution could be analyzed. The way in which hypogene and epigene caves are surfically expressed across the region indicates that many of the caves have been affected by either multi-stage epigenetic development or multi-stage hypogenetic development with epigenetic overprinting. Through the use of the methods outlined above, surficial karst manifestations vary across the region, from hypogenetic exposures in the

west and epigenetic phreatic / vadose exposures in the east. Additionally, supplementary LiDAR data was used to create digital elevation models (DEM) so that the effectiveness of physical field surveys versus remote sensing techniques could be determined. Previous works in the area by Stafford et al., (2008b) determined that remote sensing only preserved 36% of all karstic features found through physical field surveys. Given today's advancements in remote sensing accuracy, this study determined that on average LiDAR analysis identifies almost seven times more karstic features than physical surveys over a given area.

INTRODUCTION

The Gypsum Plain of west Texas hosts a plethora of karstic exposures that have only recently been investigated in detail within the last decade (Stafford, 2008a,b). The larger and more famous carbonate caves of the Capitan Formation such as Carlsbad Caverns and Lechuguilla Cave to the north have been extensively studied due to their largely complex and expansive cave systems. The widespread evaporite karst of the Permian Gypsum Plain has traditionally been overlooked and generally understudied; this is despite the fact that karst features of the Delaware Basin are one of the most prominent displays of gypsum karst in North America. Within the Delaware Basin, the primary formation that hosts cavernous porosity is the soluble gypsum and anhydrite of the Castile Formation. Due to the highly soluble nature, the Castile Formation has undergone a significant amount of dissolution since deposition and contains extensive cave and karst features (Stafford et al., 2008b). The caves found within the Castile Formation formed by both epigene and hypogene processes; however, understanding which exact processes affected the Castile and the timing of dissolution can be difficult as many hypogene caves have been heavily overprinted by epigene processes. Throughout the Castile, karst features vary from surficial karren, sinkholes, and solution breccias to large complex caves that have been affected by multiple processes (Stafford, 2008a). The objective of this study is to improve evaporite karst characterization within the Delaware Basin by creating an idealized model that displays the variability in speleogenetic evolution and hydrologic framework that exists across the Gypsum Plain in relation to the geomorphic system

Study Area

Located in the Delaware Basin, the study area sits atop an extremely large depocenter where over a billion years of the rock record is preserved; ranging from the 1.3 by old Precambrian basement to the less than 10,000 ybp Holocene sediments (Hill, 1996). The Delaware Basin is bound on its periphery by a series of exposed reef structures; to the west by the Apache Mountains, to the north by the Guadalupe Mountains, to the south by the Glass Mountains, and to the east by the Central Basin Platform. The large Gypsum Plain that encompasses the area is primarily blanketed by the Ochoan Castile and Rustler deposits at the surface (Fig. 1). Specifically, this study focuses on the northern portion of Culberson County, Texas, extending ~35 kilometers south of the New Mexico border and 50 kilometers west to east across the Castile outcrop region (Fig. 1); delineated as a representative subsection of the Gypsum Plain to investigate the variations in karst development in line with stratal dip that trends west to east.

Physiographically, the study area is located on the eastern edge of the Basin and Range province and the northern edge of the Chihuahuan Desert. The Trans-Pecos region is primarily a desert / semi-arid environment with scant precipitation, rapid evaporation, moderate winters and afternoon showers in spring months. The Gypsum Plain receives less than 300 mm of precipitation per year (Beuchner, 1950); average temperature is less variable than the rainfall, with mean summer temperatures varying from 24°C to 30°C; however, temperatures can reach upwards of 38°C.

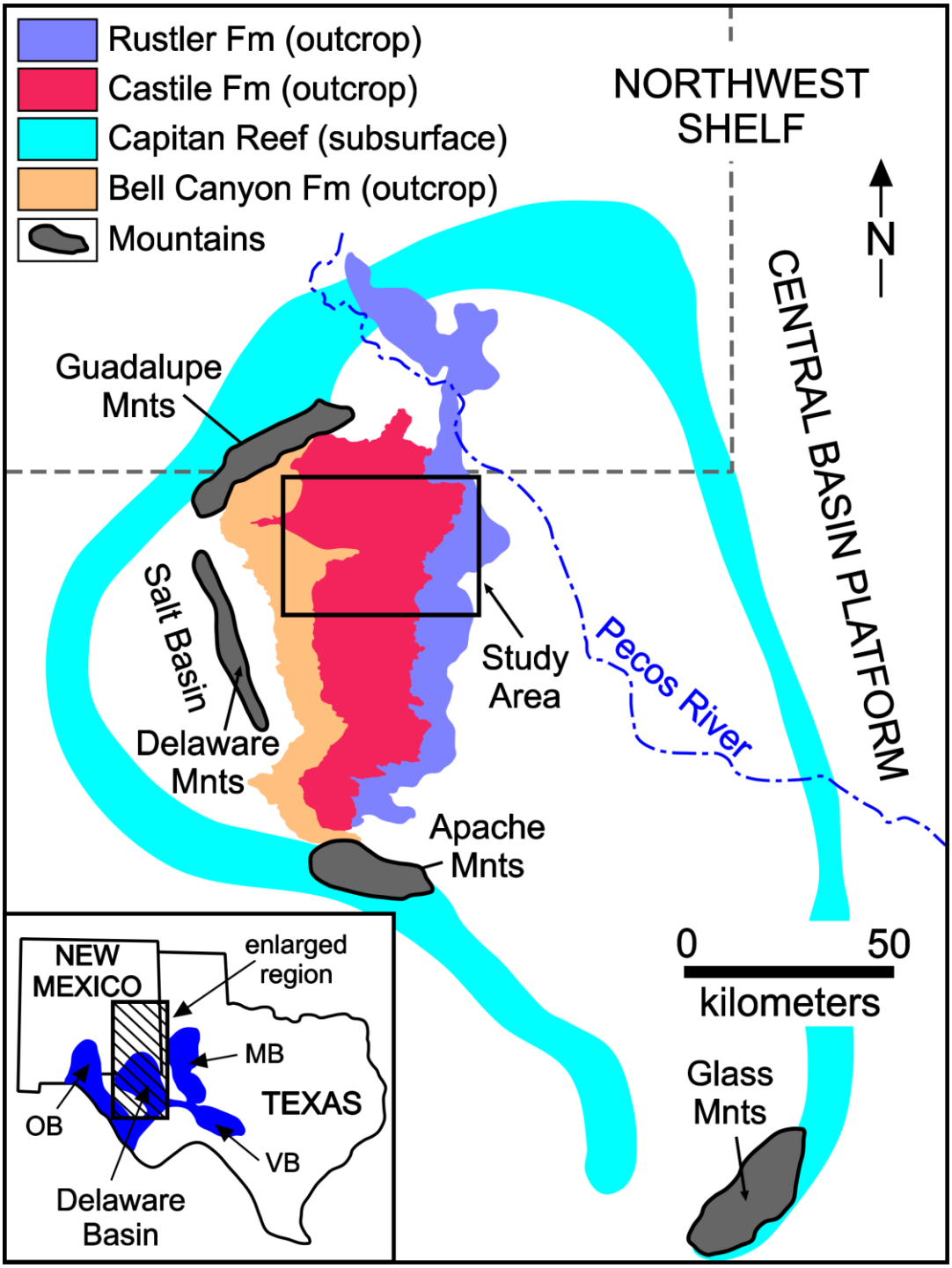

Figure 1: Regional map displaying the generalized location of Permian strata outcrops within the Gypsum Plain (modified from Stafford et al., 2008a).

Geologic Setting

Late Permian sequences in the Delaware Basin are divided into two main series: Guadalupian Series (271-260 mya) and Ochoan Series (260-251 mya) (Adams, 1965) (Fig. 2). The Guadalupian Series represent deposition of a thick, clastic, basin-filling facies with approximately 900-1200 m of total sediment (Hills, 1984). The periphery of the basin during this time was dominated by reef growth where the reef crest rose approximately 500 m above the basin floor. The central portion of the basin was dominated by sandstones and siltstones, the marginal areas by limestone deposits, and the backreef formed evaporite lagoons (Adams, 1965). Continued subsidence provided accommodation space for the central basin formations such as the Cherry Canyon, Brushy Canyon, and Bell Canyon to be deposited. These formations represent the clastic-dominated, primarily terrigenous, sediments that were deposited during episodic sea-level fluctuations during the Guadalupian when shelf environments were subaerially exposed (Scholle et al., 2004). In the closing stages of the Guadalupian, the Permian Basin became relatively tectonically stable and carbonate sedimentation was terminated (Adams, 1965). Scholle and others (2004) postulate that this is largely due the increased basin restriction that began near the end the end of the Guadalupian.

Following the Guadalupian, Ochoan evaporite formations were deposited (260 to 251 mya). Although there are many controversial aspects involving the ongoing depositional mechanisms within the Delaware Basin at the onset of the Ochoan (Kirkland, 2003), it is widely accepted that continual restriction of evaporite seas from the open ocean resulted in deposition of

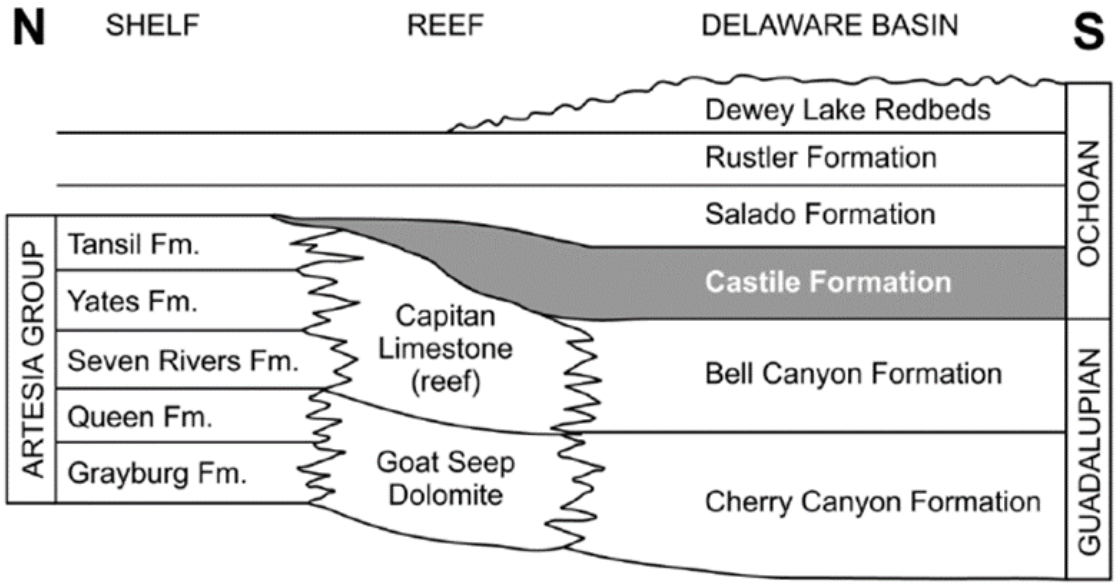

Figure 2: Stratigraphic section from the Shelf (North) to Delaware Basin (South) of lithologic units within the study area (adapted from Scholle et al., 2004).

the first phase of evaporite filling within the Delaware Basin. This closure marks the onset of Ochoan time and the beginning of deposition of the Castile Formation; the Castile reaches approximately 550 m in thickness in the northern basin (Scholle et al., 2004). The Castile consists of millimeter-scale interbedded laminae of gypsum, anhydrite, organic matter, and calcite; interbedded layers have been interpreted as varves and represent seasonal salinity fluxes (Scholle et al., 2004). The distinct characteristic of large scale, laterally-continual laminations and lack of shallow water sedimentary structures suggest that the Castile was deposited in deep water that eventually filled the entire basin (Scholle et al., 2004).

The Castile Formation grades conformably into the Salado which extends far beyond the margins of the Delaware Basin and crosses Guadalupian reef and shelf facies forming an unconformity boundary (Kelley, 1971; Hill, 1996). The Salado Formation contains laminated

halite, anhydrite, sylvite, other evaporites, and minor amounts of siliciclastic material; but does not generally appear in outcrop throughout the Delaware Basin because of its highly soluble nature (Scholle et al., 2004). Rustler strata cap Salado deposits and mark the final evaporite sequence deposited during the Ochoan. During this time, sea-level incursion and subsequent transgressions and regressions deposited cyclic layers of large-scale limestone-dolomite and anhydrite-gypsum deposits (Hill, 1996).

Following Ochoan time, the Delaware Basin began to shift from a marine sedimentation depocenter to a positive area dominated by clastic sedimentation. During the late Cretaceous to early Tertiary, the Laramide Orogeny permanently uplifted the region above sea level (Hill, 1996), tilting the Delaware Basin approximately 3-5° eastward and elevating it 1.2 km above sea level on the western side, where it remains today (Horak, 1985). Subsequent to Laramide uplift, Basin and Range extension commenced and lasted from 30 mya to present, producing conjugate jointing and fault sets oriented approximately N75E and N15W throughout the Gypsum Plain (Nance, 1993). Many of the formations resultant karstic developments within the Gypsum Plain have been a product of these conjugate fractures as well as Quaternary climate change. During the middle to late Pleistocene, Delaware Basin climate alternated between drier and warmer periods to colder and moister periods (Hill, 1996). Today, the Gypsum Plain has transitioned back into an arid, dry climate. However, due to the highly soluble nature of the Gypsum Plain, the current landscape displays many geomorphic traces of its previously wetter conditions.

METHODOLOGY

To characterize karst evolution across the Gypsum Plain, traditional cave surveys were coupled with remote sensing analyses to investigate the spatial distribution of karst features in order to assess the hydrogeological controls on speleogenesis. Spatial analyses of solutional conduits were accomplished through traditional cave mapping, overland surface mapping, and the use of remote sensing analyses of LiDAR data (Light Detection and Ranging). Data collection and analyses were focused proximal to roads within the study area in conjunction with geohazard characterization by the Texas Department of Transportation. Traverse-based surveys were conducted within 100 m of the right of way of 55 km of infrastructure that traverses the Gypsum Plain from west to east in northern Culberson County. The 13.1 km^2 of total surface survey was conducted at 20 m traverse spacing, and all karst features identified greater than 10 cm in diameter were recorded and classified in the field. All caves discovered large enough for human entry were entered and mapped using standard cave mapping techniques; morphometric features and lithologic variations were noted within surface surveys and cave maps to assess speleogenesis.

LiDAR data used for this study included approximately 20 km^2 of data acquired in approximately 300 m wide swaths along roads in northern Culberson County. Data has an average horizontal resolution of ~30 cm and vertical resolution of 10 cm for bare earth LiDAR returns. From this data, delineation of sinkholes was accomplished through processing of "fill-difference" digital elevation models (DEMs) to identify areas topographically lower than the surrounding land surface (Doctor and Young, 2013); all sinkhole features less than 10 cm in

depth were removed because they fell below the resolution of data. However, depressions associated with roadway construction and other man-made features such as ponds were also identified through LiDAR processing (Liu, 2008); these anthropogenic / non-karst features were removed manually. Final data reduction resulted in a map that contains natural sinkholes (i.e. karst features) as determined by LiDAR analyses. Density plots were calculated based on the number of features per square kilometer in order to interpret lateral variability in regional karst.

KARST MORPHOLOGY

The presence of both hypogene and epigene karst development has been documented throughout the Gypsum Plain (Stafford et al., 2008); caves within this study represent both multi-stage epigenetic and multi-stage hypogenic processes with epigenetic overprinting. Epigenetic caves tend to be solutionally-entrenched and strongly controlled by fractures while hypogene manifestations are driven by proximity to lithologic variability and are expressed as larger voids. In addition to surface dissolution (sinkholes, shallow caves, depressions) more evidence of extensive dissolution can be seen throughout the study area as diagenetic alterations such as intrastratal brecciation and evaporite calcitization.

Epigene Karst

Epigene cave development within the study area is divided into two main categories, vadose and phreatic morphologies. Epigene caves that formed within the vadose zone are expressed largely as fracture-oriented conduits dominated by increased entrenchment and abundant, small-scale scallops. Morphologically, vadose caves maintain relatively narrow passage apertures relative to height and are generally laterally-limited to 10s of meters in length, as illustrated in Nikad Cave and JC Gypsum Hole (Figs. 3A *and* 3B) in this study. Nikad Cave is associated with an entrenched 40-m-long, 30-m-wide arroyo and a 2500 m^2 watershed. The entrance is one meter wide within laminated gypsum bedrock and the cave is humanly passable for 28 m as a single, relatively straight, horizontal passage. Passage width tapers from one-meter-wide at its entrance to less than 30 cm wide at the end of the survey. JC Gypsum Hole exhibits a

similar morphology, with an inward reducing aperture and increased entrenchment along a fracture that runs along the cave ceiling (Fig. 4F); it is 35 m long and drains a watershed covering 10,000 m^2. As these caves form and water originating as overland flow becomes saturated, solutional aggressivity is reduced, limiting lateral development as saturated fluids recharge along fracture planes. This geomorphic expression in vadose epigene caves is consistent with dissolution characteristics of sulfates (Klimchouk, 2000).

Death Tube Cave and Lillcher Cave are complex, multi-stage epigenetic caves formed originally in the phreatic zone but later exposed to vadose overprinting (Figs. 3C *and* 3D). Death Tube Cave is a classic example of an epigene phreatic tube overprinted by vadose processes with more than 200 m of low gradient passage development (Fig. 3D). The elliptical morphology of the majority of the cave indicates that it formed when the water table was significantly higher than it is currently and that vadose overprinting observed is the result of local base level drop. Vadose entrenchment is much more significant within the first 30 m of the cave; entrenchment has not substantially affected the remainder of the cave where only small deviations from elliptical passages are present and passage floors are often armored with thick clay deposits (Fig. 4G). The cave terminates in a sump but throughout the low gradient passage, various “bathtub rings” of organic material are present indicating that the majority of the cave remains in the epiphreatic zone even though vadose overprinting is active near the arroyo-entrenched entrance.

Lillcher Cave development began with preferential dissolution along fractures within the phreatic zone, forming a simple dendritic morphology of elliptical tubes with a surveyed length and depth of 116 m and 17 m respectively, that terminates in a sump (Fig. 3D). Entrances and inlet tubes are morphologically comparable with phreatic tubes; having formed initially as

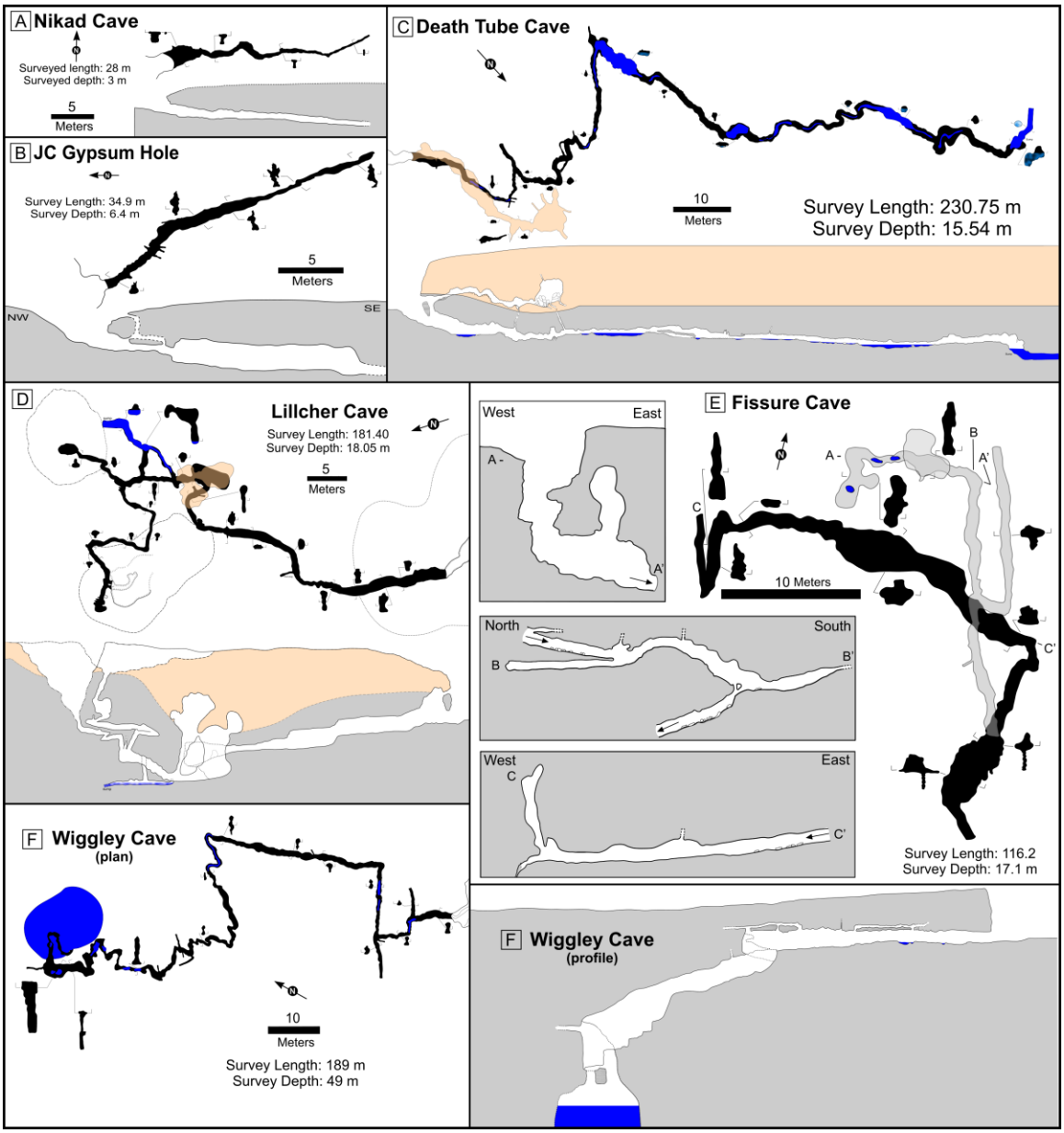

Figure 3: Simplified cave maps that represent the typical epigene vadose (3A: Nikad and 3B: JC Gypsum Hole), epigene phreatic (3D: Lillcher and 3C: Death Tube), and hypogene (3F: Wiggley and 3E: Fissure) developments that were surveyed across the study area in both plan and profile views. Portions of Lillcher and Death Tube caves are suffosion features as represented in tan color in plan and profile views; blue indicates water at time of survey.

elliptical tubes that were later entrenched by vadose processes (Fig. 4D); the cave currently exhibits three entrances, all of which have been heavily entrenched. In the lower cave portion,

where the most heavily entrenched passage near the junction with the other major conduits, a room largely developed within gypsic soil attests to more intense vadose entrenchment in the past. Here, original void space was infilled with secondary sediments that were subsequently eroded to produce a cave chamber partially formed within both gypsum bedrock and gypsic soil. Upper portions of sinkhole entrances are composed of one to three meter thick sequences of gypsic soil that are being funneled into entrances; it is probable that the room in the lower portion of the known cave is another sinkhole entrance that was completely plugged by sediment in the past and subsequently infilled. Effectively, Lillcher Cave originally formed in the phreatic zone and was then exposed to vadose overprinting at some time in the distant past, likely during the Pleistocene, and subsequently infilled with gypsic soils / sediments during previous climatic shifts. Today, the system is equilibrating with current climate and sinkhole fills are being piped into the cave. Thus, Lillcher Cave remains in a transitional vadose / phreatic environment but exhibits evidence of at least two distinctively different episodes of vadose entrenchment.

Although soil piping is a common occurrence throughout the Gypsum Plain, formation of suffosion caves are the least documented occurrences of karst in the area. These caves form as small- to large-scale sediment piping features and can exhibit much larger passages and spatial extent than previously thought; filled sinks that are actively opening through suffosion as seen in Lillcher Cave are not uncommon. The upper passage of Death Tube Cave formed along the bedrock / gypsic soil contact which acts as a significant differential permeability horizon. This horizontal contact is intercepted by vertical fractures that follow a similar trend to the lower passage into which suffosion products are being piped. It is likely that this 40 m long soil cave formed during backflooding events when fluids are injected laterally along the gypsum / soil

contact at the entrance and vertically from fractures connecting soil and bedrock portions of the cave. Fluidization of partially-lithified sediments resulted in stoping upwards and soil cave formation (Fig. 4B). A series of 25 cm diameter inlet piping tubes in the soil cave ceiling follow a fracture and appear to have formed as small-scale piping features during normal precipitation events.

The examples above represent greater complexity of epigene cave development than has been previously documented in the Castile Formation. Significant epigene cave development within the phreatic zone has not been previously reported and extensive suffosion caves were previously unreported; however, current research suggests that suffosion caves are extremely common and can reach significant size as long as there is a sufficient outlet for removal of insoluble clastic particles, either through a cave conduit as described above or through highly fractured media.

Hypogene Karst

In contrast to epigene cave development, hypogenic caves form in semiconfined systems based on pressure and density gradients and are not directly associated with surficial processes during formation. As suggested by Klimchouk (2007), identification of hypogene karst can be difficult because of the nature of their origin; hypogene caves can only be explored by cavers after they have been breached or decoupled from the environment in which they formed and often exhibit epigenetic overprinting. Primary criteria for identifying these hypogenetic features are the caves morphological expression and hydrostratigraphic position (Klimchouk, 2007). Hypogene caves likely comprise more than half of the total cave development throughout the Gypsum Plain, but surficial expression through surface denudation breaching is spatially limited (Stafford et al.,

2008b). Although hypogenic caves are common across the Gypsum Plain, they are somewhat atypical of most reported hypogene manifestations (e.g. Klimchouk, 2007) in that complex maze caves are largely undocumented, instead single riser features are most prevalent.

Fissure and Wiggley caves are typical hypogene features of the Gypsum Plain with morphologies composed primarily of large, single, ascending passages with numerous cupolas, ceiling channels, and domes which are indicative of ascending fluids (Figs. 3E *and* 3F). These cave examples occur on the western edge of the Gypsum Plain where the contact with underlying Bell Canyon clastics is less than 60 m. Although they are not the most extensive hypogene caves known in the Castile Formation, they share similar morphologic and hydrostratigraphic characteristics to much larger hypogenetic caves found within the area (Stafford et al., 2008a).

Wiggley Cave, similar to Border Cave in the proximal region (TSS, 2016), is 189 m long, 49 m deep, and gives access to a lower level lake room. The cave is heavily entrenched by vadose overprinting which forms a meandering canyon-like passage that ranges from two meters tall near the entrance to over 15 m tall in the lower portions; however, the ceiling remains level for extended sections as an elliptical tube with common cupolas connected by an undulating ceiling channel. In several sections, small pits occur which correlate directly with larger ceiling domes and show consistent morphologies of upward migrating fluids along the ceiling with subsequent vadose floor entrenchment. The lowest cave portion descends from a dome pit into a lake room of indefinite depth and approximately 20 m in diameter; anecdotal reports from divers of other similar lake rooms in the area indicated these features can extend more than 40 m deep. Wiggley Cave was formed by ascending fluid sourced from the underlying Bell Canyon Aquifer as a large

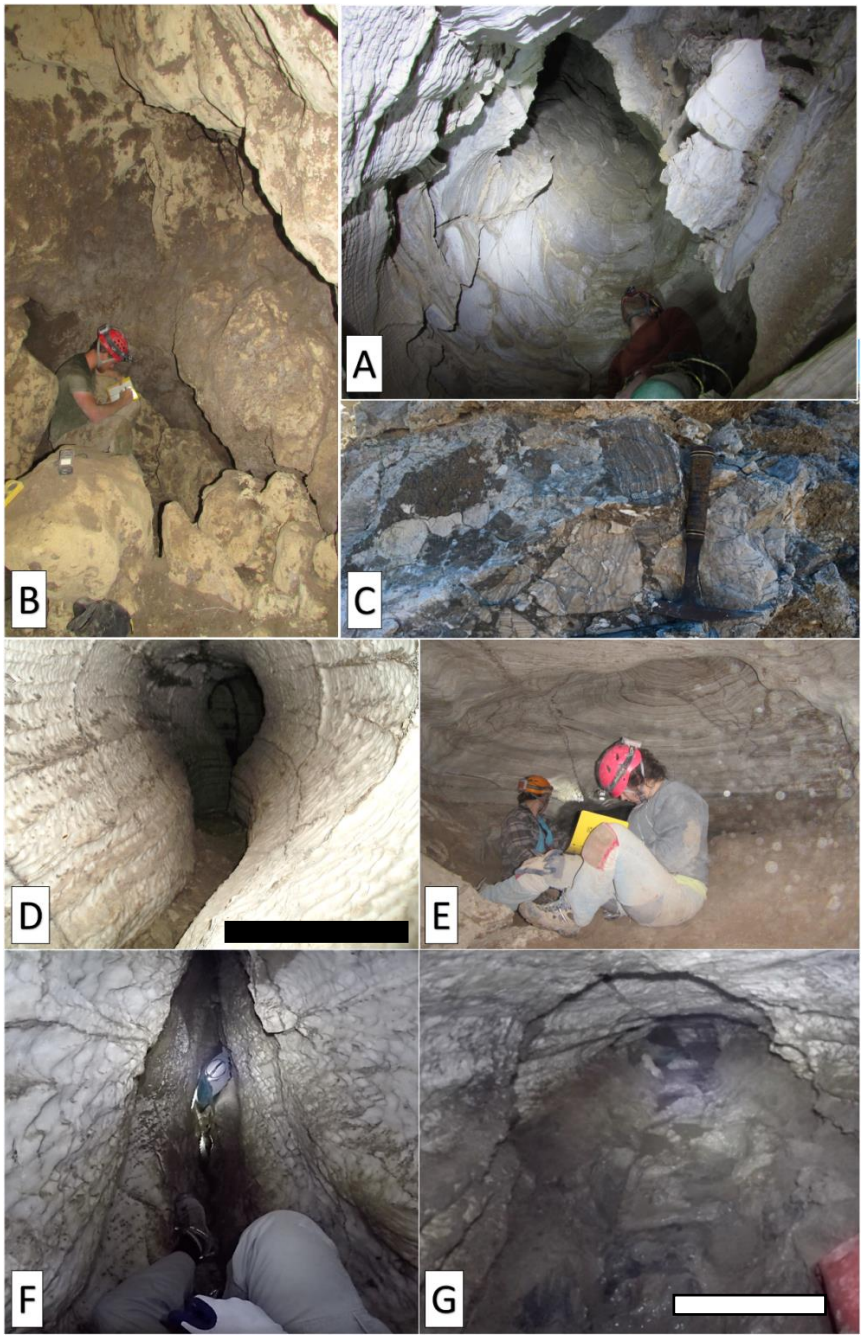

Figure 4: Epigenetic and hypogenetic morphological features found throughout the study area: A) Large hypogene dome (Fissure Cave); B) Soil suffosion chamber (Upper Death Tube Cave); C) Brecciated zone (Breccia Pipe); D) Phreatic tube overprinted by entrenchment (Lillcher Cave); E) Cupolas in relict passage (Fissure Cave); F) Epigene vadose entrenchment (JC Gypsum Hole Cave); G) Elliptical phreatic tube (Death Tube Cave) Note: black and white bars represent 50 centimeters.

solution chamber near the contact coupled with a single riser tube along fracture planes. After surface breaching, vadose entrenchment significantly overprinted the cave with associated entrenchment forming a watershed covering approximately 60,000 m^2.

Fissure Cave has a surveyed length of 116 m and depth of 17 m (Fig. 3E), forming a multi-level, fracture-controlled hypogene cave that is moderately overprinted by vadose entrenchment. At inception, fractures provided paths for ascending fluids with lateral migration along preferential gypsum laminae. Lower level passages contain large domes and abundant cupolas; the majority of ceilings and walls are completely smooth from ascending waters in a sluggish flow regime (Fig. 4E). In upper portions of the cave, large domes extend more than five meters as vertical risers (Fig. 4A) and it is probable that the entrance pit was simply the tallest of these domes and first to be breached by denudation. The cave exhibits minimal vadose overprinting in the entrance region which is comparable to the associated small drainage area (less than 3000 m^2). The lower portions of the cave exhibit solutionally-widened fractures too small for human passage but likely connect to additional hypogene chambers and conduits, and potentially a base-level lake similar to Wiggley Cave. Both Fissure and Wiggley caves exhibit vastly different morphologies when compared to their epigene counterpart. However, because of current epigene overprinting, the recognition of specific morphometric features and hydrogeologic environment were critical criteria assessed in relation to speleogenesis.

In addition to cave development, diagenetic alteration/dissolution of host strata is common; intrastratal dissolution often results in large scale collapse horizons containing “blanket-dissolution breccias” in the Delaware Basin (Anderson et al., 1972). Lateral dissolution breccia forms as halite interbeds are dissolved and overlying gypsum cannot be supported and

collapses. Dissolution breccias can be traced across the basin and have been correlated to still present halite interbeds located in the subsurface in the eastern Delaware Basin (Anderson et al., 2001). In addition to lateral dissolution, vertical dissolution can form breccia pipes, where ascending fluids drive dissolution through density convection. As void space is created at depth, overlying strata collapse into voids and upward stoping proceeds vertically as additional dissolution and collapse enhance vertical brecciation (Fig. 4C) (Anderson and Kirkland, 1980).

SPELEOGENETIC MODEL OF THE GYPSUM PLAIN

Karst development varies from west to east across the Gypsum Plain in the direction of regional dip and stratal thickening. As seen in Figure 5, this variation is present in the case of geomorphological differences, karst density (both epigene and hypogene), and proximity to differing lithologies. Along the western edge of the Gypsum Plain, the Castile Formation thins to nonexistence along the updip solutional margin; while progressively increasing in thickness towards the east as the unit dips into the subsurface and is armored by overlying strata that prevent denudation.

Caves in the western Gypsum Plain, where the Bell Canyon is relatively close to the land surface, are typically expressed as hypogene caves. Because of Laramide uplift, strata dips 3-5° east / northeast in the Delaware Basin (Lee and Williams, 2000), groundwater recharge into basin clastics beneath Castile evaporites quickly shift to a confined system with elevated hydraulic pressure. Locally, gypsum strata thickness in the western Gypsum Plain ranges from 100 to zero meters where Bell Canyon outcrops and groundwater recharge occurs; however, valleys and topographic lows within the Gypsum Plain are commonly lower than surface exposures of Bell Canyon clastics, creating potentiometric lows within the system towards which confined fluids migrate. With elevated potentiometric pressures in the west where overland flow recharge into Bell Canyon clastics is most intense from the watersheds of the Delaware Mountains, hypogene caves commonly develop throughout the western flank of the Gypsum Plain (Fig. 5). This is not to say that hypogene caves do not form further east, instead it suggests that hypogene karst development is simply more intense in the western portions; however, it is probable that

hypogene dissolution is intense at the lower boundary of Castile strata throughout the region and hypogene caves only appear more common in the west because greater incidence of breaching.

In addition to hypogene cave development, the presence of vertical breccia pipes indicates significant upward migration of fluids throughout the region. Lee and Williams (2000) suggest that these brecciated zones result from solutionally aggressive waters sourced from the Bell Canyon Aquifer that rise through density convection to create significant void space; collapse of these deep-seated caverns then stope towards the land surface (Anderson et al., 2001). Unlike the hypogenetic caves, breccia pipes are surficially expressed throughout the study area; they are surficial manifestations of deep-seated collapses that have stoped upward. Consistent with brecciated zones found in the study area, similar pipes have been documented to extend through the entire thickness of the Castile Formation in the central Delaware Basin (Hill, 1996). These breccia pipes support the idea that hypogene speleogenesis is active across the Gypsum Plain, but is focused at the Bell Canyon / Castile contact. Because Castile evaporites semi-confine the underlying clastic aquifers, hypogene karst development remains isolated from epigene karst until hypogene features are breached by surface denudation and transition into an epigene environment.

Relatively shallow epigene karst is widespread throughout the Gypsum Plain but most common in the eastern portions of the study area where epigene processes have not been captured by breached hypogene caves; breached hypogene caves exhibiting accelerated epigenetic overprinting are common in the west. In the east, there are no shallow surficial expressions of epigene karst connected to larger hypogene occurrences. Thus, these caves are vertically restricted and display typical reducing apertures and moderate entrenchment associated with pure

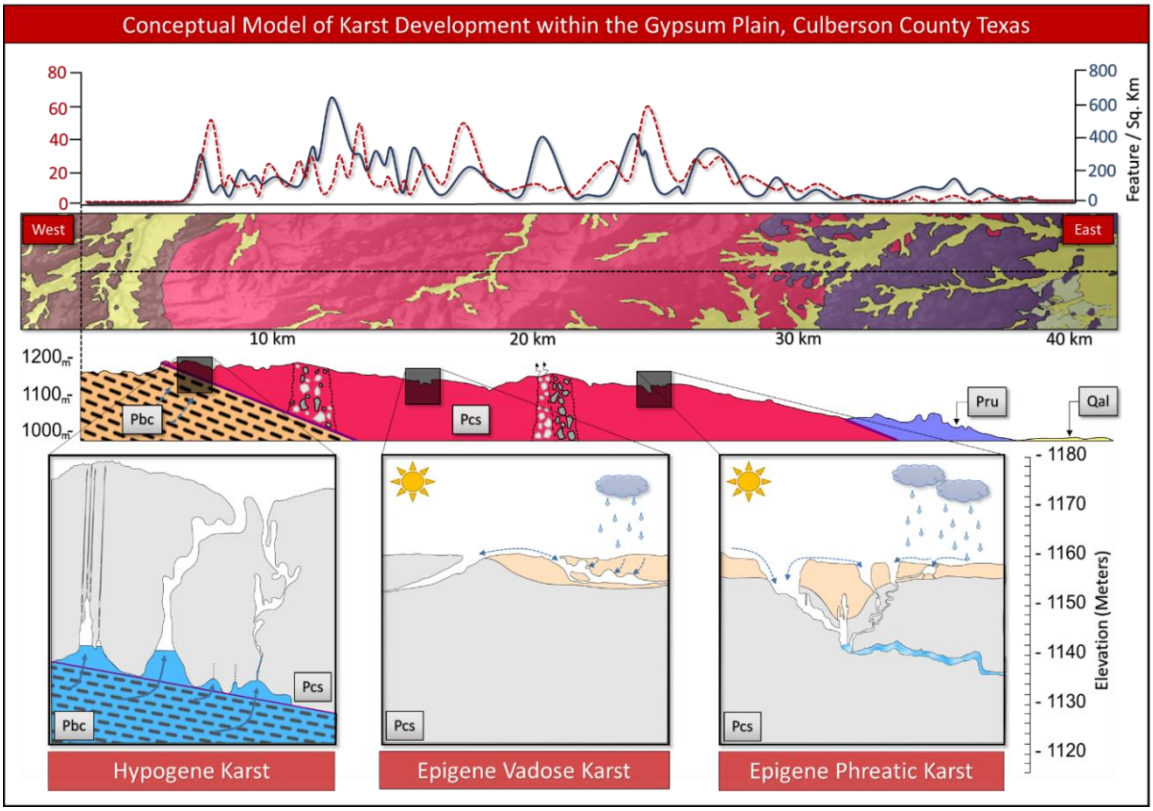

Figure 5: Idealized model of karst development across the Gypsum Plain (Pbc = Bell Canyon Formation, Pcs = Castile Formation, Pru = Rustler Formation, Qal = Quaternary Alluvium): Top graph displays the frequency of surface karst manifestations per square kilometer identified by surface surveys (red) and LiDAR analyses (blue); Middle diagram displays the cross-sectional relationship between Castile Formation and its bounding formations. Lower diagrams display a representation of the variability in karst development type (i.e. hypogene/epigene) across the study area.

epigene evaporite caves formed in the vadose zone along fractures. However, moving even further east within the study area, caves are expressed as multi-stage epigenetic caves formed within both vadose and phreatic zones (Fig. 5). The occurrence of epigenic caves formed within the phreatic zone indicates that perched aquifers and more complex groundwater systems exist within the Castile Formation than previously recognized. It is probable that independent, shallow groundwater systems have developed throughout the eastern region of the study area in order to accommodate local groundwater recharge and direct it towards the Delaware River.

Suffosion cave occurrences are much more common in the central and eastern portion of the study area, usually associated with epigenetic caves (Fig. 5). Bedrock conduits provide pathways for soil removal from the system but are small enough to limit flow and increase residence time of soil fluids. Increased residence time enables dissolution of the gypsic soil fraction resulting in development of soil caves that are a hybrid of dissolution and suffosion processes; these occurrences create relatively large soil chambers and domes with smooth walls. To the west, located near hypogene occurrences, soil caves are highly subdued; these caves have the ability to recharge waters quickly after breaching, thus water residence time in soil is greatly reduced as it flows quickly through the breached system. The suffosion process typically requires infilling of sinks or draping of sediments over pre-existing caves / solutionally-widened fractures within the study area; breached hypogene caves that have been exposed to epigene processes receive little or no infilling because of their ability to transport sediments into the subsurface, thus with less infilling less suffosion is possible.

In addition to variations in specific karst features from west to east, overall density of features varies as well. Most surficially-expressed karst identified by either field survey or LiDAR analyses are located within the Castile Formation (Fig. 5). Karstic occurrences drop dramatically beyond Castile outcrops within the study area. The Bell Canyon contains no known karst features as it is predominantly a siliciclastic unit; karst features within the Rustler Formation are subdued as this unit is primarily composed of limestone and is less soluble than the Castile. LiDAR analyses reveal significantly more karst features than surface surveys because shallow, filled sinks coupled with denser vegetation in some regions preclude identification of subtle karst features in the field; however, additional features identified through LiDAR analyses have been

randomly checked and all field verifications indicate that these are true karst features that are extremely shallow and / or small.

CONCLUSIONS

Previous research indicated that >10,000 individual karst features dominated by hypogene processes exist within the Gypsum Plain, with increased karst development along the western edge of the outcrop area (Stafford et al., 2008b). This study further expands upon this with increased data resolution and develops a conceptual model for karst spatial distribution (Fig. 5). Karst development appears most predominant on the western edge because of intense hypogene karst breaching where potentiometric pressures in the underlying Bell Canyon Aquifer are highest and Castile thinning from surface denudation is greatest; breccia pipes occur throughout as large-scale hypogene dissolution at the Bell Canyon / Castile contact has created stoping features. The central portion of the Gypsum Plain is dominated by shallow, fracture-controlled epigene caves formed in the vadose zone. The eastern portion of the Castile outcrop exhibits more complex epigene caves of phreatic origins associated with shallow, perched aquifers that are likely coupled to entrenchment of significant fluvial systems (e.g. Delaware River) that bisect the Gypsum Plain.

Based on this study, which included high-resolution LiDAR analyses, Stafford et al., (2008b) significantly underestimated the region's potential for karst; this original estimation can easily be increased by at least an order of magnitude and possibly two orders of magnitude. Just under a decade ago, the highest resolution data for remote sensing within the region was 10 m accuracy DEMs and one-meter accuracy digital orthophotos (DOQ). The original study conducted by Stafford et al. (2008b) concluded that by analyzing remote sensing data (DOQ), only 36% of karst features over a given area were identified when compared to what could be

identified through physical land surveys. On average, 42 karstic features were identified per square kilometer through physical land surveys and over 270 karstic features were identified per square kilometer through high-resolution LiDAR analyses (Figs. 5*;* 6A). This value extrapolated over the entire Gypsum Plain results in an estimation of approximately 500,000 surficially-expressed karst features within Castile outcrop alone. Compared to traditional surveys in the area, physical surface mapping revealed ~15% of all karst detected through high resolution (~30 cm accuracy) LiDAR analyses. In other words, advances in resolution and accuracy of remote sensing data indicate that LiDAR is almost seven times more effective at identifying surface manifestations when compared to physical land surveys.

In addition to increased accuracy of remote sensing in recent years, LiDAR has become much more efficient because it can be manipulated to reveal features that could be easily missed when doing surface surveys. Karstic features that are either shallow, small in diameter or completely surrounded by vegetation can now be identified with ease and associated drainage basins can be more easily assessed (Figs. 6A; 6B). Although identifying exact scale and location of deep-seated hypogene caves that have yet to breach was outside of the scope of this research, it is certain that within the subsurface, karst that has yet to be surficially-exposed is significantly higher than current estimates, providing interesting and challenging topics for future studies.

One of the most important factors of LiDAR analyses within this study is its ability to detect open conduits into the subsurface. Karst depressions identified through DEM analyses may or may not contain open conduits into the subsurface; areas previously identified by DEM analyses were re-investigated using LiDAR point cloud 3D and cross sectional views. If the 3D views were interpreted to contain open conduits, these areas were then flagged to be checked and

mapped during field work. Ultimately, advances in remote sensing are enabling better visualization of surface / subsurface relationships (Fig. 6C). The ability to specifically target / detect karst features with highly increased efficiency opens the door to conducting karst studies and understanding regional speleology on a much larger scale than traditional survey methods.

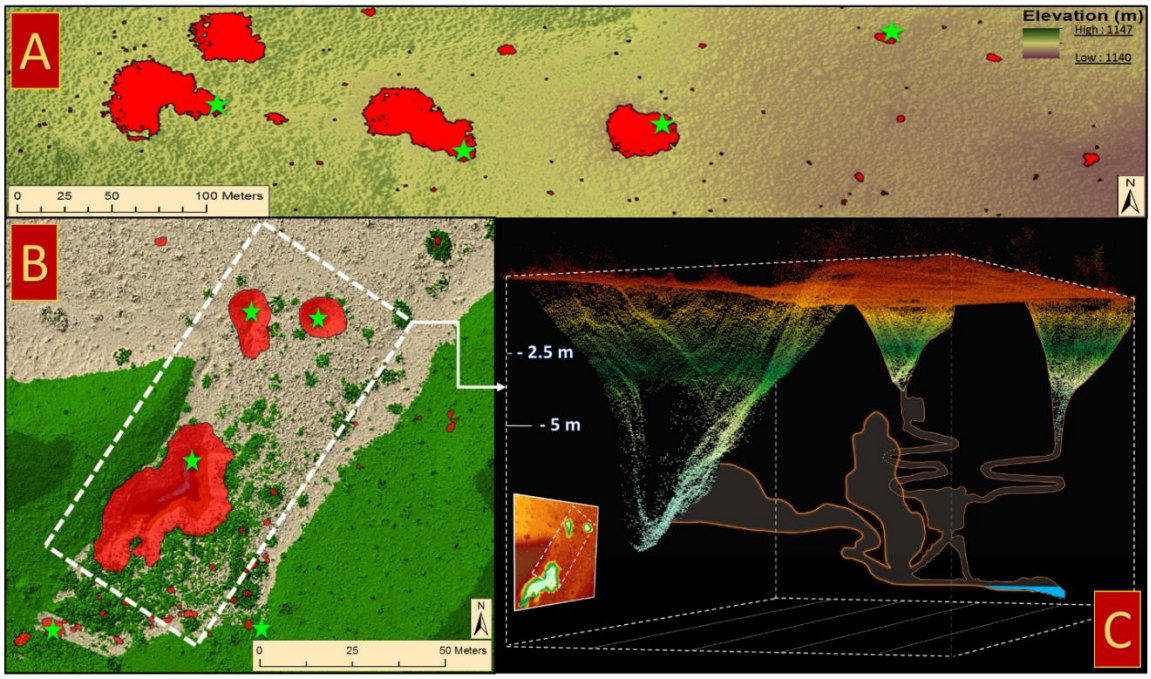

Figure 6: LiDAR analyses. A) discrepancies in karst manifestation identification of surface walks (green stars) and LiDAR analyses (red); B) LiDAR and DEM analyses enhance identification of depressions surrounded by dense vegetation (small isolated depressions in red).; C) 3D view of LiDAR point cloud data of the entrances into Lillcher Cave with simplified cave map from survey data (orange) (vertical exaggeration is 2X).

.

ACKNOWLEDGEMENTS

This research was partially funded by the Texas Department of Transportation with support from the Department of Geology at Stephen F. Austin State University. The authors are indebted to following field assistants that made this work possible: Aaron Eaves, Ashley Landers, Adam Majzoub, Lillian O'Shay, Jessica Shields, and Nikota Welch.

REFERENCES

Adams, J.E., 1965, Stratigraphic-Tectonic Development of Delaware Basin, Bulletin of The American Association of Petroleum Geologists, vol 49, No. 11 p. 2140-2148.

Anderson, R.Y., Dean, W.E., Kirkland, D.W., and Snider, H.I., 1972, Permian Castile varved evaporite sequence, West Texas and New Mexico. Geological Society of America, v. 83, p. 59-85.

Anderson, R.Y., Kietrke, K.K., and Rhodei, D.J., 2001, Development of Dissolution Breccias, Northern Delaware Basin, New Mexico and Texas.

Anderson, R.Y., and Kirkland, D.W., 1980, Dissolution of salt deposits by brine density flow. Geology, v. 8, p. 66-69.

Buechner K. H., 1950, Life History, Ecology, and Range of The Pronghorn Antelope in Trans-Pecos Texas. The University of Notre Dame, The American Midland Naturalist. Vol 52 No. 2. p. 266.

Doctor, D.H., and Young, J.A., 2013, An Evaluation of Automated GIS Tools for Delineating Karst Sinkholes and Closed Depressions from 1-Meter LIDAR-Derived Digital Elevation Data. Proceedings of the 13th Multidisciplinary Conference on Sinkholes and the Engineering and Environmental Impacts of Karst, Carlsbad, NM, USA, 1 May–15 August 2013; p. 449–458.

Hill, C.A., 1996, *Geology of the Delaware Basin, Guadalupe, Apache, and Glass Mountains, New Mexico, and West Texas*: Society of Economic Paleontologists and Mineralogists, Permian Basin Section, Publication no. 96-39, p. 480.

Horak, R.L., 1985, Trans-Pecos tectonism and its affects on the Permian Basin, in Dickerson, P.W., and Muelberger, W.R., eds., Structure and Tectonics of Trans-Pecos Texas: Midland, Texas, West Texas Geological Society, p. 81–87.

Kelley, V.C., 1971, Geology of the Pecos Country, Southeastern New Mexico. New Mexico Bureau of Mines and Mineral Resources, Socorro, New Mexico, p. 78.

Klimchouk, A.B., 2000, Speleogenesis under deep-seated and confined setting. In: Klimchouk, A., Ford, D.C., Palmer, A.M. and Dreybrodt, W. (Eds.), Speleogenesis: Evolution of karst aquifers. National Speleological Society, Huntsville p. 244-260.

Klimchouk, A., 2007, Hypogene Speleogenesis: Hydrogeological and Morphogenetic Perspective: National Cave and Karst Research Institute Special Paper, no. 1, Carlsbad, NM.

Kirkland, D.W., 2003, An explanation for the varves of the Castile evaporites (upper Permian), Texas and new Mexico, USA: Sedimentology, v. 50, p. 899–920, doi: 10.1046/j.1365-3091.2003.00588.x.

Lee, MK., and Williams DD., 2000, Paleohydrology of the Delaware Basin, western Texas: overpressure development, hydrocarbon migration, and ore genesis. Bulletin of the American Association of Petroleum Geologists 84 (7): p. 961-974.

Liu, X., 2008, Airborne LiDAR for DEM Generation: Some Critical Issues, Progress in Physical Geography, Vol. 32, No. 1, p. 1-49.

Nance R., 1993, Application of the standard tablet method to a study of denudation in gypsum karst, Chosa Draw, southeastern New Mexico. MS Thesis, Greely, University of Northern Colorado: p. 82.

Scholle P.A., Goldstein R.H., and Ulmer-Scholle D.S., 2004, Classic upper Paleozoic reefs and bioherms of west Texas and New Mexico. Socorro, New Mexico Institute of Mining and Technology: p. 166.

Stafford, K., Nance, R., Rosales-Lagarde, L., and Boston, P., 2008a, Epigene and hypogene gypsum karst manifestations of the Castile Formation: Eddy County, New Mexico and Culberson County, Texas, USA: International Journal of Speleology IJS, v. 37, p. 83–98.

Stafford K.W., Rosales-Lagarde L., and Boston P.J., 2008b, Castile evaporite karst potential map of the Gypsum Plain, Eddy County, New Mexico and Culberson County, Texas: a GIS methodological comparison. J. Cave and Karst Studies. P. 83-98.

Stafford, K.W., Ulmer-Scholle, D., and Rosales-Lagarde, L., 2008c, Hypogene calcitization: Evaporite diagenesis in the western Delaware Basin: Carbonates Evaporites Carbonates and Evaporites, v. 23, p. 89–103.

Texas Speleological Survey, 2016, WallsMap: Texas Speleological Survey proprietary karst database. Texas Speleological Survey, Austin, Texas.

APPENDIX A

DETAILED LITERATURE REVIEW

LOCATION

The study area is located on either side of highway RM 652 along a 55 kilometer stretch across northern Culberson County, Texas. The road essentially runs from the west highway US62/180 intersection on the Texas / New Mexico border to the Culberson / Reeves county line to the east, ending just 16 kilometers short of Orla Texas. Physiographically, the study area is located in the Basin and Range province and is part of the largest desert in North America, the Chihuahuan Desert (Fig. A1).

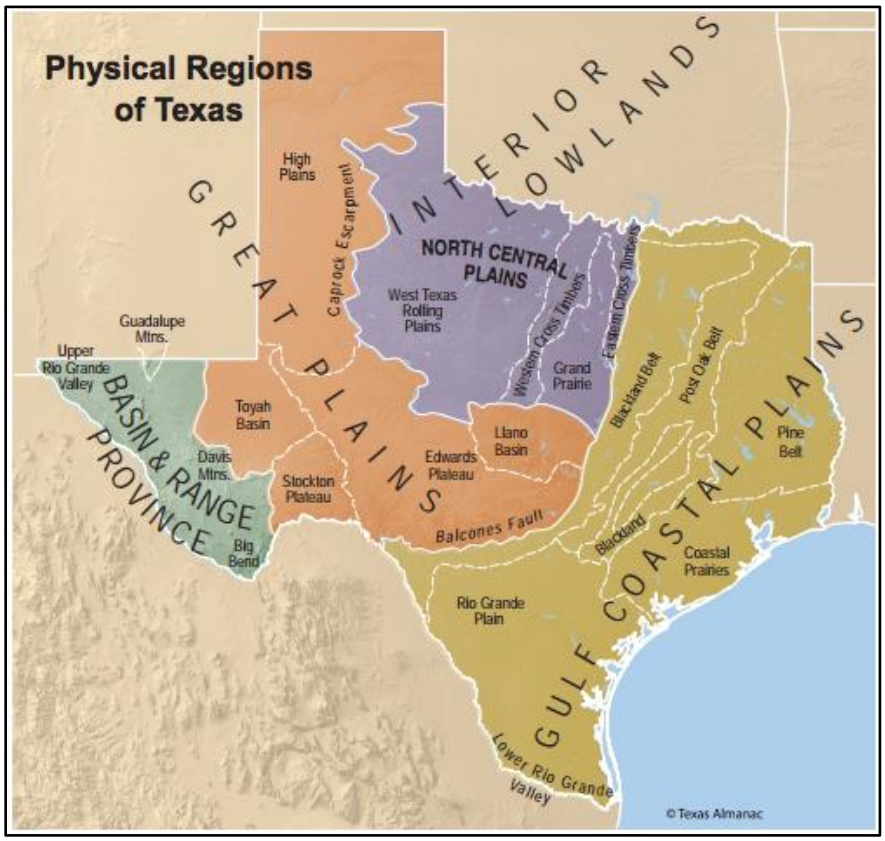

Figure A1: Physiographic regions of Texas (from www.texasalmanac.com)

This region contains nine counties and encompasses approximately 83,000 square kilometers of west Texas. The Trans-Pecos region is primarily a desert / semi-arid environment which results in scant precipitation, rapid evaporation, moderate winters and a large proportion of sunny days with short afternoon showers in the spring months. Agriculture in this region is very scarce due to the lack of moisture within the soil and limited amount of surface water available for irrigation. Precipitation is highly variable across the Trans-Pecos depending on topographic location, where the flats receive less than the mountainous regions due to the rain shadow effect. The study area along RM652 receives less than 300mm of precipitation per year and decreases as you move west towards Big Bend (south of Alpine and Marathon), which receives less than 250mm annually (Buechner, 1950). The average temperature of this area is less variable than the rainfall, with the mean summer temperatures varying from 24° to 30° Celsius; however, temperatures can reach upwards of 38°C.

The study area is also located in the heart of the Delaware Basin where over a billion years of the rock record is preserved; ranging from the 1.3 by old Precambrian basement to the less than 10,000 ybp Holocene sediments (Hill, 1996). The Delaware Basin is bound on its periphery by a series of exposed reef structures; to the west by the Apache Mountains, to the north by the Guadalupe Mountains, to the south by the Glass Mountains, and to the east by the Central Basin Platform. The large Gypsum Plain that encompasses the area is primarily blanketed by the Ochoan (later Permian) aged Castile and Rustler evaporite deposits at the surface (Fig. A2).

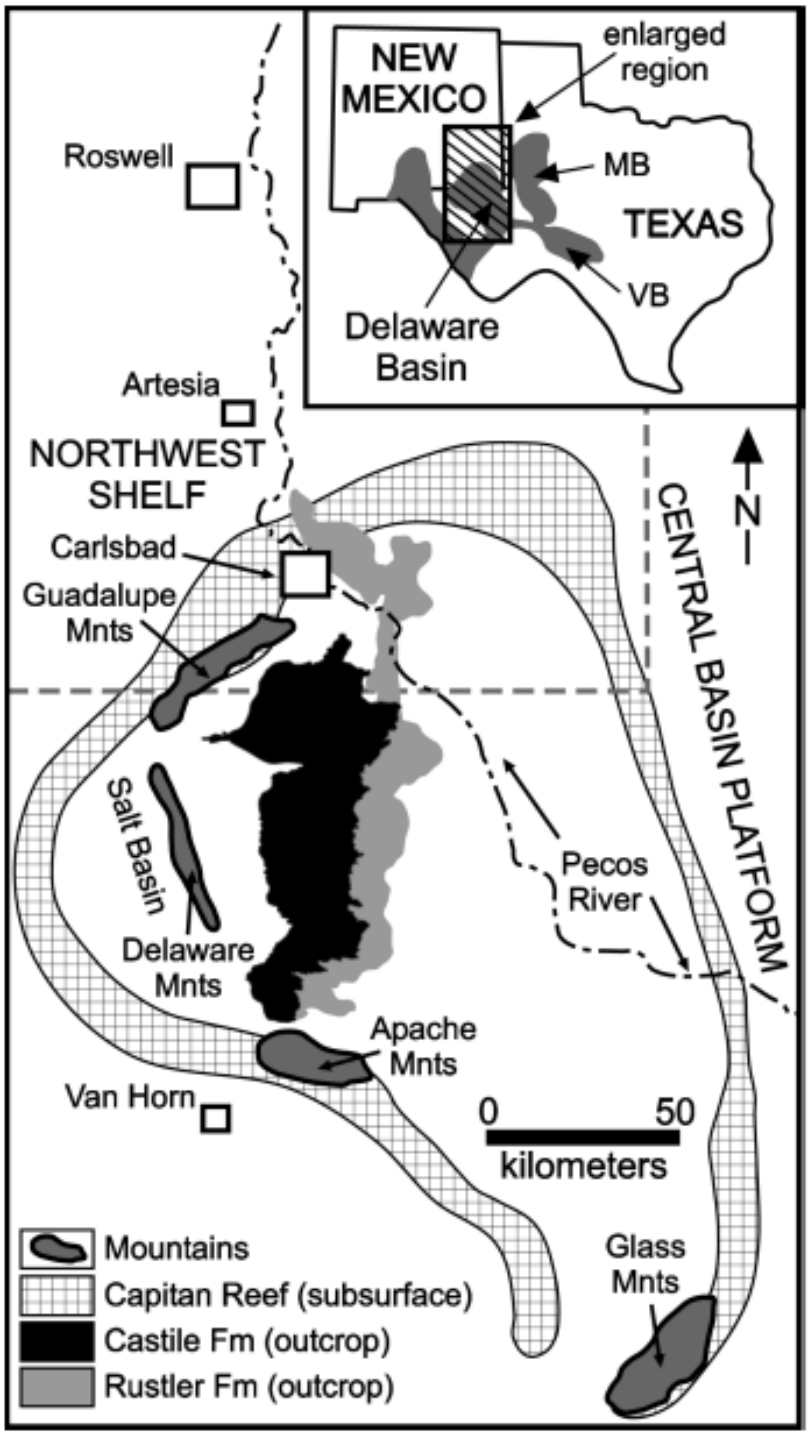

Figure A2: Location of the study area and Castile / Rustler formation outcrops (from Stafford et al. 2008a).

GEOLOGIC SETTING & BASIN EVOLUTION

The Delaware Basin of west Texas is one of the largest and oldest petroleum producing provinces in the United States, and as a result, it has been extensively studied. It spans a distance of approximately 320 kilometers long by 160 kilometers wide in the form of a large negative structural depression (Adams, 1965). The Delaware Basin is a part of a larger sedimentary basin referred to as the Permian Basin which covers approximately 223,000 square kilometers and encompasses 52 counties in Texas and southern New Mexico. Today, the Permian Basin, also known as the West Texas Basin, is comprised of five parts; the eastern Midland Basin, the Central Basin Platform, the western Delaware Basin, and the southern Marfa / Val Verde Basins (Fig. A3). These basins were extremely large depocenters for sediments during the late Paleozoic era (Hill, 1996).

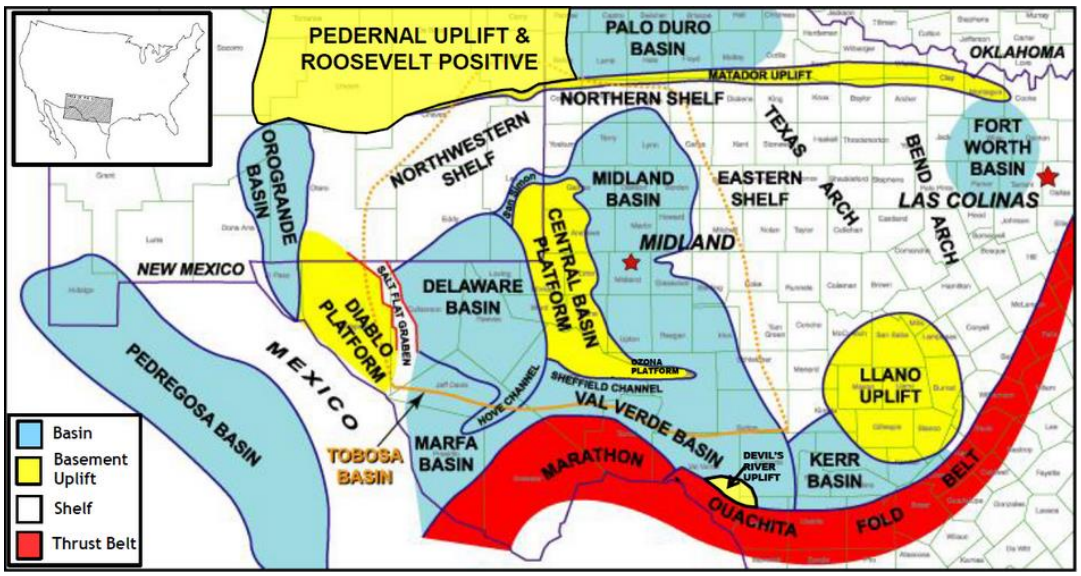

Figure A3: Major sedimentary basins within west Texas and southern New Mexico (from www.pxd.com)

Today, much of the Permian-aged rocks in southeastern New Mexico and the Trans-Pecos region are divided, from oldest to youngest, into the Wolfcampian, Leonardian, Guadalupian, and Ochoan series (Bachman, 1983). The center portions of the Delaware Basin are primarily dominated by Ochoan aged evaporites, while the perimeter of the basin is marked by the carbonate Capitan Limestone or reef complex. Even though this reef structure was formed over 280 million years ago, it has continued to influence the geologic history of the region today (Bachman, 1980).

Basin Formation / Tectonic Evolution

The first stage of the modern day Permian Basin development occurred from the late Precambrian to the late Mississippian. The ancestral Permian Basin occupied a passive margin type setting with weak crustal extension and low-rates of subsidence (Horak, 1985). Throughout the late Precambrian / Cambrian, the Transcontinental arch extended southeastward across New Mexico just adjacent to west Texas (Fig. A4).

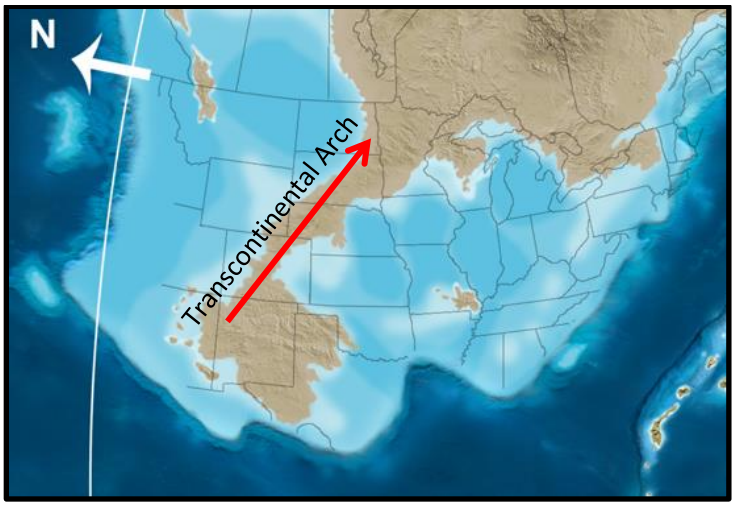

Figure A4: Displays the location of the Transcontinental Arch during the late Cambrian. (from Blakey, 2016)

The tectonic evolution of the area resulted in the conversion of this arch into a negatively sagging basin. Broad epeirogenic sags and swells covered this area with no important structural deformation (Horak, 1985). Adams (1965) suggests that the conversion of this ridge was caused by the shrinking and cooling of the underlying mantle and crustal rocks. Subsidence of this arch was, however, very slow and resulted in a flattened coastal plain where the Early Ordovician sea subsequently transgressed (Adams, 1965). The early Ellenburger Sea spread a large wedge of evenly bedded carbonate sediments offshore that rested on near shore clastic deposits derived from the erosion of the basement (Fig. A5). These sediments are now part of the Ellenberger Group of the Permian Basin. The carbonate shelves that formed were very wide and relatively shallow. They are well known for being one of the largest shallow-water carbonate platforms in the geologic record (Loucks, 2008). As a result of the minimal cross-shelf circulation, most of the Ellenburger limestone was quickly dolomitized after deposition (Adams, 1965).

Figure A5: Displays the shallow Early Ordovician Sea and subsequent deposition of the Ellenberger Formation (from Blakey, 2016).

Due to crustal warping that occurred near the end of the early Ordovician, a broad, shallow, gently dipping intracratonic basin began to form which is known as the Tobosa Basin (Galley, 1958). The deposition was dominated by “layer-cake” stratigraphy of shallow-water shelf carbonate deposits and fine-grained clastics that began filling the Tobosa Basin. By the Middle Ordovician, the shales and limestones of the Simpson Formation had covered the southern portion of present-day North America (Scotese et al., 1979). At this time, the Tobosa Basin became much deeper and extended further south (Hills, 1984).

By the Devonian, mass deposition of sediments was still occurring. However, there was a lack of extensive limestone deposition due to water depth towards the axis of the basin or increased acidity. By the Late Devonian, much of present day North America was covered by shallow seas which were poorly ventilated (Hills, 1984). Subsidence rates were quick but variable and some areas of the basin became starved due to slow clastic sediment deposition unable to keep pace. This variability caused seemingly erratic variations in limestone, dolomite, shale, and chert deposits. As structural stability temporarily re-established, forestepping of the carbonate shelves seaward resumed (Adams, 1965). During the Late Devonian and continuing into the Early Mississippian, an early transgression event occurred which deposited the Woodford Shale; the Tobosa Basin consisted primarily of dark gray and brown shales at this time. The development of a median ridge began to split the Tobosa Sag at the same time the area of active basinal subsidence extended northward into Kansas (Adams, 1965). Within the to-be Delaware Basin area, the black Woodford Shale was approximately 20-200 m thick and contained a large amount of organic / radioactive material.

Prior to the Permian, sediments were continually being deposited into the Ouachita Trough Basin to the southeast. These sediments accumulated within this deep marine basin slowly until the late Paleozoic Era. The second stage of the formation of the Permian Basin involved the collision of North American (Laurentia) and South American / African (Gondwana) during the Hercynian/Ouachita Orogeny to form Pangea (Fig. A6) (Hill, 1996). This collision occurred in the late Paleozoic, from the Late Mississippian through early Permian (320-265 Ma). The uplift of this trough produced the Ouachita Mountains which at the time ran all across Texas. Remnants of the Ouachita Trough can be seen in the Marathon Basin in west Texas, but for the most part, these uplifted Permian sediments are all covered by younger sediments. During the time of the Ouachita thrust front, minor thrusts and arches formed simultaneously. This compressional event formed the Muenster Arch, Bend Arch, and Red River arch which are located near the Ouachita thrust belt in northeastern Texas. During this time, there were a series of transgressions and regressions. Fluctuating nearshore environments with alternating non-marine channel fluvial-deltaic systems existed which deposited many sediments throughout Texas (Reneer, 1983).

The Tobosa Basin was heavily deformed due to movement along high angle basement faults and pre-existing zones of weakness (Horak, 1985). Both the Hercynian and Ouachita orogenies gave rise to the Central Basin Platform through associated horst-block faulting, which divided the Tobosa Basin into the western Delaware Basin, eastern Midland Basin, and the Val Verde Basin to the southeast. Basin subsidence continued as sediments were essentially shedding off of these uplifted areas (Ouachita Trough, Red River Arch, central New Mexico) and all migrating towards the Midland/Delaware basins (Hills, 1984). These sediments were often

reworked by waves and currents of the inland sea which resulted in the shallow fluvial-deltaic deposits seen throughout north central Texas.

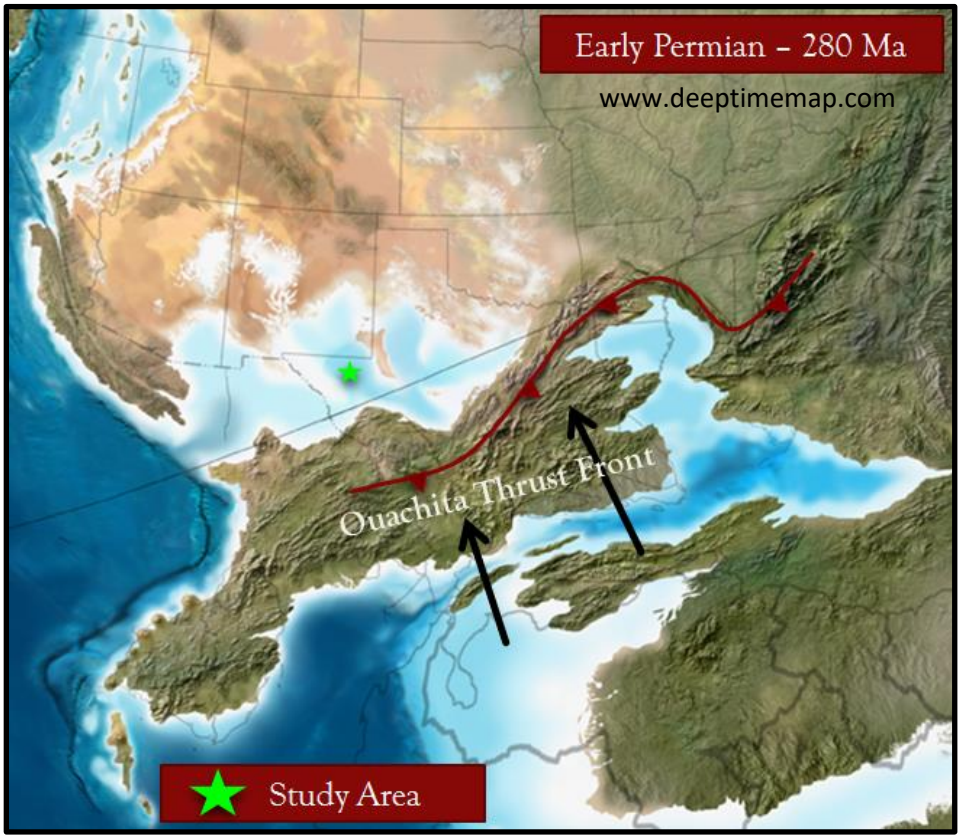

Figure A6: Theoretical view of the Oauchita thrust front during the Early Permian (from Blakey, 2016).

The blocks that formed from reactivation of high angle basement faulting rose and subsided independently. This crustal mobility, high heat flow, rapid basin subsidence, and filling characterize the essential depositional framework that controlled subsequent Permian sedimentation patterns (Horak, 1985). Some suggest that the Delaware Basin is similar to an aulacogen as its relationship to the Marathon/Ouachita thrust belt is nearly perpendicular. However, the faulting does not seem great enough at this time to support such claims. Therefore,

the Delaware Basin is considered to be a large intraplate basin and during this time was tilted to the east (Hills, 1984).

As previously mentioned, the Central Basin Platform uplift divided the Tobosa Basin. This uplift was composed of heavily folded and faulted Paleozoic rocks with a widespread unconformity that truncated Precambrian to Late Pennsylvanian aged rocks (Jones and Matchus, 1984). The folds that form the Central Basin Platform (northwest trending) are parallel to portions of the Marathon thrust front, supporting its Marathon/Ouachita orogeny origin. The Midland Basin that formed to the east is slightly larger than the Delaware Basin but also shallower. It covers approximately 40,000 square kilometers and at its deepest point contains around 4500 meters of sediment (Horak, 1985). Due to the compressional stresses applied by the Ouachita orogenic front, the Delaware Basin continually subsided during the Pennsylvanian. The uplift of the Glass Mountains to the south of the basin was followed by increased erosion and basin infilling. This infilling caused even more basin subsidence and loading that increased the relief of the rising Central Basin Platform and the sinking Delaware Basin (Hill, 1996). Because of the increased subsidence, the deepest portions of the basin were dominated by muds and dark siliceous shale accumulations and these regions were unable to form limestones.

The Delaware Basin remained a relatively deep water basin until the late Guadalupian Epoch. By the Late Pennsylvanian, broad carbonate shelf development continued along the perimeter of the newly divided basin and sections of the Central Basin Platform as a result of its equatorial location. This resulted in a deep starved shale basin as sedimentation in the Midland / Delaware basins was rather sparse due to the trapping of clastic material (eroded off the northeast highlands) behind the carbonate banks (Hills, 1984).

The next stage or phase of basin development occurred during the Permian. The Permian marks a time of high mobility rates and rapid filling of the basins with fine- to coarse-grained clastics; accompanied by the extensive development of reef-fringed carbonate and evaporite platforms (Horak, 1985). This phase encompassed a time span of 290-250 million years ago from middle Wolfcampian to Ochoan (Hills, 1996). Sedimentation and development of carbonate shelves occurred until the Delaware Basin remained as a small deep water depocenter (Adams, 1965). Rapid basin subsidence occurred which allowed for huge accumulations of sediments. Approximately 3500 meters to 5000 meters of sediments were deposited in the central portions of the Delaware Basin and 2000 meters on the outer shelf (Scholle et al., 2004). This massive sedimentation ultimately imposed a significant amount of compressional stress on the underlying rocks. The stress further squeezed up the Central Basin Platform to the east, and the Diablo Platform to the west, which provided even more accommodation space and clastic sources (Adams, 1965).

During this phase, the region was continually dividing into the Delaware Basin, Central Basin Platform, and Midland Basin (Hills, 1996). Tectonically speaking, the area during this time was relatively quiet until increased tilting occurred during the late Ochoan. Throughout the Delaware Basin, none of the earlier mentioned faults or folds that formed during the collision phase extended into the Permian rocks above the Wolfcampian (Hill, 1996). Some Permian rocks do have later aged folds (monoclines / anticlines) but were formed by differential compaction and basement abnormalities rather than compression during the Ouachita Orogeny (Hill, 1996). Initially, during the early Permian (Wolfcampian), large amounts of clastics were deposited that

thickened towards the center of the basin; these sediments are thought to be primarily distributed by sweeping turbidity flows off the flanks of the uplifted areas.

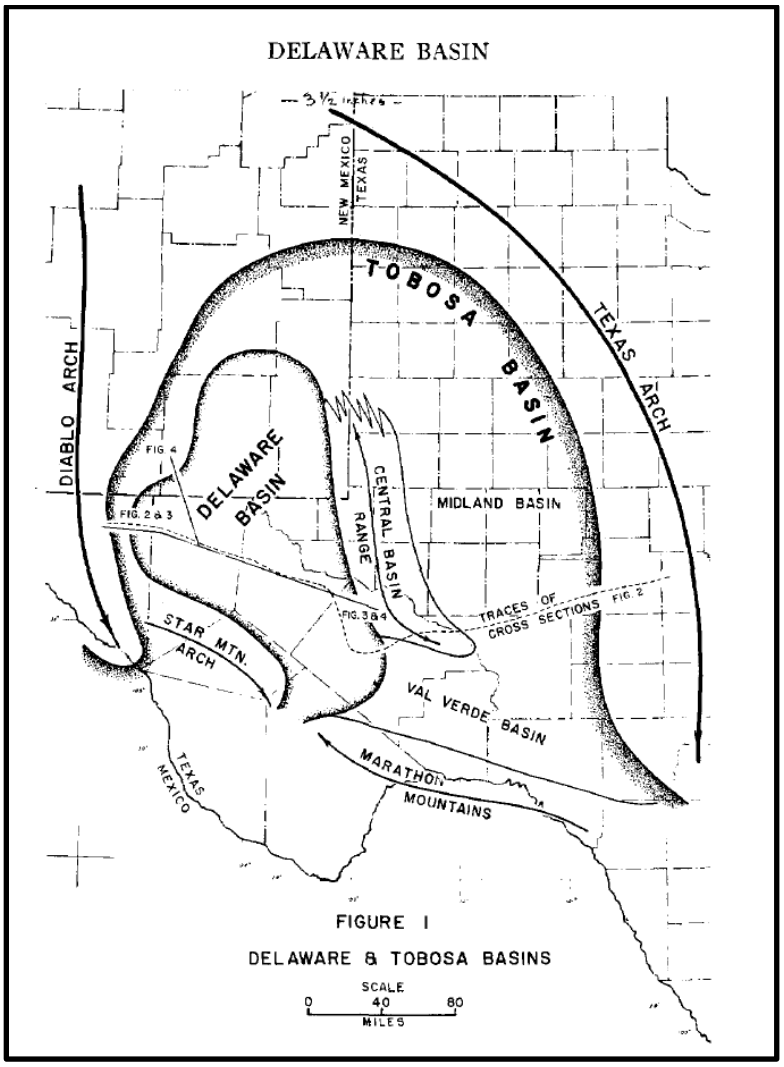

Figure A7: Delaware / Tobosa basin with associated channels and uplifts (from Adams, 1965).

The Wolfcampian Seas that filled the Delaware Basin at this time were agitated enough for thorough mixing of the water column. The mixing occurred due to increased activity in turbidity flows and circulation through carbonate channels in the shelf. The Hovey Channel and

Val Verde Basin to the south kept the surface water organically productive & aerated (Fig. A7) (Hills, 1984). The Wolfcampian was a time of the greatest basin subsidence within the southern Delaware Basin. Most of this subsidence occurred between the Marathon thrust sheets and Fort Stockton Uplift (Ewing, 1993).

This mixing of nutrients allowed for the proliferation of algae and other planktonic and nektonic forms that were the organics that ultimately created this highly productive hydrocarbon source rock (Adams, 1965). Normal marine salinity prevailed during this time as the marginal shelves and platforms were not sufficient to cause more than a mild restriction of circulation. The basin floor at the onset of the Wolfcampian was 300 meters deeper than the surrounding shelves. By the closure of the Wolfcampian deposition, the basin was approximately 450 meters deep and a large amount of organic material had been preserved (Hills, 1984).

Following the Wolfcampian, during the Leonardian, deposition of fine-grained clastic sediments continued into the central portion of the basin and subsidence across the Delaware and Midland basins was slower than in the early Permian. These sedimentation events were interrupted by cyclic carbonate wedges on the basin edges that extended as limestone beds basinward (Hills, 1984). These lenses of carbonate material offered sufficient overburden to compact the underlying fine-grained sediments and redirect pore waters which induced diagenesis. Some fine-grained clastic and sandstone beds are found basin-wide across the Delaware Basin and it is suggested that turbidity flows are the main cause of distribution (Adams, 1965).

By the end of the Leonardian, the Central Basin Platform, Diablo Arch, and the Star Mountain Arch became completely covered by bedded shelf limestones (Adams, 1965). In deeper

portions of the basin, these shelves were bordered by reefs which limited the movement of unconsolidated limestone muds. In the northern, shallower section of the basin, limestone detritus washed off the shelves and eventually became important petroleum reservoirs. The sediment outflowed through channels in the shelf/reef and caused the formation of alluvial fans which ultimately promoted the forestepping of reefs and seaward shelf growth (Adams, 1965). Evaporites were deposited on the broad shelves where the widespread restricted lagoons were located; and coarse-grained clastic sedimentation increased due to the renewal of uplifts in the northwest and increased subsidence (Adams, 1965). The underlying Wolfcamp sediments at this time were buried greater than 900 meters and the onset of an active petroleum system began (Hills, 1984).

The Late Permian sequences in the Delaware Basin are divided into two main series which are based on lithology and controlled by reef growth. The two main Upper Permian sequences are the Guadalupian Series (271-260 mya) and Ochoan Series (260-251 mya) (Adams, 1965) (Fig. A8). The Guadalupian Series represents the deposition of a thick, clastic, basin-filling facies, where the basin is continually filled with approximately 900-1200m of sediment (Hills, 1984). The periphery of the basin during this time was dominated by reef growth where the reef crest rose approximately 500 meters above the basin floor. The central portions of the basin were dominated by sandstones and siltstones, the marginal areas by limestone deposits, and the backreef formed evaporite lagoons (Adams, 1965). The Carbonate Reef formations that were deposited during this time were the Goat Seep Dolomite and the overlying Capitan limestone (Fig. A7). Contemporaneously, the backreef facies sediments of the Artesia Group were

deposited. These sediments included the Queen, Seven Rivers, Yates, and Tansil Formations (Scholle et al., 2004) (Fig. A8).

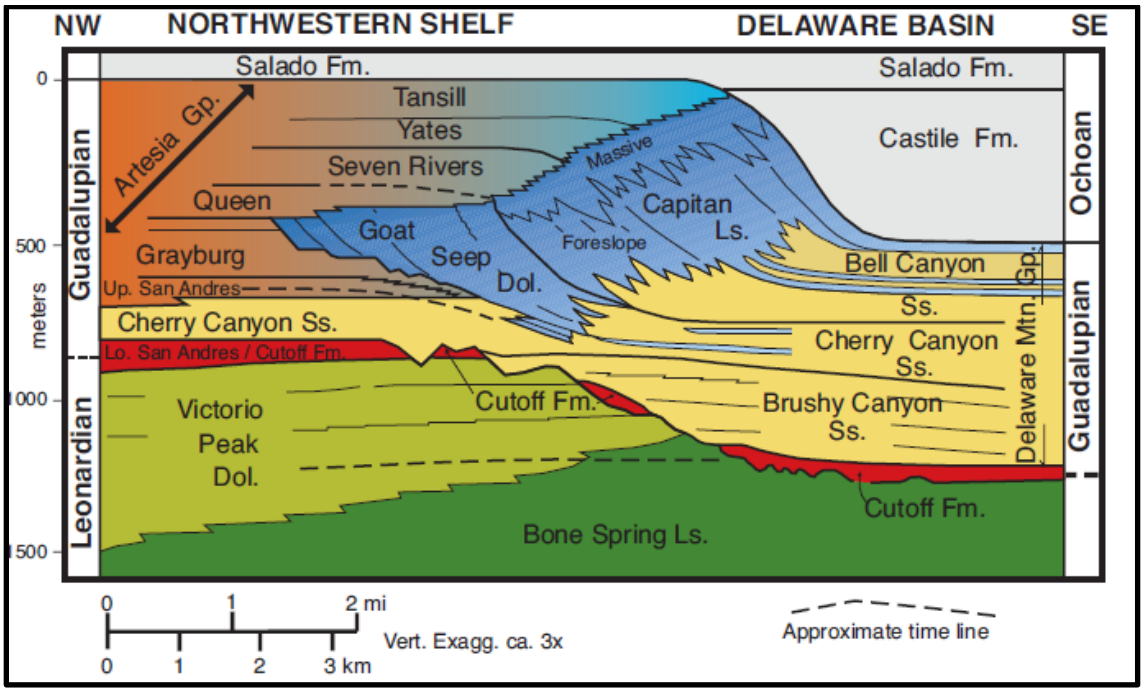

Figure A8: Delaware Basin cross section with lithologic units (from Scholle, et al., 2004).

Continued subsidence provided accommodation space for the central basin formations such as the Bell Canyon, Brushy Canyon, and Cherry Canyon formations to be deposited. These formations represent the clastic-dominated, primarily terrigenous sediments that were deposited during episodic sea-level fluctuations during the Guadalupian (Scholle, et al., 2004). In the closing stages of the Guadalupian, the Permian Basin became relatively tectonically stable (Adams, 1965). At this point, the middle Permian sediments previously deposited were 300 meters deeper. The Wolfcampian strata were now buried even further, now underneath 2400 – 3000 meters of overburden. These sediments were well within the catagenic zone where the

cracking of kerogen to hydrocarbons was actively occurring (Hills, 1984). Subsequently, the deposition of carbonate reefs and associated carbonate shelf sedimentation was terminated. Scholle and others (2004) postulate that this is largely due the increased basin restriction that began near the end the end of the Guadalupian.

Following the Guadalupian, the Ochoan series of evaporite formations were deposited (260 to 251 mya). The continual restriction of the evaporite seas resulted in the deposition of the first phase of evaporite filling within the Delaware Basin; this basin filling formation is the Castile Formation. The Castile Formation is a unit that reaches approximately 550 meters in thickness at the northern section of the basin (Scholle et al., 2004). The massive evaporite deposition occurred due to increased growth of the Capitan Reef effectively closing off of the previously mentioned Hovey Channel. This closure excluded the Delaware Basin from its direct connection to the open ocean. The Castile began filling the Delaware Basin and the evaporite sedimentation spread across the shelfal regions (Fig. A8). The Castile consists of millimeter-scale interbedded laminae of gypsum, anhydrite, organic matter and calcite (Fig. A9). These interbedded layers have been interpreted to be varves with over 209,000 cycles present in the Castile alone (Scholle et al., 2004).

The distinct characteristic of large scale, laterally-continual laminations and lack of shallow water sedimentary structures suggest that the Castile was deposited in deep water (Scholle et al., 2004). The Castile sediments infilled the Delaware Basin and evaporite deposits spread across the region. The next Ochoan unit deposited was the Salado Formation. The Castile Formation grades conformably into the Salado and unlike the Castile, it extends far beyond the

margins of the Delaware Basin and is the first unit to cross the Capitan Reef from basin to shelf (Kelley, 1971; Hills, 1996).

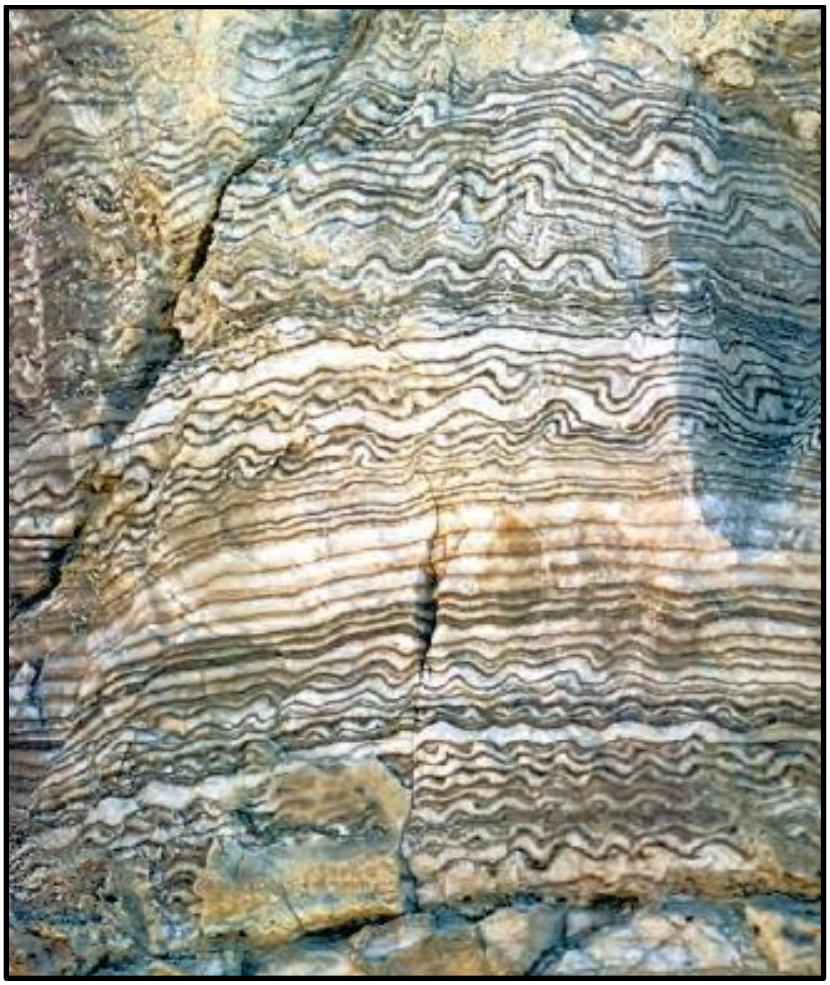

Figure A9: Laminated Varves of the Castile formation (Scholle, et al 2004).

The distinct characteristic of large scale, laterally-continual laminations and lack of shallow water sedimentary structures suggest that the Castile was deposited in deep water (Scholle et al., 2004). The Castile sediments infilled the Delaware Basin and evaporite deposits spread across the region. The next Ochoan unit deposited was the Salado Formation. The Castile

Formation grades conformably into the Salado and unlike the Castile, it extends far beyond the margins of the Delaware Basin and is the first unit to cross the Capitan Reef from basin to shelf (Kelley, 1971; Hills, 1996). The Salado Formation contains laminated halite, anhydrite, sylvite, other evaporites, and minor amounts of siliciclastic material. Beyond the borders of the basin, the Salado typically lies directly on Guadalupian carbonate rocks. However, in modern times, due to its extreme solubility, the Salado does not generally appear in outcrop throughout the Delaware Basin (Scholle et al., 2004). Due to uplift on the west side of the Delaware Basin, eastward tilting of the basin continued throughout the late Permian and created more accommodation space for deposition of the Salado and subsequent Rustler formations (Hill, 1996). Hill (1996) suggests that the faults on the western flank of the Central Basin Platform were acting as a hinge line for tilting, and ultimately caused the Capitan forereef to dip approximately 20-35 degrees to the east. The tilting resulted in thicker Salado deposition to the east (600 meters) and thinner deposits to west (300 meters) where it overlies the Guadalupian backreef Tansil Formation (Fig. A8).

The final evaporite of the Ochoan depositional sequence is the Rustler Formation. The Upper Permian Rustler Formation unconformably overlies the Salado. Hill (1996), postulates that this pre-Rustler unconformity marks a time of extensive Permian tilting and erosion where the Salado has been completely removed. This erosion results in the Rustler Formation lying directly on top of the Castile Formation within the Delaware Basin or on Guadalupian evaporites in the backreef. Furthermore, Leng (1937) suggests that the Rustler Formation sits directly on a truncated surface of the Salado, which indicates that uplift and tilting occurred at time of deposition during the Ochoan. During this time, a sea-level incursion and subsequent

transgressions and regressions deposited cyclic layers of large-scale limestone-dolomite and anhydrite-gypsum deposits (Hill, 1996).

These deposits, like the Salado, covered the basin and extended into the backreef behind the Capitan Reef. The Castile, Salado, and subsequent Rustler formations essentially became the caprocks for the region cutting off most vertical migration of fluids. Not enough organic material was present in the anhydrite to generate any commercial quantity of petroleum (Hills, 1984). In addition to their sealing characteristics, these evaporite minerals provide the primary host rock for karst development throughout the Delaware Basin region. The final deposition event of the Ochoan occurred at the closure of Rustler time (Hill, 1996). The Dewey Lake Red Beds represent continental deposition as sea level dropped. Eastward tilting and uplift of the Delaware Basin was still underway during the late Ochoan which resulted in an angular unconformity between the Dewey Lake, underlying Rustler Formation, and overlying Triassic rocks. This final regression of the Permian sea deposited largely siliciclastic-rich and iron-rich continental deposits (Hill, 1996).

Following Ochoan time, at the Permian-Triassic boundary (250mya) the Delaware Basin began to shift from a largely marine sedimentation depocenter to a positive area dominated by clastic sedimentation. The Delaware Basin was uplifted at this time and the marine environment was replaced by lacustrine, fluvial, and deltaic environments (Hill, 1996). Erosion and dissolution dominated the region from the end of the Ochoan time to the late Triassic. The depositional hiatus lasted approximately 25-30 million years until sedimentation picked back up with the widespread deposition of the Chinle Group in the late Triassic (Lucas and Anderson, 1993). Following the Triassic, the Jurassic was also a time of much erosion, dissolution, and slow sedimentation. During this time many of the underlying Permian and Triassic rocks were karstified (Hill, 1996).

The Stable Platform Phase of the Delaware Basin occurred from the middle Triassic to the late Cretaceous (230-80mya). Pangea rifting began and split apart North and South America (Mojave Senora megashear to the southwest). By the end of the stable platform phase and subsequent launch of the Laramide phase, the Farallon Plate began to converge with the western coast of North America (Fig. A10). The back-arc deformation from the plate convergence formed the Chihuahua Trough of the Late Jurassic to mid-Cretaceous. The Chihuahua Trough experienced marine transgressions that spread carbonate sediments across the region and into the Delaware Basin throughout the Cretaceous (Hill, 1996). Areas such as the Glass Mountains, Apache Mountains, and portions of the Guadalupe Mountains were also covered by this event. The Laramide phase occurred from 80 mya to 40 mya and marked the end of the stable platform phase. During the late Cretaceous to early Tertiary, Laramide Orogeny convergence rates had increased significantly pushing the Farallon Plate far enough to permanently uplift the entire Rocky Mountain region above sea level (Hill, 1996). After the uplift, the Delaware Basin was tilted eastward approximately 4° and elevated 1.2 kilometers above sea level on the western side, which is where it remains today (Horak, 1985). Even though the area was being largely affected by the Laramide, there was very little tectonic expression in the Delaware Basin. Hills (1963) postulates that much of the folding, thrusting, and frontal range formation like what is seen in Colorado and Wyoming was absorbed by the rigid massifs of New Mexico and the Texas panhandle.

The volcanic phase of the Delaware Basin followed the Laramide phase and occurred from 40 mya to 30 mya. This phase involved weak extension and crustal thinning that occurred

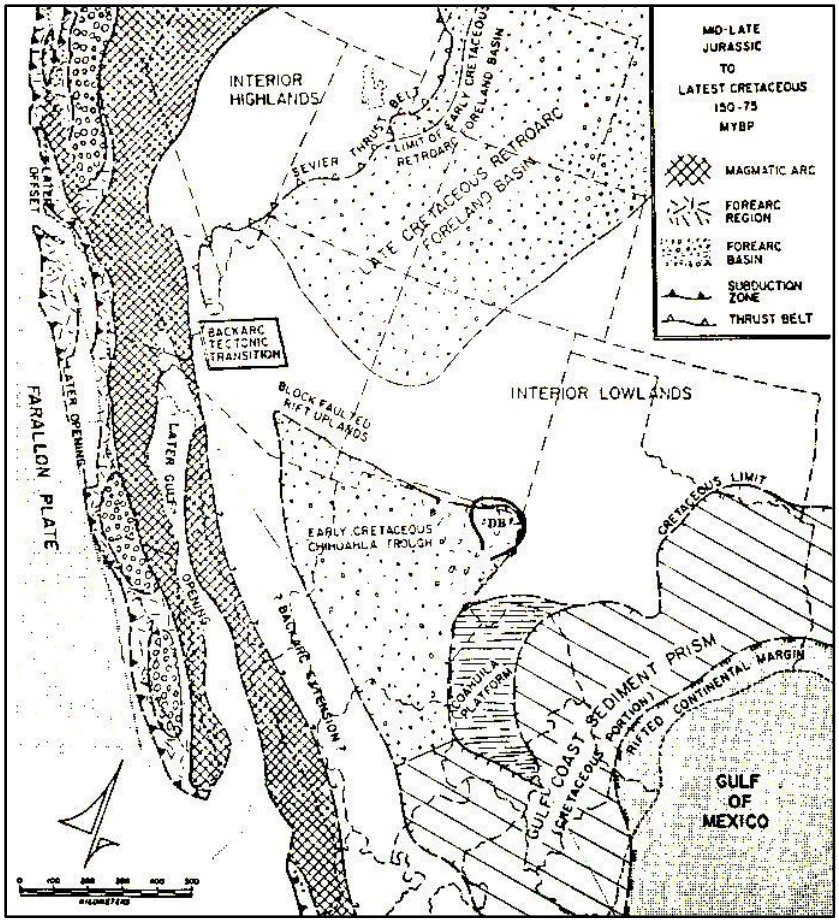

Figure A10: Paleotectonic map of western North America from late Jurassic to late Cretaceous; showing the position of the trough, Delaware Basin, and Farallon thrusting (from Dickinson, 1981).

during a time of transition from a north-northwest compressional regime (Laramide) to an extensional (Basin and Range) regime (Hill, 1996). Alkalic belts and igneous complexes were emplaced across the trans-pecos region during this time and were not associated with large scale rifting events. The large domes of igneous rocks found near the Glass Mountains as well as all of the intrusive dikes found throughout the Delaware Basin were emplaced during this time (Hill, 1996). The cause of the sudden increase in magmatic activity and change from compression to

extension is not unambiguous. Keith (1978) postulates that the onset of magma generation and emplacement into the upper crust may have been a result of either the steepening of Farallon subduction or the sinking of a detached piece of the continental plate.

Subsequent to the Laramide and Volcanic phases, the Basin and Range extensional phase commenced and lasted from 30 mya to present. Basin and Range extension is expressed all across the Delaware Basin and to the southwest coast of the United States. This region is characterized by crustal extension, high heat flow, normal faulting, and graben formation (Horak, 1985). Throughout the Oligocene, high heat flow had begun and continued through the Miocene. It is postulated by Green and Ringwood (1969) that the heating up of the Delaware Basin may have been caused by rising diapiric magma in the mantle which began to partially melt rocks and heat hydrothermal fluids. During the late stages of the Basin and Range, it is proposed that northeast extension was replaced by northwest west extension which resulted in the formation of a northeast trending graben (Hentz and Henry, 1989). The easternmost basin found in the Basin and Range province, the Salt Flat Graben, was formed by northwestern extension that dropped this region during the Tertiary. This graben is approximately 100 kilometers long and 16 kilometers wide and has been a primary depocenter for fluvial and lacustrine deposits in the far west Delaware Basin since the middle Tertiary (Scholle et al., 2004). Because there is no natural basin outlet, the Salt Flat Graben today is dominated primarily by evaporite deposits in a saline wet pan playa.

GUADALUPIAN SERIES STRATIGRAPHY

The Guadalupian Series, named after the Guadalupe Mountains, was characterized by the massive growth of stratigraphic carbonate reefs around the periphery of the Delaware Basin, siliciclastic deposition in the center of the basin, and a mixed clastic-carbonate deposition in the shallow backreef shelf lagoon (Fig. A8) (Hills, 1996). The marginal reefs continued to grow throughout the Guadalupian to keep up with the continually subsiding Delaware Basin. The reefal carbonates deposited during this time were the Goat Seep Dolomite and overlying Capitan Limestone. Within the backreef that formed behind the Capitan Reef, the Guadalupian Artesia Group shelfal redbed evaporites and dolomites were deposited. These sediments included the Grayburg, Queen, Seven Rivers, Yates, and Tansil formations (Scholle et al., 2004). The primary siliciclastic/terrigenous deposition during this time occurred in the central portion of the Delaware Basin where the Bell Canyon, Brushy Canyon, and Cherry Canyon formations were deposited (Fig. A11).

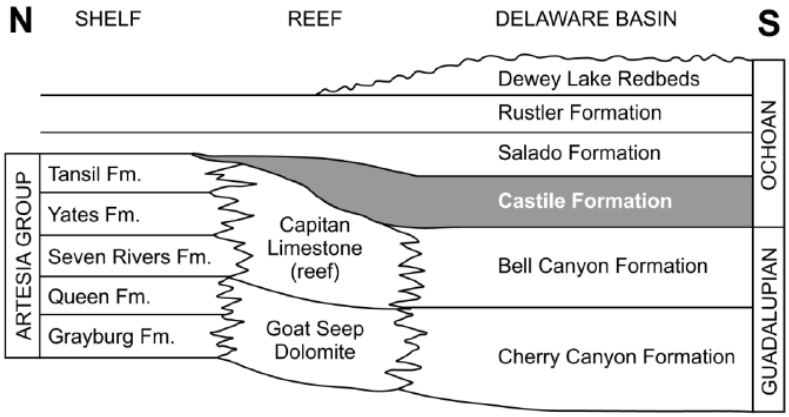

Figure A11: Stratigraphic section from the Shelf (North) to Delaware Basin (South) of lithologic units within the study area (adapted from Scholle et al., 2004).

The Cutoff Formation marks the onset of the Guadalupian and the highest level of the Permian Sea where it slowly subsided until the late Guadalupian. The deposits within the Guadalupian are important because they record the early developmental stages of the Delaware Basin. These Guadalupian sediments lay the groundwork for future deposition of the Ochoan series evaporites.

Backreef Facies: Artesia Group (Guadalupian)

The Artesia Group of the Guadalupian contains five major formations including, from oldest to youngest, the Grayburg, Queen, Seven Rivers, and Tansil formations. These formations were all deposited shelfward of the Guadalupian Capitan and Goat Seep reefal deposits (Nance, 1993). The Artesia Group displays considerable cyclicity and a swift change in lithofacies as you move from the reef deposits of the Capitan complex to the evaporitic backreef facies (Kelley, 1971). The cyclicity is likely a result of alterations in current flow and minor sea level changes on a minor to medium scale of 0.3 to 2.5 meters (Smith, 1974b). Throughout Guadalupian time, as the Permian sea reduced in size, the backreef facies changed from red beds to evaporites to dolomite to limestones towards the reef front (Hill, 1996).

Grayburg Formation

The Grayburg Formation is the first unit deposited during Guadalupian time within the backreef facies. The Grayburg Formation represents a carbonate bank that is approximately 385 meters thick and thins basinward as a result of erosion, depositional thinning, and changes in facies (Franseen, 1989). Within the inner-shelf carbonate facies, the Grayburg consists of primarily calcareous dolomite that is light gray, grayish-orange and pinkish-gray with interbedded

fine-grained sandstones. Within the shoreward evaporite facies, it contains primarily gypsum, red sandstone, silt, and clay (Hill, 1996). The proportion of carbonate to clastic material is about 3:1 in the upper Grayburg and 2:1 in the lower. The transition between the Grayburg and overlying Queen Formation marks a major change in depositional style, from a carbonate bank to a reef complex (Hill, 1996).

Queen Formation

The Queen Formation is lithologically quite similar to the Grayburg Formation in the near-reef and reef areas, but it contains approximately twice the proportion of clastic material (Kelley, 1971). The carbonates within the Queen Formation are pale-orange, relatively fine-grained, dolomites that are typically two meters thick (Hill, 1996). Like the Grayburg, the Queen lithology rapidly shifts northward into thinner red sandstone, siltstone, and mudstone with dolomite. The transition between the silty upper beds of the Queen Formation and overlying Seven Rivers is easily distinguishable (Sarg, 1985).

Seven Rivers Formation

The Seven Rivers Formation is sandwiched between the overlying Yates and underlying Queen formations. It is approximately 150-200 meters thick and predominately composed of thinly-bedded, grayish-yellow, fine-grained dolomite. As seen in figure A11, the Seven Rivers grades laterally into the Capitan Limestone from its evaporite facies to dolomite to pure limestone (Hill, 1996). This unit shows the classic facies transition from an evaporative tidal flat or lagoon to more carbonate deposition near the Capitan Reef.

Yates Formation

The siliciclastic rich Yates Formation is bound at the top and bottom by the Tansil and Seven Rivers formations respectively (Kelley, 1971). Similar to the Seven Rivers, the Yates Formation contains two main facies, the carbonate, and evaporite. Within the carbonate facies, it contains a thinly-bedded, tan to gray dolomite with interbedded fine-grained, reddish-brown sandstones. The evaporite facies is dominated by gypsum, red mud, and silt. Unlike the previous two formations, which are predominately dolomite, two-thirds of the Yates Formation is composed of siltstone and sandstone. This large siliciclastic component allows for easy differentiation between bounding formations (Hill, 1996).

Tansil Formation

The final backreef facies deposit of the Guadalupian is the Tansil Formation, which disconformably underlies the Salado Formation. Within the carbonate facies, the Tansil contains thinly-bedded, light-gray dolomites. Within the evaporite facies, the Tansil is composed of gypsum and red clay/silt. The Tansil grades laterally into the upper Capitan Reef where bedding becomes thicker, more fossiliferous, and less dolomitic (Hill, 1996).

Reef Facies: (Guadalupian)

Goat Seep Dolomite & Capitan Limestone

During the middle Guadalupian, the Permian sea had shrunk to the size of the Delaware Basin. Prior to this time, the periphery of the basin was dominated by low relief carbonate bank/ramp type deposits (Hill, 1996). Conditions during the middle Guadalupian supported the growth of massive sponge-algal reef formation. This massive reef growth resulted in the

formation of the middle Guadalupian Goat Seep dolomite and late Guadalupian Capitan Limestone (Hill, 1996). The Goat Seep Dolomite consists of 400 meters of massive, finely-crystalline, light gray dolomite that conformably underlies the Capitan Limestone. The Goat Seep Dolomite differs from the younger Capitan Limestone in the following ways: it is composed primarily of dolomite, is more bedded with a lower angle shelf edge, has different fauna species, and contains more of the foreslope facies with fewer large clasts (Hill, 1996). The Capitan Limestone, commonly referred to as the Capitan Reef, has been extensively studied and described as it is one of the most famous fossil reefs on record. As seen in figure A2, the Capitan Reef forms a large 650-kilometer long horseshoe bend around the periphery of the Delaware Basin. Approximately 65 kilometers of this Formation can be seen at the surface to the northwest in the Guadalupe Mountains (Hill, 1996). The Capitan Limestone is divided into two main members, the massive reef, and forereef; together they comprise a thickness of approximately 450 to 600 meters. The Reef member is comprised of fine-grained, light gray, limestone and forms massive cliffs. The larger forereef facies is composed of light pink dolomitic limestone with some reefal debris and forms a weathered slope (Hill, 1996).

Basinal Facies: Delaware Mountain Group (Guadalupian)

The Delaware Mountain Group (DMG) within the Delaware Basin contains three main formations and many members. The DMG consists of the Brushy Canyon, Cherry Canyon, and Bell Canyon formations which represent nearly 1200-1600 meters of stratigraphically cyclic siliciclastic / carbonate slope and basinal sediments (Dutton et al., 2005). The Basinal Facies of the DMG were deposited in the lowstand interval of the classic reciprocal sedimentation model of the Delaware Basin (Fig. A12). During the Guadalupian and DMG depositional phase, the

Permian Sea had shrunk to the extent of the Delaware Basin. The basin was relatively deep and as previously mentioned, began building the large carbonate Goat Seep and Capitan Limestone Reef complex. The onset of reef buildup restricted siliciclastic sediment flow from across the entire Permian Basin to just the Delaware Basin (Hill, 1996). The DMG contains a variety of sedimentary structures from cross laminations, scour and ripple marks to areas that contain no sedimentary structure at all.

Figure A12: Illustrating sediment flow into the Delaware Basin during a LST (from sepmstrata.org).

Brushy Canyon Formation

The lowermost unit of the basinal facies is the Brushy Canyon Formation. The Brushy Canyon is the coarsest-grained rock of the facies and contains fine to medium-grained channelized sandstone beds (3m) with little to no detrital carbonate debris from the reef – forereef (Hill, 1996). The Brushy Canyon is almost entirely a thick-bedded, tan to brown, sandstone unit with some minor occurrences of limestone in the most basinal regions. Unlike the overlying Cherry Canyon and Bell Canyon, there are many coarse-grained sandstone beds. The Brushy Canyon marks the first cyclic deposit of the basinal facies and each cycle typically contains a period of channeling that is overlain by a coarser sandstone unit (Hill, 1996). As defined by Gardner and Sonnenfeld (1996) the boundary between the Brushy Canyon and overlying Cherry Canyon can be easily identified by the presence of an organic-rich lutite.

Cherry Canyon Formation

The Cherry Canyon Formation is approximately 300 to 400 meters thick and contains thinly-bedded / laminated sand and siltstones that make up the upper portion of the forereef slope below the Capitan Limestone. Like the Brushy Canyon, the Cherry Canyon displays cyclic sedimentation and is represented by alternating sandstone and thin nodular limestone beds (Hill, 1996). These cycles are typically three to six meters in thickness and represent sea level fluctuations. The clastic component of these laminations is derived from the basinward deposition of sand and silt that has bypassed the shelf areas during lowstands. Unlike the Brushy Canyon, the Cherry Canyon contains large tongues of limestone that are correlated back to the forereef deposits of the Goat Seep Dolomite (Hill, 1996).

Bell Canyon Formation

The uppermost unit of the Delaware Mountain Group is the Bell Canyon Formation. Similarly, to the Cherry Canyon, the primary components of the Bell Canyon are fine-grained sandstone and coarser-grained siltstones with the same cyclic interbedded limestones. Specifically, the Bell Canyon Formation is very well-sorted and primarily composed of quartz with a fairly high percentage of feldspar (20%) (Hill, 1996). The bedded limestone units thicken and grade laterally into the Capitan Limestone. Past the reef and into the backreef facies, the Bell Canyon grades laterally into interbedded dolomites, limestones, and evaporites of the Artesia Group (Bachman, 1980).

OCHOAN SERIES STRATIGRAPHY

The Ochoan series of evaporite formations were deposited from 260 to 251 mya (Fig. A11). The continual restriction of the evaporite seas resulted in the deposition of the first phase of evaporite filling within the Delaware Basin. The Ochoan represents a massive change in sedimentation from siliciclastics and limestones to evaporites. The closure of the Hovey Channel, due to the reef growth, cut off the Delaware Basin's interaction with the open ocean. This largely restricted and highly saline environment promoted the deposition of a massive sequence of evaporites during the Ochoan including gypsum, anhydrite, and halite (Hill, 1996).

Castile Formation

The basal unit of the Ochoan series is the Castile Formation. The Castile outcrops extensively throughout the study area and is a largely unbroken, massive to laminated gypsum deposit with interbedded halite (Hendrickson and Jones, 1952). The Castile Formation reaches approximately 550 meters thick and grades conformably upward into the overlying Salado Formation (Scholle et al., 2004). The thickness of the Castile increases to the east and ultimately pinches out completely to the northwest as it moves up the base of the reef escarpment (Hill, 1996). The Castile consists of millimeter-scale interbedded laminae of gypsum, anhydrite, organic matter and calcite. Within the subsurface, the sulfates remain dehydrated as anhydrite but hydrates near the surface to gypsum (Stafford, 2008). These interbedded layers have been interpreted to be varves with over 209,000 cycles present in the Castile alone. During dryer and more saline periods, sulfate and halite laminations were deposited and during less saline periods

calcite laminae dominated (Stafford, 2008). The presence of these distinct characteristics of large-scale, laterally-continuous laminations and lack of shallow water sedimentary structures suggests that the Castile was deposited in deep water (Scholle et al., 2004). The Castile, in its lower portion, consists of grayish white gypsum and the upper member generally contains massive, white gypsum (Kelly, 1971).

Within the study area, the presence of unique secondary calcitization of the gypsum is not uncommon. Calcitization of the Castile results in the creation of geomorphic features called "castile buttes" at the surface and "castile masses" in the subsurface. The buttes are essentially large hills standing up to 30 meters above the Gypsum Plain, which represent the secondary replacement of anhydrite by calcite (Hill, 1996). Stafford et al., (2008c) suggests that the calcitization is a result of either bacterial sulfate reduction or thermal sulfate reduction.

Salado Formation

The second unit deposited during the Ochoan time in the Delaware Basin was the Salado Formation. Beyond the periphery of the basin, the Salado typically sits directly on Guadalupian carbonate rocks; however, the Salado Formation is not seen throughout the study area as it is extremely soluble and has been dissolved away (Scholle et al., 2004). Laminated halite, anhydrite, sylvite, other evaporites, and minor amounts of siliciclastic material are present throughout the Salado Formation. The Salado represents a much more saline and shallow water depositional environment compared to the Castile and Rustler as it contains approximately 84% chloride, 12% sulfate, and 4% siliciclastic material (Scholle, et al 2004). The halite beds are clear, coarse-grained, and often laminated but lack the calcite laminae seen in the Castile Formation (Hill, 1996). The thickness of the Salado varies greatly due to original deposition and subsequent

dissolution. The lower and upper members of the Salado equate to about 500 meters total but in some areas it is nonexistent. Following the Salado, the Rustler Formation is conformably deposited on the upper Salado solution-breccia zone that formed as a result of groundwater leaching (Hill, 1996).

Rustler Formation

The final evaporite deposit of the Ochoan depositional sequence is the Rustler Formation. During Rustler time, sea-level transgressions and regressions deposited cyclic layers of large-scale limestone-dolomite and anhydrite-gypsum deposits (Hill, 1996). These deposits, like the Salado, covered the basin and extended into the backreef behind the Capitan Reef. The Rustler is divided into five major parts; these include, the Virginia Draw (unnamed), the Culebra Dolomite, the Tamarisk Member, the Magenta Dolomite Member, and the Forty-niner Member (Bachman, 1980). The two dolomite members, the Magenta and Culebra, mark the two major advances in sea level during Rustler time. The basal member consists of 15 meters of dark siltstone overlain by 10 meters of fine, thinly-bedded, crystalline dolomite (Hill, 1996). The first transgressive unit, the Culebra Dolomite, is a six to nine meters thick unit and is a distinctive marker bed in the Rustler. It is a finely crystalline, brownish-gray, thinly-bedded dolomite with many layers containing abundant vugs of two to ten millimeters in diameter (Bachman, 1980). The Tamarisk Member represents a regressive sequence with higher salinities and is identified as a light gray halite and anhydrite with minor siltstone. The second major transgression deposited the Magenta Dolomite Member which consists of six to eight meters of red to brown dolomite. Lastly, the regressive Forty-Niner Member marks the uppermost member of the Rustler Formation. In surface

exposures, it is massive gray gypsum with a small red siliciclastic component and within the subsurface, it is typically anhydrite (Bachman, 1980).

Dewey Lake Red beds

The Dewey Lake Red Beds rest conformably on the Rustler Formation and are primarily composed of thin beds of reddish-brown siltstone and finer-grained sandstone with occasional small-scale ripple marks (Bachman, 1980). These beds mark the retreat of the final advance of the Permian Sea. As the Dewey Lake transitions into the underlying Rustler, there are several minor occurrences of selenite veins. The depositional environment for the Dewey Lake is controversial but has been proposed to be deposited in a shallow water lagoon or continental delta environment (Hill, 1996).

KARST AND SPELEOLOGY

Karst manifestations, for all intents and purposes, involve the dissolution of soluble rock, mobility of ions in solution through permeable conduits, and potential re-precipitation of dissolved ions. The dissolution and subsequent formation of karst typically occurs in rocks that are highly soluble, such as, limestone, dolomite, and evaporites. Karst landscapes are typically identifiable by, but not limited to, the presence of surficial features such as cavernous porosity (caves) and sinkholes, as well as karstic brecciation and karren (Stafford et al., 2008a). Speleogenesis, on the other hand, is essentially the driving mechanism for the formation of karst. As defined by Klimchouk (2000), speleogenesis involves "the creation and evolution of organized permeability structures in a rock that have evolved as the result of dissolutional enlargement of an earlier porosity." Speleogenesis plays a role in the formation of caves and other surficial karst features; however, it is not limited to these manifestations. Speleogenesis covers the whole gamut of carbonate/evaporite dissolution and evolution of soluble rocks from intergranular pore spaces on the micron scale to large scale cavernous porosities (Stafford et al., 2008c).

The dissolution of carbonate/evaporite rocks and formation of karst, specifically caves, principally develops in three basic diagenetic settings: 1) oceanic/coastal, within rocks that are diagenetically immature with high porosity and permeability; 2) hypogenic, where ascending fluids dissolve soluble rock in a confined (no surface exposure) setting, and 3) epigenic, where meteoric water flow is sourced from the surface (unconfined) and infiltrates rocks below (Ford and Williams, 2007).

Oceanic/coastal karst generally forms contemporaneously with the deposition of the surrounding surface rock such as in coastal limestones. A key element that differentiates coastal karst from inland karst is that it is dealing with diagenetically immature rock (Michael et al., 2013). Many limestone coasts are immature and have not undergone deep burial; because of this, these coastal limestones, often referred to as eogenetic rocks, naturally contain coarser grains and higher porosities. Additionally, due to being diagenetically young, coastal rocks typically contain the highly soluble calcium carbonate polymorph aragonite, which is easily dissolved into cavernous porosities (Michael et al., 2013). The combination of all the aforementioned characteristics represents the complexity and factors involved in the initial development of coastal karst.

Epigene karst formations are considered the opposite of hypogene karst where caves develop in an unconfined environment by the activity of descending surficial waters. These karst systems are typically shallow and localized; where fluid flow is largely driven by gravitational gradients (Klimchouk, 2007). Within the unsaturated vadose zone, epigenic caves typically form more vertical passages due to gravity-driven fluids. In the saturated or phreatic zone, epigenic caves typically form more solutionally widened passages that are often elliptical in shape due to being formed while completely filled with water. Epigenic caves in general exhibit scalloped walls and form along fracture planes that are then solutionally widened (Stafford et al., 2008a).

Hypogenic karst, unlike both coastal and epigenic karst, forms where pressurized groundwater is moving through a confined bed or stratum (typically ascending) and most importantly, is completely removed from surficial processes during formation (Klimchouk, 2007). However, hypogene karst can, in fact, create landforms after original cave formation.

Hypogenetic karst features are often expressed at the surface as relict features where they are decoupled from the environment in which they were originally formed (Klimchouk, 2007). These relict features, such as collapsed sinkholes, were originally formed in a confined (hypogenic) setting but were then overprinted by epigene (unconfined) processes (Stafford et al., 2008a).

Differentiating between hypogene and epigene sinkholes involves analysis of their geomorphic expression. Hypogene originated sinkholes (collapsed) typically form by ascending fluids and the upward stoping of subsurface voids which produces steep-sided, near-circular features. Epigene originated sinkholes form by descending fluids and the subsequent solutional incision / dissolution forming elongated sinks (Ford and Williams, 2007). Within the hypogene speleogenetic realm, fluid pressure and migration is powered by both free and forced convection. The free convection pressure regime is driven by buoyancy, density variations, and temperature; forced convection flow is driven by differences in hydraulic head across an area, where water is flowing from areas of high pressure to areas of low pressure (Tóth, 1999).

Within the Delaware Basin, the primary formation that contains large cavernous porosity is within the soluble gypsum and anhydrite of the Castile Formation. The karst features of the Delaware Basin are one of the most prominent displays of gypsum karst in North America (Hill, 1996). The Castile evaporite, due to being naturally highly soluble, has undergone a significant amount of dissolution since deposition and contains an extensive amount cave and karst features (Stafford et al., 2008a). The type of caves found within the study area formed by both epigene and hypogene processes. However, as previously mentioned, understanding which exact processes affected the Castile and the timing of dissolution can be difficult as many hypogene caves have been overprinted by epigene processes. Throughout the Castile, many karst features

can be found from surficial karren, sinkholes, and karstic breccias to large complex caves that have been affected by multiple processes (Stafford, 2006). Through the use of spatial analysis and field mapping, Stafford et al., (2008b) predicts that there are over 10,000 karstic depressions within the study area where over half of these anomalies are collapse structures which likely formed originally by hypogenic processes (Fig. A13.) The remaining features (45%) are likely of epigenetic origin but knowing if they are just overprints of this process is nearly impossible.

Sinkhole morphology within the study area ranges from highly elongated to nearly circular. By the use of a ratio between the length and width of a specific sinkhole, Stafford et al., (2008b) determined that an approximate determination can be made to whether or not the sinkhole was developed by hypogene or epigene processes. Sinks that have a width/length ratio greater than 0.5 (nearly circular) are likely a result of hypogene processes and are exposed at the surface as collapse sinks. Sinks that have a length/width ratio that is less than 0.5 (elongated) are likely a result of epigene processes or overprinting and are exposed at the surface as elongated solutional sinks (Stafford, et al. 2008a). However, it is important to keep in mind that these ratios are merely an estimation to quickly classify the origin of a sinkhole. Analysis of the surface morphology of a sinkhole is only one clue into its formational history as these exposures can be obscured by significant overprinting (Stafford et al., 2008a). Analyzing additional features such as cave risers, channels, cupolas, blanket-dissolution breccias, breccia pipes, and evaporite calcitization can help to uncover the formational history of the karst within the Castile Formation.

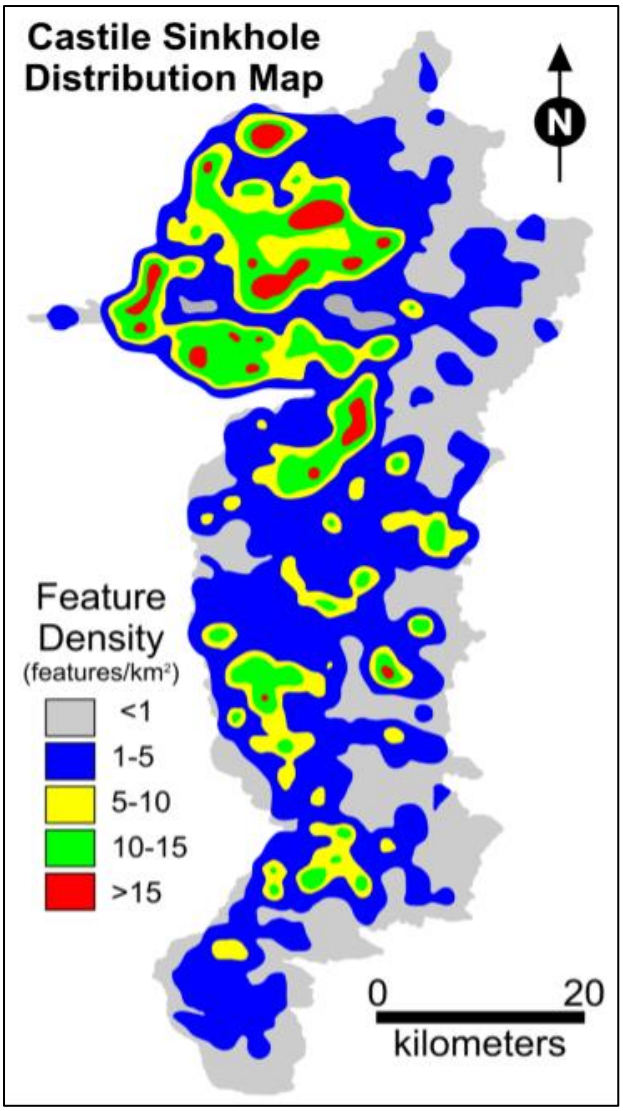

Figure A13: Illustrating the spatial distribution of karstic depressions derived from GIS analysis (from Stafford et al., 2008b).

Notable geomorphic features such as wall scallops, cupolas, and risers are present within the Castile Formation. Scallops indicate the presence of fast moving fluid and are typically indicative of flash flooding of meteoric water within an epigenic or overprinted hypogenic cave (Stafford et al., 2008a). In addition to scallops, epigene caves within the Castile typically contain

narrow openings that develop primarily along fracture planes that are solutionally widened and relatively shallow. On the other hand, some caves within the Castile Formation exhibit large ceiling cupolas, risers, and half tubes which indicate a hypogene origin (Fig. A14) (Stafford et al., 2008a). These risers and cupolas are a result of ascending fluids moving from areas of high pressure to areas of low pressure and dissolving out domal structures in the ceiling of cave passages. Half tubes represent additional ascending fluid that dissolves out channels along cave passage walls and ceilings (Stafford et al., 2008a).

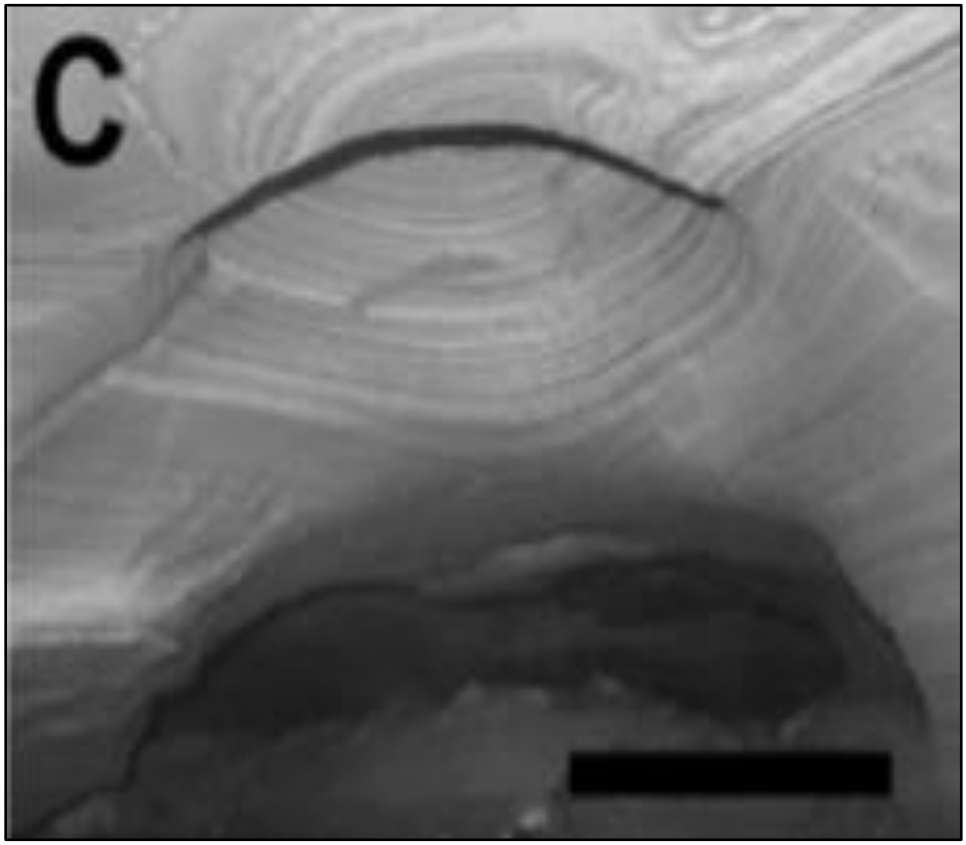

Figure A14: Typical ceiling cupola in a series of domal ceiling features. (black bar is 1 meter) (Dead Bunny Hole, Culberson Co. TX) (from Stafford et al., 2008a).

In addition to surface dissolution (sinkholes, shallow caves, depressions) more evidence of extensive dissolution can be seen throughout the study area and Delaware Basin through the presence of both lateral and vertical dissolution features. As the name implies, lateral dissolution involves the lateral movement of chemically-unsaturated water that penetrates and dissolves easily soluble intrastratal evaporite beds (Hill, 1996). In the case of the Delaware Basin, this dissolution often results in large scale collapse horizons containing “blanket-dissolution breccias” (Fig. A15) (Anderson et al., 1972).

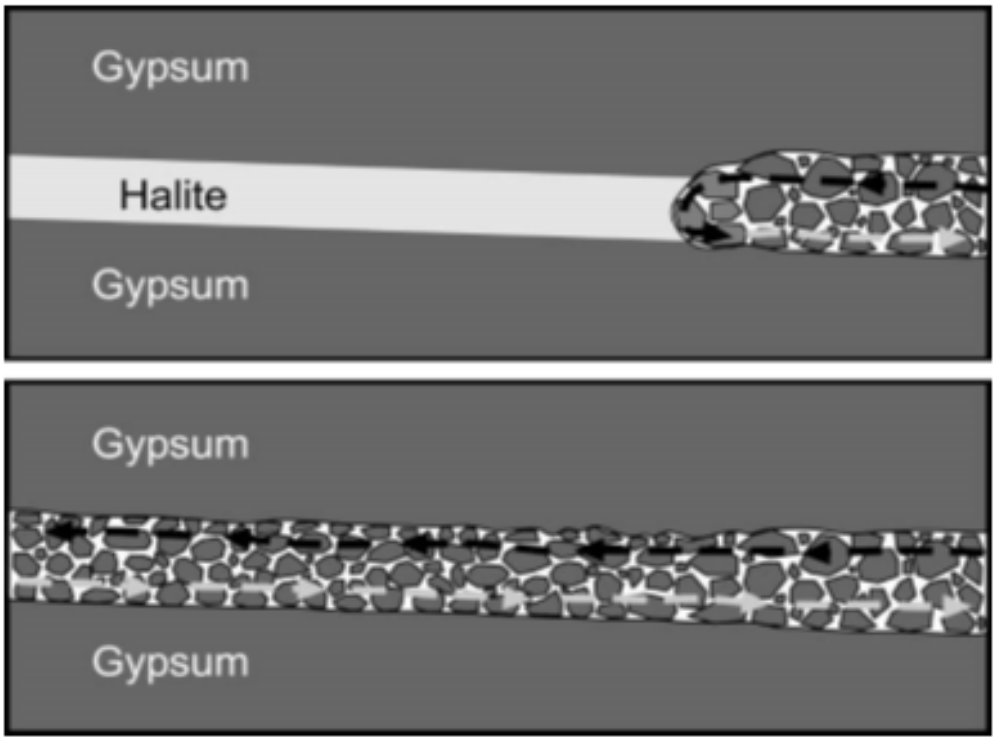

Figure A15: Diagram illustrating the process in which blanket-dissolution breccias form through the dissolution of halite where arrows represent fluid movement (from Stafford, 2015).

Lateral dissolution breccia forms as halite (Salado) material is dissolved and the overlying gypsum (Castile) can no longer support its own weight and collapses into angular

fragments. These dissolution breccias can be traced across the basin and have been correlated to the still present Salado evaporites that are located on the eastern side of the Delaware Basin (Anderson, et al 1978). In addition to lateral dissolution, vertical dissolution can take the shape of breccia pipes. This sort of dissolution requires a source of relatively fresh pressurized water, and a fracture network along which this water can rise and dissolve/remove evaporites (Hill, 1996). Similar to blanket breccias, vertical breccia pipes also form by fluid only it is ascending in this case to create vertical conduits filled with angular brecciated material (Fig. A16) (Anderson and Kirkland, 1980). Most of these brecciated zones, either vertical or lateral, are often calcitized (Stafford et al., 2008a) and appear as a dark gray variant of the typical light colored Castile (Fig. A17).

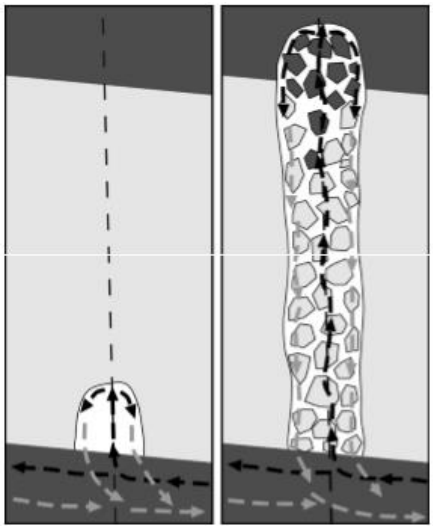

Figure A16: Diagram illustrating the process in which breccia pipes form through the dissolution of halite where arrows represent fluid movement (from Stafford, 2015).

Figure A17: Photograph taken in road cut off of highway RM652 displaying a fragmented calcitized zone of the Castile Formation that is likely a result of a breccia pipe.

The calcitization that can be seen in the Delaware Basin is in the form of the previously mentioned castile buttes, masses, and brecciated zones. It is reported that these calcitized zones primarily occur due to three main processes. These processes involve Bacterial Sulfate Reduction (BSR), Thermochemical Sulfate Reduction (TSR) and meteoric calcitization (Stafford et al., 2008c). Both thermal and bacterial sulfate reduction require the presence of sulfate rocks (gypsum) and an organic carbon source (Machel 1992). As the sulfate is reduced, a saturated fluid containing both hydrogen sulfide and calcite precipitates out as native sulfur and secondary calcite (Machel, 1992). BSR occurs when sulfate reducing bacteria acts as the catalyst and typically thrives in temperatures between 0 and 80°C (Ehrlich, 1990). TSR typically occurs between 100 to 180°C (Machel, 1998) and does not require the active involvement of microbial organisms. Understanding the limitations and requirements of both of these calcitization methods can help determine which form calcitized the Castile within the study area. Even though Kirkland and Evans (1976) propose that the calcitization within the Delaware Basin is primarily a result of BSR, the thermal regime of the Delaware Basin supports both types.

GIS LiDAR

To understand acting hydrological processes it is important to be able to delineate sinkholes, especially when trying to mitigate potential geological hazards within a karst landscape. This can be accomplished by land survey and mapping of karst features; however, over the past decade, the capabilities and accuracy of Geographic Information Systems (GIS) have allowed for sinkhole analyses of very large areas with great efficiency. One helpful form of GIS is in the application of remote sensing through the use of airborne Light Detection and Ranging (LiDAR), which has long been recognized for its potential and ability to delineate sinkhole locations (Newton, 1976). LiDAR is a specific remote sensing technique that can accurately measure the elevation or intensity of features on the land surface by the use of laser light pulses fired out of an airplane. There are often multiple reflection surfaces (i.e. trees, buildings, water) between the airplane and bare earth (Fig. A18) (Zhu et al., 2014). LiDAR data is often referred to as "point clouds" which contain many readings over a desired area and require post-process filtering to analyze accurately. By measuring the delay of the return time of the pulses, one can classify each of the returns into a specific surface so "noise," anything but bare earth (terrain) in this case, or unwanted data can be excluded from analysis (Zhu et al., 2014).

Modern LiDAR units are typically capable of detecting multiple returns or reflection surfaces. Generally, the first return measures the tree canopy, the second measures middle canopy or lower vegetation, and the final or last return measures the bare earth (Liu, 2008). This post-processed surface (last return) can be converted into a Digital Elevation Model (DEM), which displays the elevation of the terrain. Digital Elevation Models can be analyzed to determine

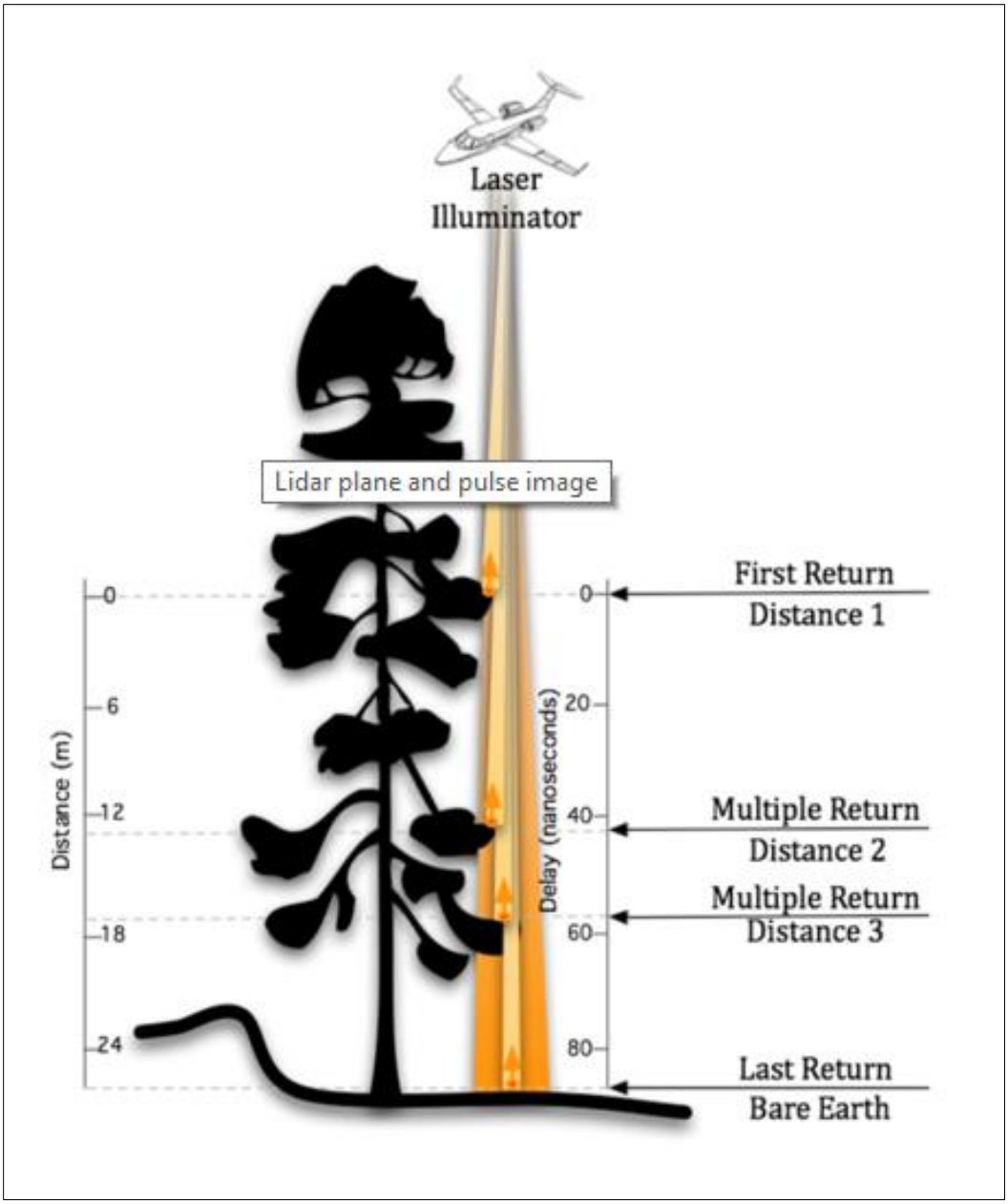

Figure A18: Diagram illustrating the process in which multi-return LiDAR is obtained (from ucanr.edu).

locations that have undergone subsidence or collapse and have proven to be extremely useful in the delineation of sinkholes and other karstic lineaments. Although LiDAR can be a very useful

tool for interpretation, like conventional survey methods, it is not without limitation. It is important to keep in mind that LiDAR and DEM creation involves many different factors such as varying modeling methods, interpolation algorithms, and DEM resolution (Liu, 2008). While being cognizant of these limitations and variables, high-density and high-accuracy LiDAR data can provide as a great platform to identify karst sinkholes at a high resolution.

REFERENCES

Adams, J.E., 1965, Stratigraphic-Tectonic Development of Delaware Basin, Bulletin of The American Association of Petroleum Geologists, vol 49, No. 11 p. 2140-2148.

Anderson, R.Y., Dean, W.E., Kirkland, D.W., and Snider, H.I., 1972, Permian Castile varved evaporite sequence, West Texas and New Mexico. Geological Society of America, v. 83, p. 59-85.

Anderson, R.Y., Kietzke, K.K., and Rhodes, D.J., 1978, Development of dissolution breccias, northern Delaware Basin and adjacent areas, bulletin 159. New Mexico Bureau of Mines and Mineral Resources, Socorro, New Mexico, p. 47-52.

Anderson, R.Y., Kietrke, K.K., and Rhodei, D.J., 2001, Development of Dissolution Breccias, Northern Delaware Basin, New Mexico and Texas.

Anderson, R.Y., and Kirkland, D.W., 1980. Dissolution of salt deposits by brine density flow. Geology, v. 8, p. 66-69.

Bachman, G.O., 1980, Regional Geology and Cenozoic History of the Pecos Region, Southeastern New Mexico: U.S. Geological Survey Open File Report 80-1099, p. 117.

Bachman, G.O., 1983, Regional Geology of Ochoan Evaporites, Northen Part of Delaware Basin: New Mexico Bureau of Mines and Mineral Resources, Open File 184.

Blakey, R., 2016, Deep time Maps™: www.deeptimemaps.com.

Buechner K. H., 1950, Life History, Ecology, and Range of The Pronghorn Antelope in Trans-Pecos Texas. The University of Notre Dame, The American Midland Naturalist. Vol 52 No. 2. p. 266.

Dietrich, J.W., Owen, D.E., Shelby, C.A, and Barnes, V.E., 1995, Geologic atlas of Texas: Van Horn-El Paso Sheet. University of Texas Bureau of Economic Geology, Austin, Texas, 1 sheet.

Doctor, D.H.; Young, J.A., 2013, An Evaluation of Automated GIS Tools for Delineating Karst Sinkholes and Closed Depressions from 1-Meter LIDAR-Derived Digital Elevation Data. Proceedings of the 13th Multidisciplinary Conference on Sinkholes and the Engineering and Environmental Impacts of Karst, Carlsbad, NM, USA, 1 May–15 August 2013; p. 449–458.

Ewing, T.E. 1993, Erosional margins and patterns of subsidence in the Late Paleozoic West Texas Basin and New Mexico; in love, et al. (eds.), Carlsbad region, New Mexico and West Texas: Geol. Soc., Guidebook, 44th Ann Field Conf., p 115-166.

Ford D.C. & Williams P.W., 2007 – Karst hydrogeology and geomorphology. John Wiley & Sons: p. 562.

Ford D.C.2006 – Karst geomorphology, caves, and cave deposits: A review of North American contributions during the past half century. Geological Society of America, Special Paper 404.

Franseen, E.K**.**, 1988, The Grayburg and Queen Formations (Permian) and the Associated Erosion Surface at the Shelf Margin, Western Escarpment, Guadalupe Mountains, West Texas: *in* Reid, S.T., Bass, R.O. and Welch, P, eds., Guadalupe Mountains Revisited, Texas and New Mexico, West Texas Geological Society Publication 88-84, p. 155-162.

Franseen, E.K., Fekete, T.E. and Pray, L.C., 1989, Evolution and Destruction of a Carbonate Bank at the Shelf Margin: Grayburg Formation (Permian), Western Escarpment, Guadalupe Mountains, Texas: *in* Crevello, P.D., Wilson, J.L., Sarg, J.F. and Read, J.F., eds., Controls on Carbonate Platforms and Basin Development, Society of Economic Paleontologists and Mineralogists Special Publication #44, p. 289-304.

Gardner, M. H., and Sonnenfeld, M. D., 1996, Stratigraphic changes in facies architecture of the Permian Brushy Canyon Formation in Guadalupian Mountains National Park, west Texas, *in* DeMis, W. D., and Cole, A. G., eds., The Brushy Canyon play in outcrop and subsurface: concepts and examples: guidebook: Society of Economic Paleontologists and Mineralogists Permian Basin Section Publication 96-38, p. 51–59.

Gradstein, F. M., Ogg, J. G., and Smith, A. G., 2004, A geologic time scale 2004: Cambridge University Press, p. 589.

Hendrickson, G. E., and Jones R. S., 1952, Geology and groundwater resources of Eddy County, New Mexico: New Mexico Bur. Mines Mineral Resources, Groundwater Rept. 3, p. 109.

Hentz, T.F., and Henry, C.D., 1989. Evaporite-hosted native sulfur in Trans-Pecos Texas: relation to late phase Basin and Range deformation. Geology, v. 17: p 400-403.

Hill, C. A., 1996, *Geology of the Delaware Basin, Guadalupe, Apache, and Glass Mountains, New Mexico, and West Texas*: Society of Economic Paleontologists and Mineralogists, Permian Basin Section, Publication no. 96-39, p. 480.

Hill, C.A., 1989, The Evolution of the Delaware Basin- Preliminary Results. SEPM , Cave Research Foundation, Albuquerque, NM p. 467.

Hill, C.A., 1996, Geology of the Delaware Basin, Guadalupe, Apache and Glass Mountains: New Mexico and West Texas. Permian Basin Section – SEPM, Midland, TX, p. 480.

Hills, J.M., 1984, Sedimentation, Tectonism and hydrocarbon generation in Delaware Basin, West Texas and southeastern New Mexico: American Association of Petroleum Geologists Bulletin, v. 68, p. 260-267.

Horak, R.L., 1985, Trans-Pecos tectonism and its affects on the Permian Basin, in Dickerson, P.W., and Muelberger, W.R., eds., Structure and Tectonics of Trans-Pecos Texas: Midland, Texas, West Texas Geological Society, p. 81–87.

Kelley, V.C., 1971, Geology of the Pecos Country, Southeastern New Mexico. New Mexico Bureau of Mines and Mineral Resources, Socorro, New Mexico, p. 78.

King, P.B., 1942, Permian of west Texas and southeastern New Mexico. American Association of Petroleum Geologists Bulletin, v. 26, no. 4, p. 535-563.

Klimchouk, A.B., 2000, Speleogenesis under deep-seated and confined setting. In: Klimchouk, A., Ford, D.C., Palmer, A.M. and Dreybrodt, W. (Eds.), Speleogenesis: Evolution of karst aquifers. National Speleological Society, Huntsville p. 244-260.

Kirkland, D.W., 2003, An explanation for the varves of the Castile evaporites (upper Permian), Texas and new Mexico, USA: Sedimentology, v. 50, p. 899–920, doi: 10.1046/j.1365-3091.2003.00588.x.

Kirkland, D.W., and Evans, R., 1976, Origin of limestone buttes, Gypsum Plain, Culberson County, Texas. American Association of Petroleum Geologists Bulletin, v. 60, p. 2005-2018.

Lee, MK., and Williams, DD., 2000, Paleohydrology of the Delaware Basin, western Texas: overpressure development, hydrocarbon migration, and ore genesis. Bulletin of the American Association of Petroleum Geologists 84 (7): 961-974.

Lee, J. (*ed*), 1996, GYPKAP Report Volume 3. Southwestern Region of the National Speleological Society, Alamogordo, New Mexico, p. 69.

Lorenz, J.C., 2006, Assessment of the potential for karst in the Rustler Formation at the WIPP site. Sandia National Laboratories, Report SAND 2005-7303, p. 102.

Loucks, R.G., 2008, Review of the Lower Ordovician Ellenburger Group of the Permian Basin, westTexas,http://www.beg.utexas.edu/resprog/permianbasin/PBGSP_members/writ_synth/Ellenburger%20report.pdf , Website accessed March 26, 2016.

Lucia, F.J., 1972, Recognition of evaporite–carbonate shoreline sedimentation, in Rigby, J.K., and Hamblin, W.K., eds., Recognition of Ancient Sedimentary Environments: Society of Economic Paleontologists and Mineralogists, Special Publication 16, p. 160–191.

Michael J. L., and Mylroie J.E., (eds.), 2013, Coastal Research Library, vol. 5, Springer, Dordrecht, The Netherlands, 429 p. (eBook – PDF format).

Nance R., 1993, Application of the standard tablet method to a study of denudation in gypsum karst, Chosa Draw, southeastern New Mexico. MS Thesis, Greely, University of Northern Colorado:.p. 82.

Newton, J.G., 1976, Early Detection and Correction of Sinkhole Problems in Alabama, with a Preliminary Evaluation of Remote Sensing Applications: Alabama Highway Department, Bureau of Research and Development, Research Report no. HPR- p. 76, 83.

Poppenga SK., Worstell BB., Stoker JM., and Greenlee SK., 2010, Using selective drainage methods to extract continuous surface flow from 1-meter lidar-derived digital elevation data. U.S. Geological Survey Scientific Investigations Report 2010–5059, p. 12.

Sarg, J. F., 1985, Permian shelf calcrete, Shattuck Member, Queen Formation (southeast New Mexico)-shelfal expression of Middle Guadalupian fall in sea level: West Texas Geological Society Bulletin, v. 24, p. 8-16.

Scholle P.A., Goldstein R.H. and Ulmer-Scholle D.S., 2004, Classic upper Paleozoic reefs and bioherms of west Texas and New Mexico. Socorro, New Mexico Institute of Mining and Technology: p. 166.

Stafford, K.W., 2015, Evaluation of Existing Geologic Conditions along RM 652: Initial Characterization of Karst Geohazards Associated with RM 652 in Culberson County, Texas: TxDOT rep., p. 1–71.

Stafford, K., Nance, R., Rosales-Lagarde, L., and Boston, P., 2008a, Epigene and hypogene gypsum karst manifestations of the Castile Formation: Eddy County, New Mexico and Culberson County, Texas, USA: International Journal of Speleology IJS, v. 37, p. 83–98.

Stafford K.W., Rosales-Lagarde L. and Boston P.J., 2008b, Castile evaporite karst potential map of the Gypsum Plain, Eddy County, New Mexico and Culberson County, Texas: a GIS methodological comparison. J. Cave and Karst Studies. p. 83-98.

Stafford, K.W., Klimchouk, A.B., Land, L., and Gary, M.O., 2009, The Pecos River hypogene speleogenetic province: a basin-scale karst paradigm for eastern New Mexico and west Texas, USA, In Stafford, K.W., Land, L., and Veni, G. (eds), NCKRI Symposium 1: Advances in Hypogene Karst Studies. National Cave and Karst Research Institute, Carlsbad, New Mexico, p. 121-135.

Stafford, K.W., Ulmer-Scholle, D., and Rosales-Lagarde, L., 2008c, Hypogene calcitization: Evaporite diagenesis in the western Delaware Basin: Carbonates Evaporites Carbonates and Evaporites, v. 23, p. 89–10.

APPENDIX B

DETAILED METHODOLOGY

KARST SURVEY

Understanding the spatial distribution and density of karst features is of utmost importance when trying to recognize the hydrogeological controls and framework of an area. Spatial analysis of solutional subsurface conduits will be done through the process of physical cave mapping, overland surface mapping, creation and illustration of cave maps, and the use of spatial data (LiDAR) through the use of GIS.

Cave mapping involved the use of a two to three person team mapping of all humanly enterable caves within a 100 meter buffer on either side of RM 652 in Culberson County, Texas. Surveys were conducted through the use of a Disto rangefinder, Suunto compass / clinometer, then recorded and sketched in the field following the National Speleological Society protocol (Dasher, 2011). By mapping, these caves, general trends, structural controls, and preferential flow paths can be identified to assess the potential for large-scale dissolution and potential roadway failure. Caves that were found and surveyed were described in terms of morphology and speleogenetic evolution. All cave surveys were drafted through the use of the programs Walls and Xara Xtreme 5. Walls is a free program hosted by the Texas Speleological Survey and is specifically designed for the processing and analysis of cave surveys. Xara Xtreme 5 is simply a graphics software where exported line plots from Walls can be further refined into cave maps. In conjunction, these programs will allow for a digital view of potentially hazardous karstic features within the study area.

The initial steps of cave mapping begin by essentially creating a line plot that contains a point to point survey of length, declination, and inclination. The ultimate output of these measurements is a top down plan view and a side profile view of elevation changes within the cave. Starting at the cave entrance, a point is chosen that will be the beginning of the cave survey. From this point (A), a second point (B) is scouted by the third member of the cave mapping team and the measurements of length, declination, and inclination are measured by the second team member. These readings are recorded by the cave sketcher or first team member and subsequently plotted within a field notebook. This plot or sketch essentially acts as the skeleton of the cave. Field sketches are prepared while the point to point survey of the cave skeleton is being made. Once the "skeleton plot" is made, geomorphic details such as cave wall and floor rock type, the presence of risers, cupolas, scallops, fractures, floor and ceiling drops are filled in (Fig. B1).

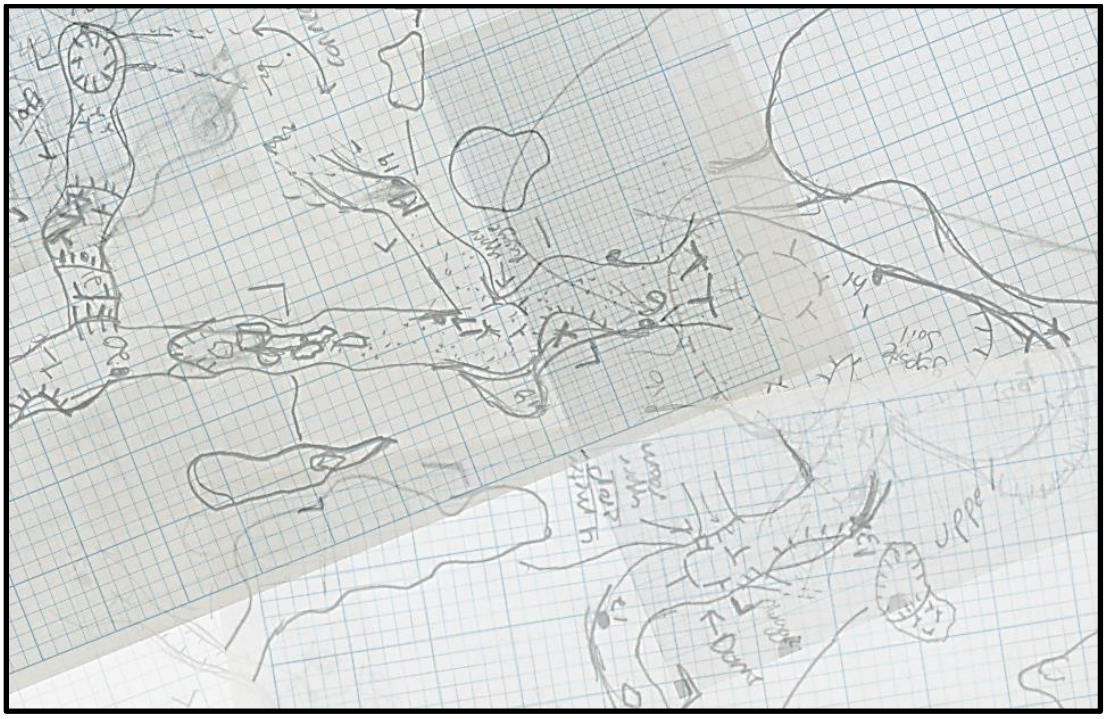

Figure B1: Raw plan view of a field sketch of a central chamber in Lillcher Cave.

In addition to the sketch shown above, a cross-sectional profile view is also created to show the vertical relationship of passages within the subsurface; both the plan and profile views are eventually digitized and refined into final cave maps. In addition to sketching as many details as possible, photos and videos of interesting features are taken with a GoPro wide angle lens to be used as a reference for the exact characteristics of certain areas within a cave.

After the entire cave has been sketched in detail with both plan and profiles views, the cave is ready to be digitized into its final form. To begin this process, all of the tabular data such as inclination, declination, and length are entered into the previously mentioned program “Walls”. From left to right, the data is entered into walls in the following format (Fig. B2):

| Point 1 | Point 2 | Distance (meters) | Inclination | Azimuth (degrees) |

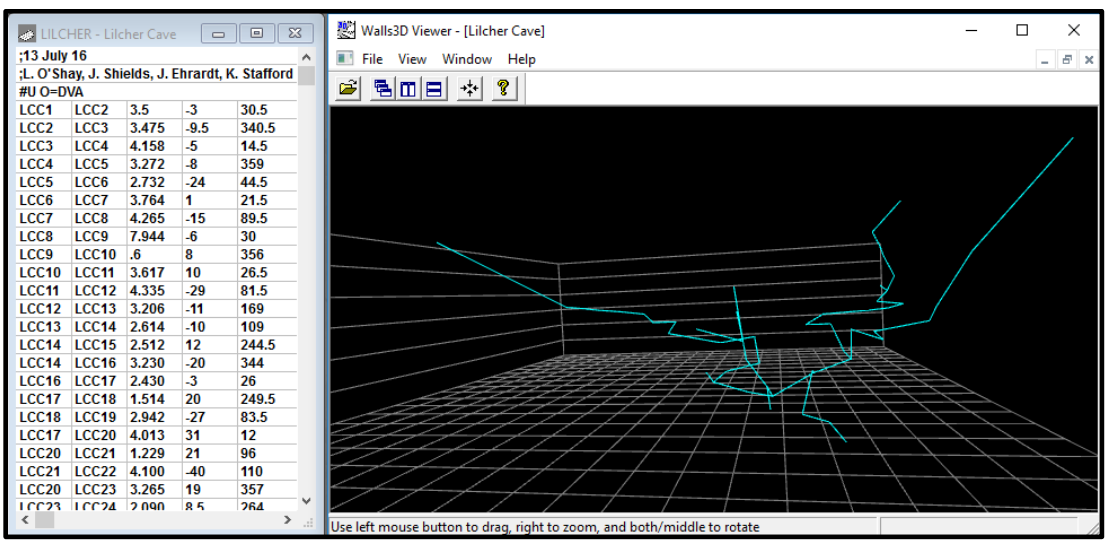

Figure B2: Walls cave software showing data input panel and output cave skeleton plot in 3D.

Using the provided data, Walls drafts a skeleton plot of the cave in both plan and profile views. This program accounts for inclination in order to correct line segment distances that are

shot at large angles, which are sometimes difficult to sketch in the field accurately. Ultimately, an accurate skeleton map of the cave is made with the vertices of the inputted data. This corrected skeleton of the cave is used as the foundation in which the detailed version of the final cave map will be made. With the skeleton created, it is then copied into an illustration program in order to be digitized with details. During this process, the scale is preserved so that both the profile and plan views are equivalent in size. In this case, the program Xara Xtreme 5 was used to digitize the details around the skeleton plot. To add detail to the skeleton plot that is output by Walls, the field cave sketches are draped over the plot and drawn to scale preserving cave passage length, width, and height. By transparently displaying the field sketch over the skeleton plot, the previously mentioned geomorphic cave features, floor drops, ceiling breakdown, water filled passages, and more can be digitized in with accuracy (Fig. B3).

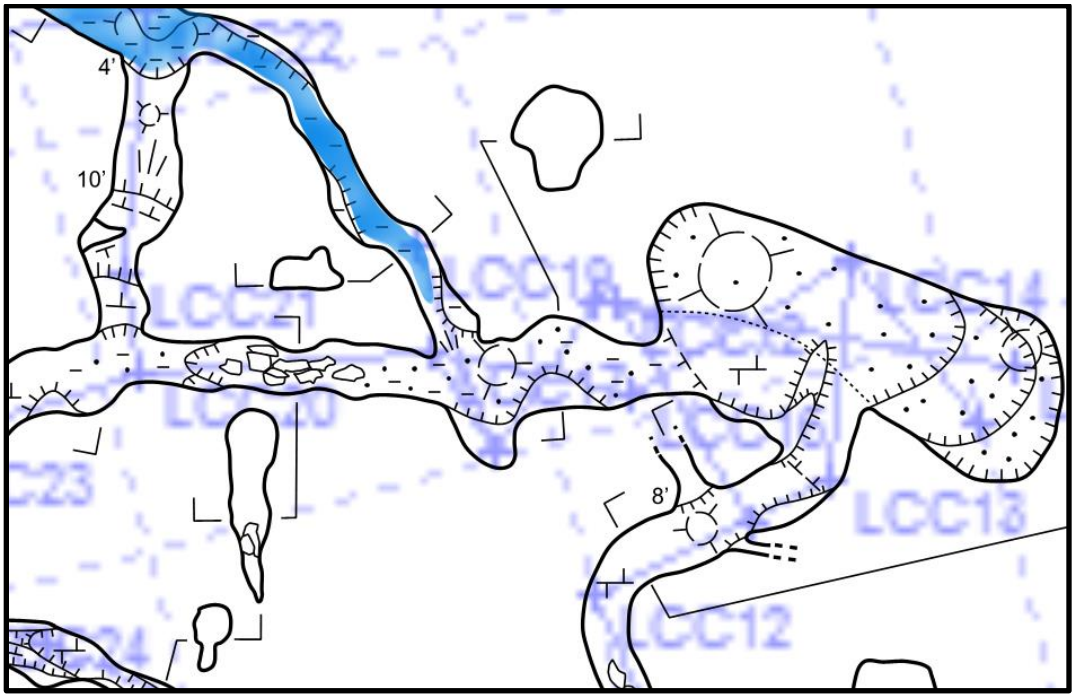

Figure B3: Walls skeleton plot overlain with digitized drawing of field sketches in XaraXtreme5.

This final view of the cave is known as the “plan view” or a top-down look at the karstic feature as it lies in the subsurface. After the plan view is made, the profile or cross-sectional view of the cave is also digitized. This view displays the vertical relief and relationship of the cave as you move down the cave passage. Combined, the plan and profile views offer a look at the cave passage orientation and furthermore, can offer insight into the speleogenic evolution of the cave. All maps are completed with a title, date of survey, north arrow, scale bar, passage length & depth, mapping personnel, and occasionally an index map of the caves location (Fig. B4).

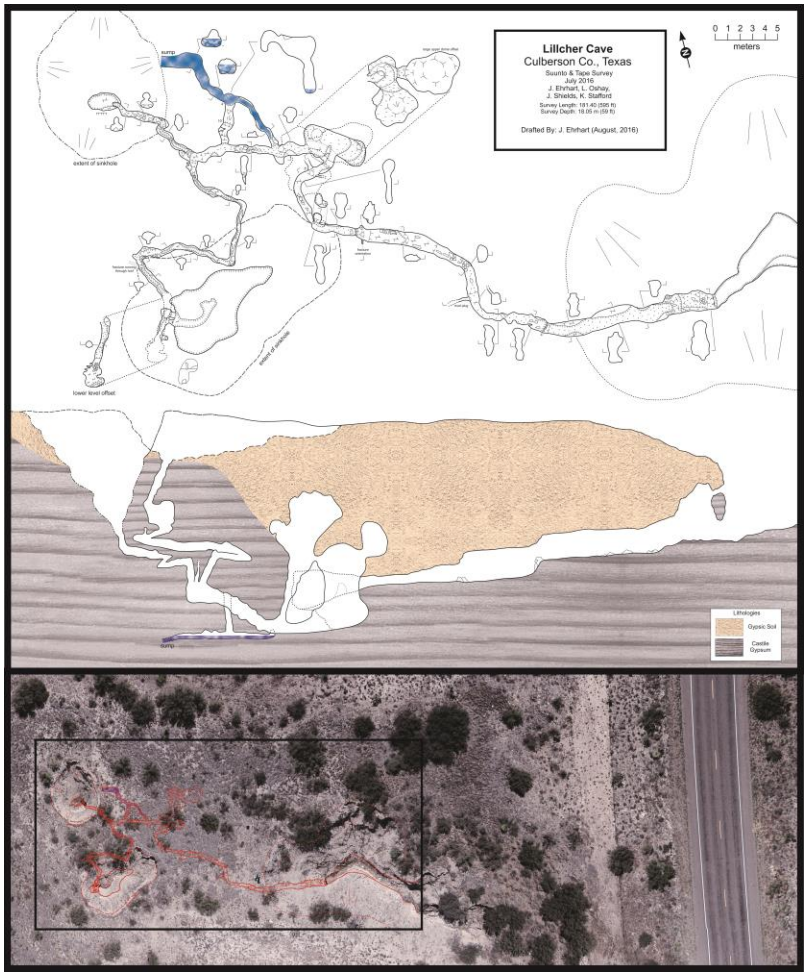

Figure B4: Displaying final cave map output of Lillcher Cave.

The overland survey portion of delineation involves systematically traversing the entire area on either side of RM 652 and identifying sinkholes, caves, solutional conduits, and karstic lineaments. All major overland karstic features are digitized through the use of ArcGIS and supplemented with LiDAR data. As seen in figure B5 below, the blue polylines represent the traverse tracks of five people on either side of RM652 with approximately 10-meter spacing; each karstic feature was logged spatially in a GPS unit and described in the field. Monitoring traverse tracks helps to verify karstic feature locations and ensure proper coverage. Collectively the area traversed covers a total of 19.2 km^2.

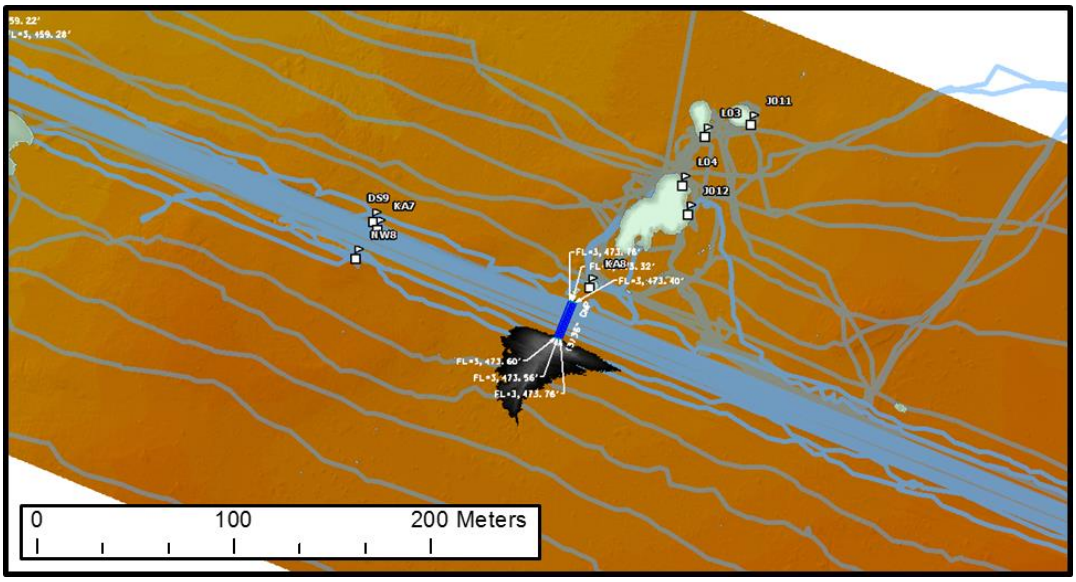

Figure B5: Image of DEM overlain with traverse tracks in blue and karstic features in white.

GIS LiDAR and DEM

As previously mentioned, accompanying physical cave mapping and karst delineation with LiDAR data can help to enhance the accuracy and clarity of a karst density study. The LiDAR data used for this study was shot in February of 2016 by the Texas Department of Transportation. The Texas Department of Transportation provided Stephen F. Austin State University with a total of 440 LAS point cloud files which cover 100 meters on either side of RM652 for 55 kilometers totaling to approximately 20 km^2 (Fig. B6).

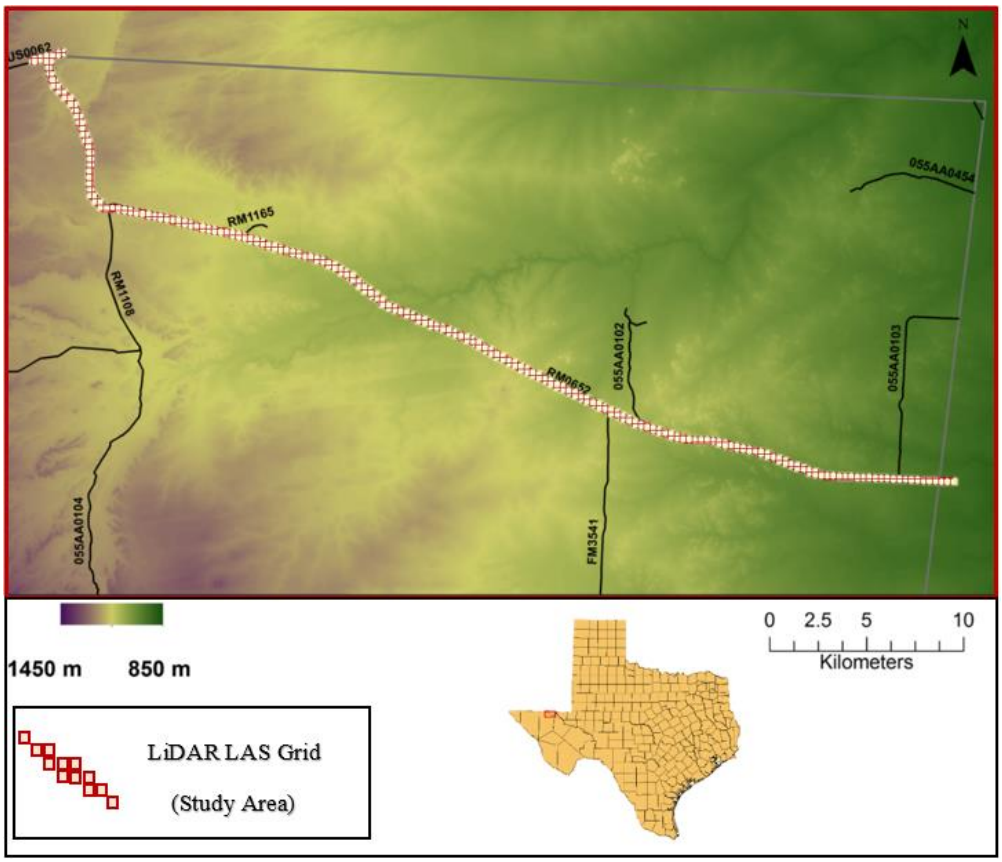

Figure B6: Index map of study area showing LAS grid along RM652 in Culberson County.

This raw data was imported into ESRI ArcGIS for desktop in order to begin digitization and karst delineation. The high density and accuracy of these point cloud files provide as the basis for a digital elevation model (DEM) that can be further analyzed to detect karstic features. The first step required in the creation of a DEM is extracting data from the LiDAR point cloud LAS file. To do this, a LAS dataset can be made to easily view the entirety of the data in a manageable way. The LAS Grid is imported as seen in figure B6, and converted into a digital elevation model (DEM) using the tool *LAS Dataset to Raster*. Before using the *"LAS Dataset to Raster* tool there is some prep work that must be done to the dataset. For example, when this LiDAR data was shot in February of 2016, it was shot using a TxDOT Surface Adjustment Factor of 1.00025. This adjustment factor must be applied to the projection system in order for the LiDAR LAS grids to line up correctly to their real world positions. To accomplish this, a custom projection system built off the original State Plane system was made which accounted for this Surface Adjustment Factor (SAF); this was done by multiplying the SAF by the false easting and northing of the original Projected Coordinate System (PCS). Additionally, it is important to understand that by default LAS Datasets show all of the point cloud data that was shot. Meaning all returns will be displayed over the given area (i.e. ground, upper and lower vegetation, unassigned points etc). For the purpose of locating depressions and karstic features the desired raster, as previously mentioned, is a DEM or digital elevation model. This digital elevation model displays only the ground points and hides all other point cloud data in order to get the true surface topography. To create this raw DEM, within the LAS Dataset a few options must be specified using the "LAS Dataset Toolbar" (Fig. B7).

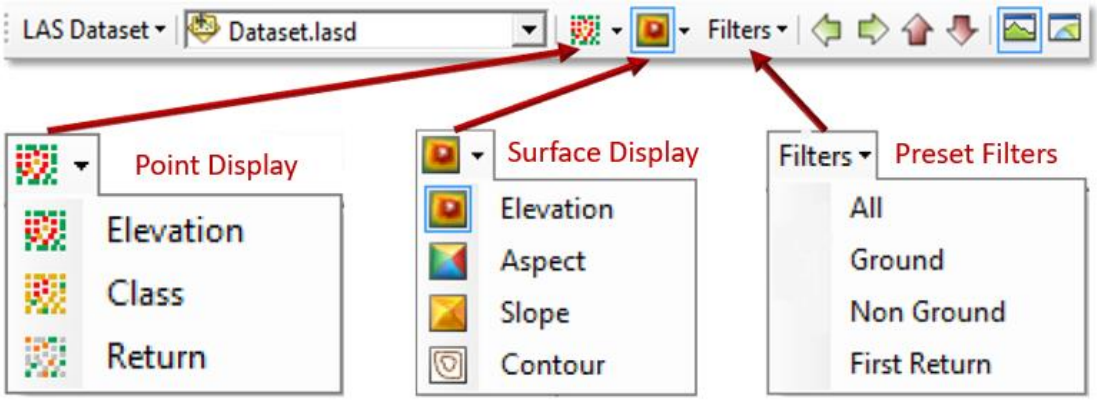

Figure B7: Las Dataset Toolbar options as seen in ArcMap for Desktop V. 10.3.1.

The first dropdown within figure B6 labeled as "LAS Dataset" allows for the alteration of the point count budget when creating cross-sectional views of the LiDAR data. The point count budget is essentially the limiting factor on how many points of data can be displayed on a single cross section. To better display cross-sectional data, the point count budget was set to 150,000 from the default of 50,000 (more on this later). The dropdown labeled "Point Display" displays the point cloud data in three ways, by its elevation, class, or return (Fig. B7). Modeling the data in the "Point Display" view also allows the user to see the LiDAR point density across a given area (Fig. B8).

Under the "Point Density" dropdown "Class" and "Return" can also be selected. The "Class" option will display the LiDAR point cloud data as classes (Unassigned, Ground, Noise, Rail, etc.) and color them accordingly. The "Return" option will display the same point data but divide them up based on which return they are associated with (Last, First, All, etc.). Similarly, the next dropdown within the LAS Dataset toolbar labeled "Surface Display" (Fig. B7) interpolates and creates a surface on the fly from the supplied LiDAR point cloud data that is seen

in Figure B8. The “Surface Display” dropdown has three main selections: elevation, aspect, and slope. The elevation selection creates a real world topographic display of the elevation data. The aspect selection displays the downslope direction for the maximum rate of change. Lastly, the

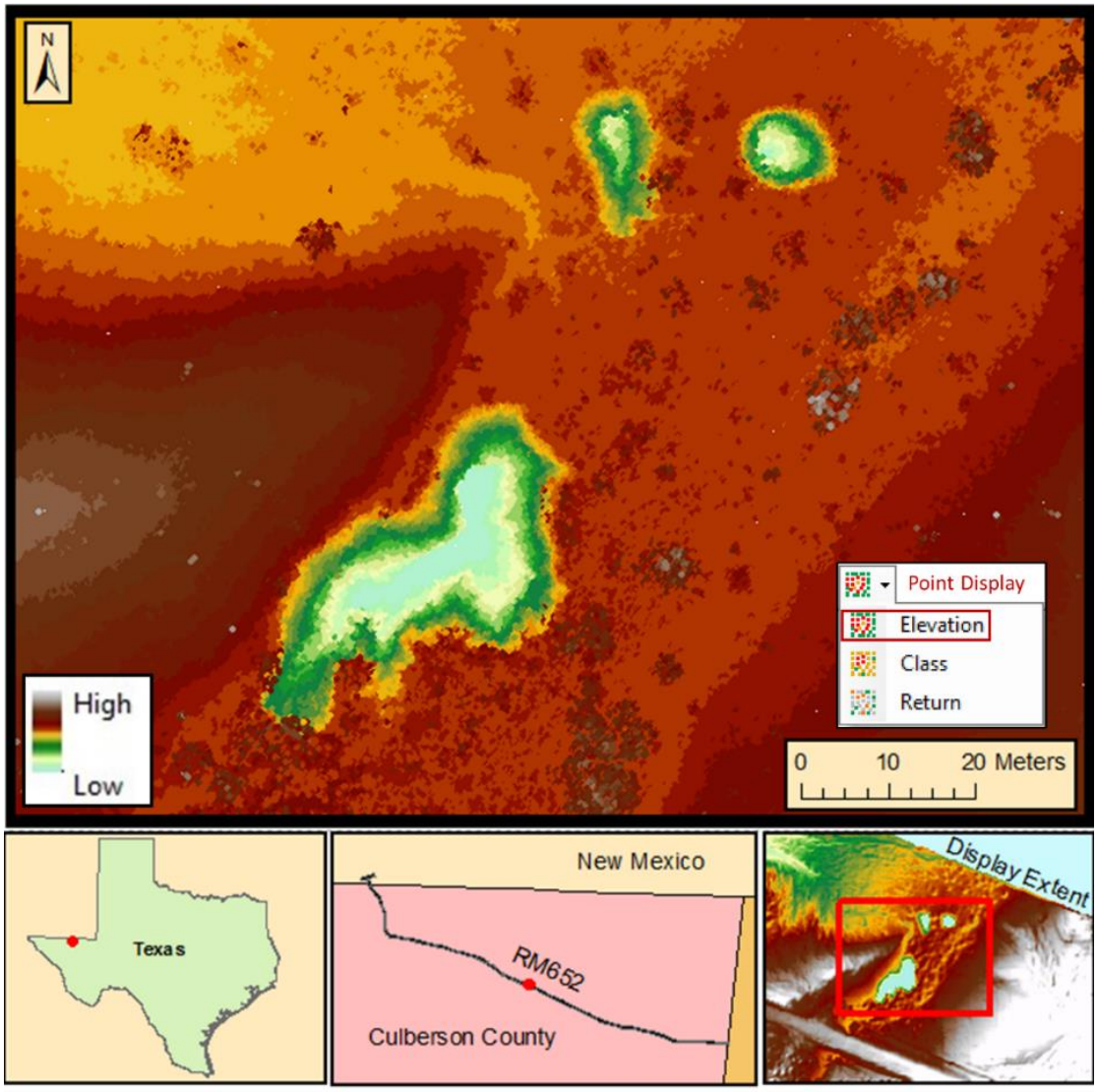

Figure B8: Sample section of the study area showing the “Point Display” - elevation view and point density (Note: This is only displaying 25% of point cloud data in the current extent and is filtered to “all returns”).

slope selection displays the steepest portion of each cell and is recorded in degrees. As seen in figure B9 below, using the "Surface Display" with elevation selected allows for a more three-dimensional view of the same study area segment when compared to the "Point display" (Fig. B8).

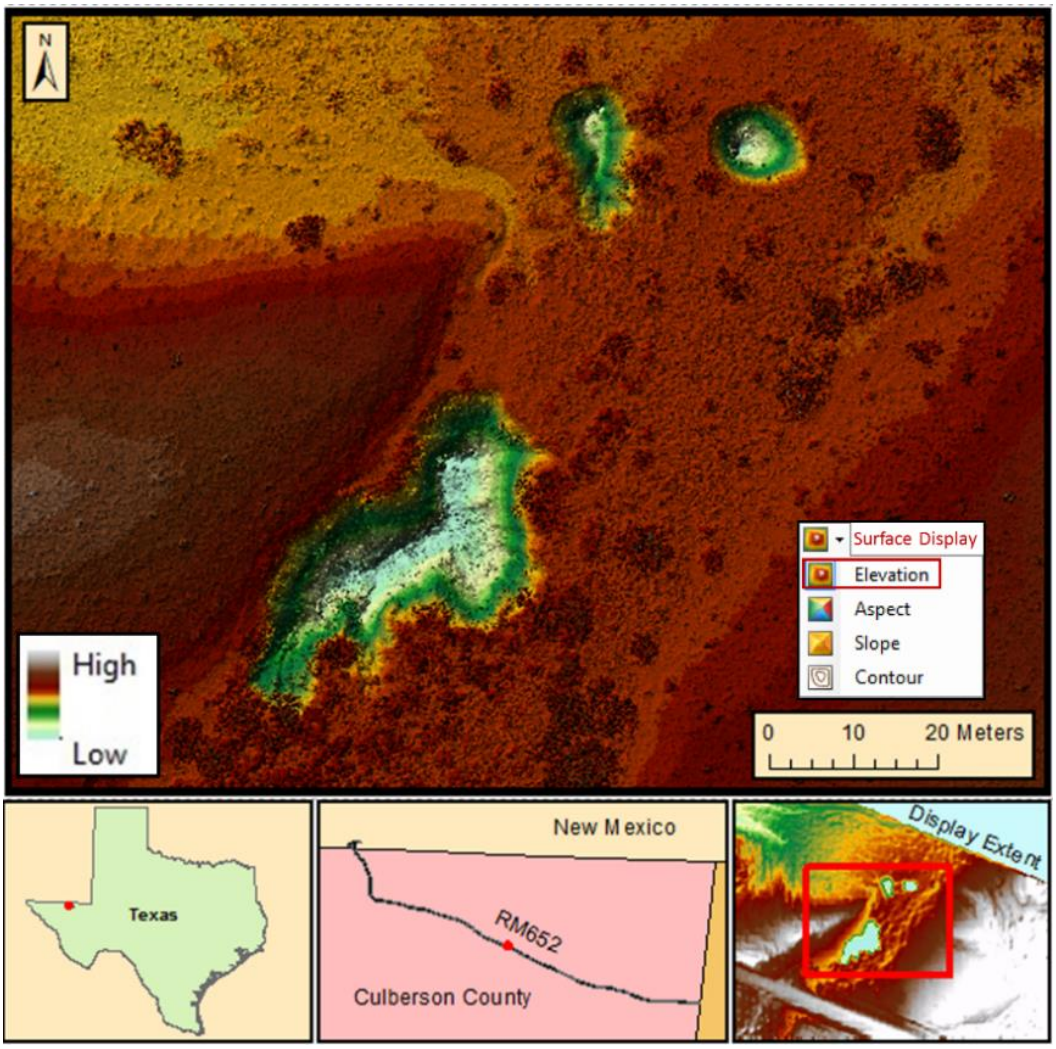

Figure B9: Sample section of the study area showing the "Surface Display" - elevation view and topography (Note: This is only displaying 25% of point cloud data in the current extent and is filtered to "all returns").

As previously mentioned, slope and aspect maps were also created using the "Surface Display" option. These maps allow for both a two and three-dimensional look at areas where the slope is the highest (Fig. B10). Ultimately, slope analysis was performed to locate high-angle slopes as many of the larger collapse features within the study areas are expressed as very steep gradients, especially near cave entrances.

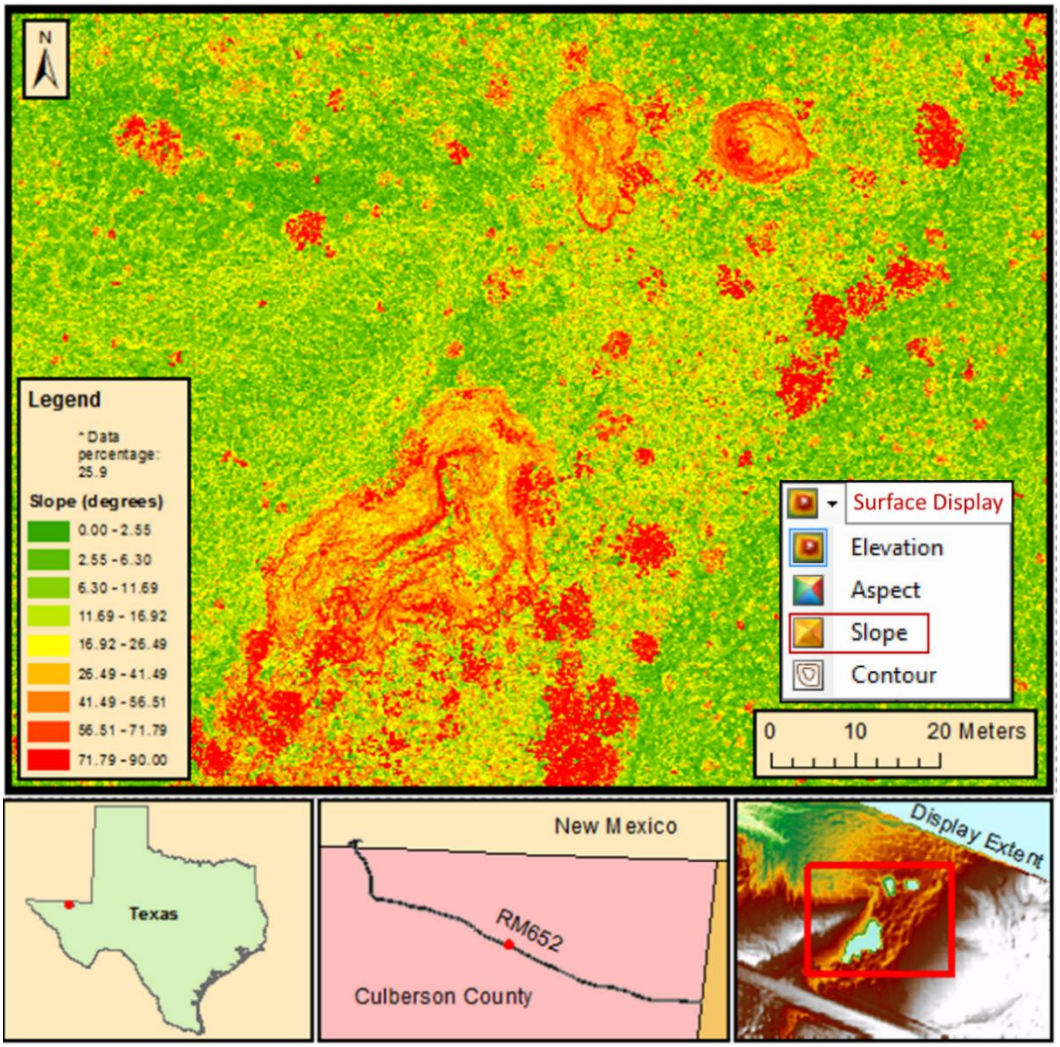

Figure B10: Sample section of the study area showing the "Surface Display" slope view with topography inclination in degrees (Note: This is only displaying 25% of point cloud data in the current extent and is filtered to "all returns").

Lastly, the final dropdown within the LAS Dataset toolbar is the “Preset Filter” dropdown (Fig. B7). The filter option allows the user to filter out unwanted data in a quick and simple way. For example, selecting the “Ground (bare earth)” option will filter out every return other than those labeled as ground or bare earth. Likewise, the “First Return” option will filter out all data that is not labeled as first return. The filter selection does have an effect on the final map display of the previously mentioned dropdowns. For example, the “Surface Display” elevation option will create an interpolated elevation surface of either the ground, first return, or all returns, depending on which preset filter is selected. It is important to note that all of the aforementioned selections play a role in the creation of the raw DEM through the use of the *LAS Dataset to Raster* tool. With the 3D Analyst extension, ground (bare earth) preset filter, and triangulation method selected, the *LAS Dataset to Raster* tool was used to create the raw DEM for the entire 55 Kilometer study area (Fig. B11). Using triangulation instead of a binning method offers true interpolation, and is best for DEMs. With triangulation, cell values are calculated from a triangulated model of the LAS Dataset.

The sampling size is determined by the resolution of the LAS data. In this case, the LAS data has a resolution of 0.5 meters. The Natural Neighbor interpolation method was used because it is known to produce the better results in terms of accuracy and display than linear or binning methods (Esri, 2012). The DEM created as a result of this tool provides a high resolution (0.5 x 0.5 meter) model of the topography with all other returns removed; meaning this DEM will show only the bare earth and remove all vegetation making the delineation of sinkhole features, areas of subsidence, river channels, and other hydrological features much easier (Fig. B12) (Liu, 2008).

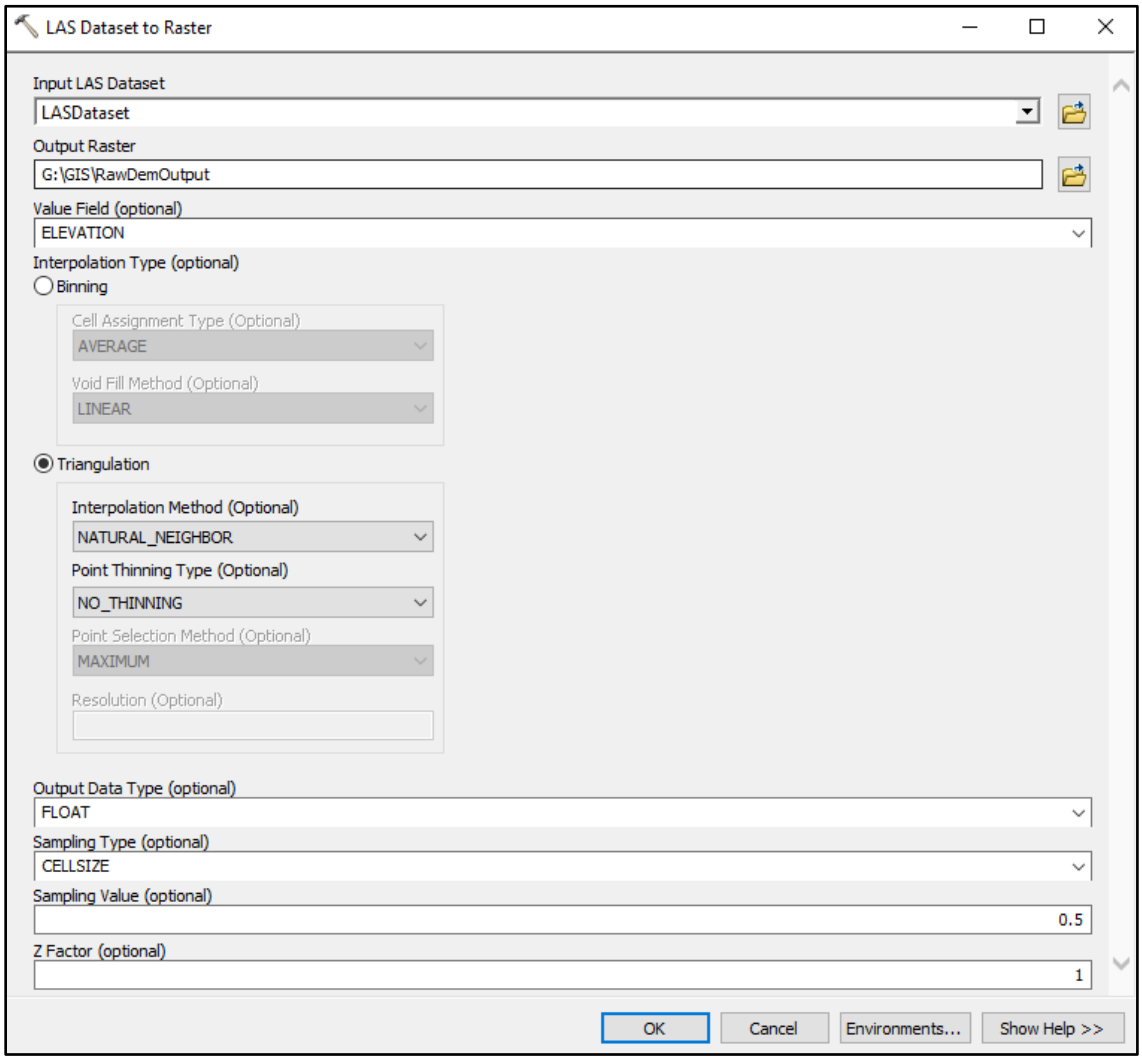

Figure B11: Parameters used for the creation of the DEM Raster where Value Field = Elevation → Triangulation = Natural Neighbor → Thinning Type = No Thinning, → Output Data Type = Float → Sampling Type = Cell Size → Sampling Value = 0.5.

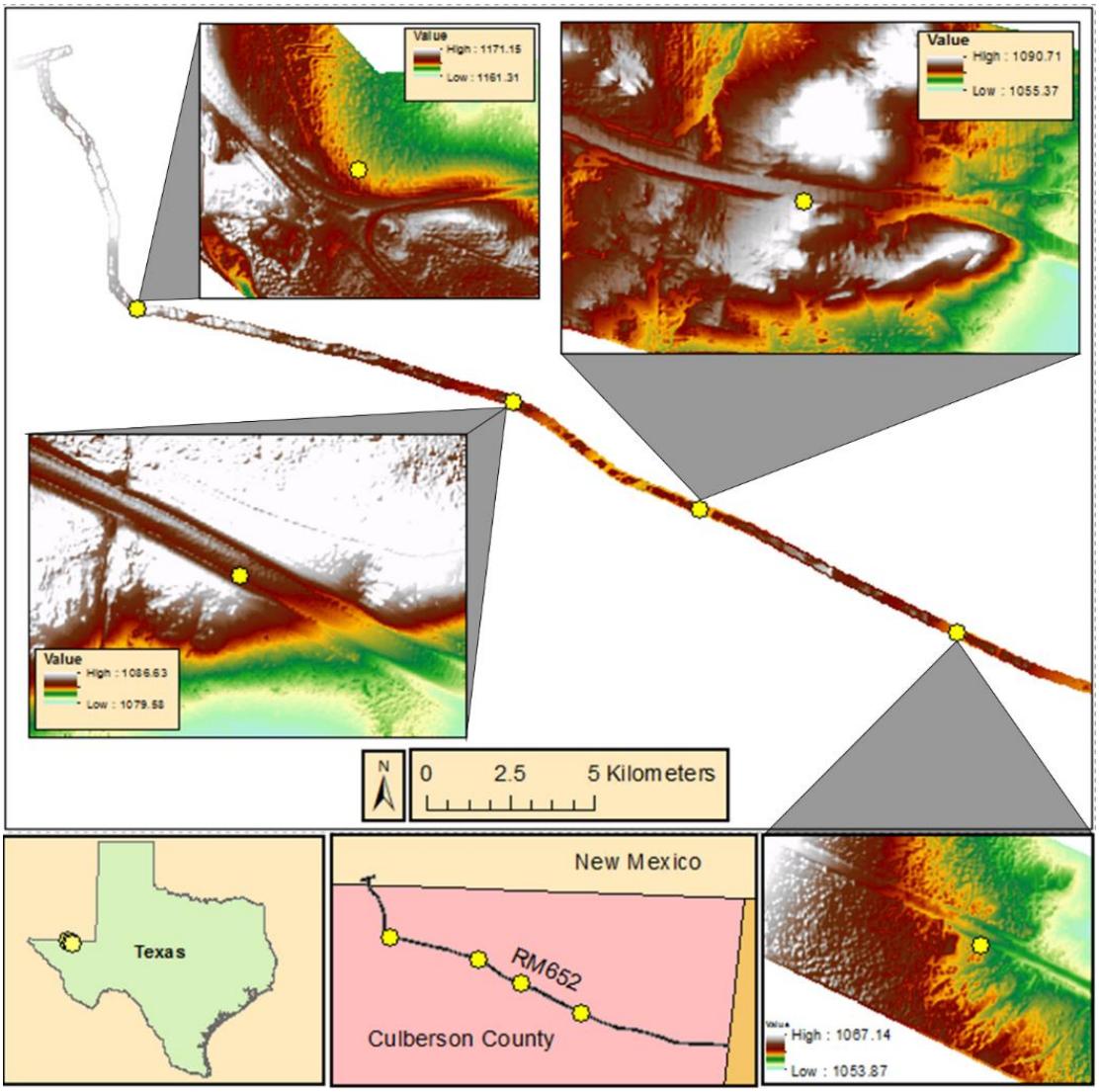

Figure B12: Sample of the output of the "LAS Dataset to Raster" tool. Displays segments of the DEM that were created for the entire 55 kilometer study area.

As previously mentioned, DEMs with high resolution can be used to detect and delineate karstic features such as sinkholes, depressions, and cave entrances. The workflow in figure B13 displays the entire process of converting a raw digital elevation model into a karstic delineation shape file that contains all attributes associated with each hydrologic feature.

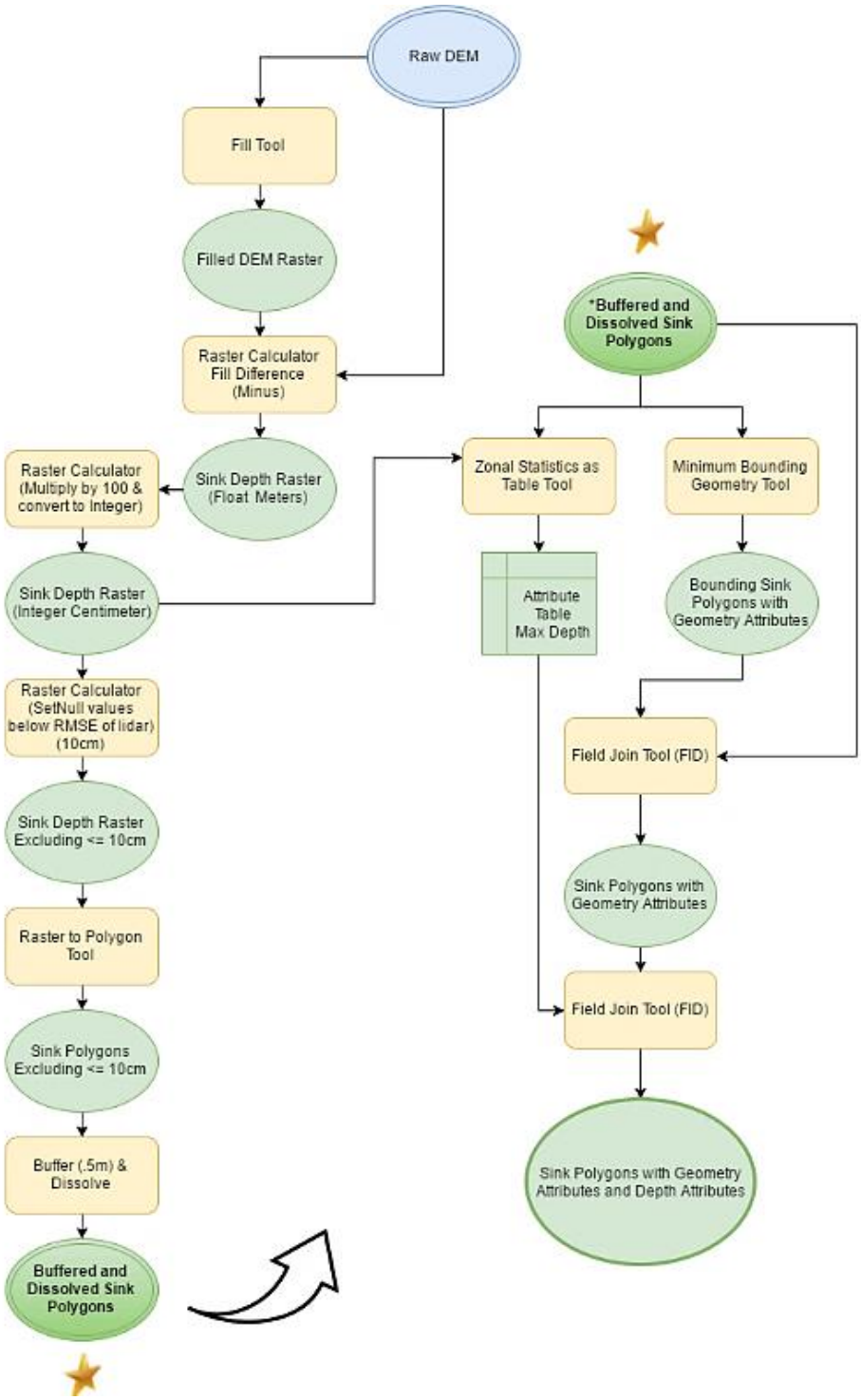

Figure B13: Model workflow for finding sinks and their associated attributes (depth, length, width, etc.).

In order to identify depressions, sinkholes, and caves the DEM must be run through the *Fill* tool. This tool will fill all of the depressions up to their spill level or pour points, (the minimum elevation along its watershed boundary) essentially creating a depressionless DEM (ArcGIS). This tool is located under Spatial Analyst Tools → Hydrology → Fill within ArcMap v. 10.3.1 (Doctor and Young, 2013). After the DEM is filled, the original DEM is subtracted from the filled DEM in order to generate a raster that represents just the depth of areas that are below the original surface; this process nets a 'fill-difference' raster (Fig. B15a). The fill process is iterative, meaning that if a filled area is located within a larger sink it will continue to fill all the way to its spill point. This works well for locating depressions and sinks but can cause areas that are near culverts or bridges to completely fill and dam up. This is because when creating a DEM using only the ground return, sometimes bridges are classified as ground which artificially raises the stream level up to the elevation of the bridge surface. This creates areas where water would actually drain out through the culvert or under a bridge but is artificially damming up and ponding (Fig. B14).

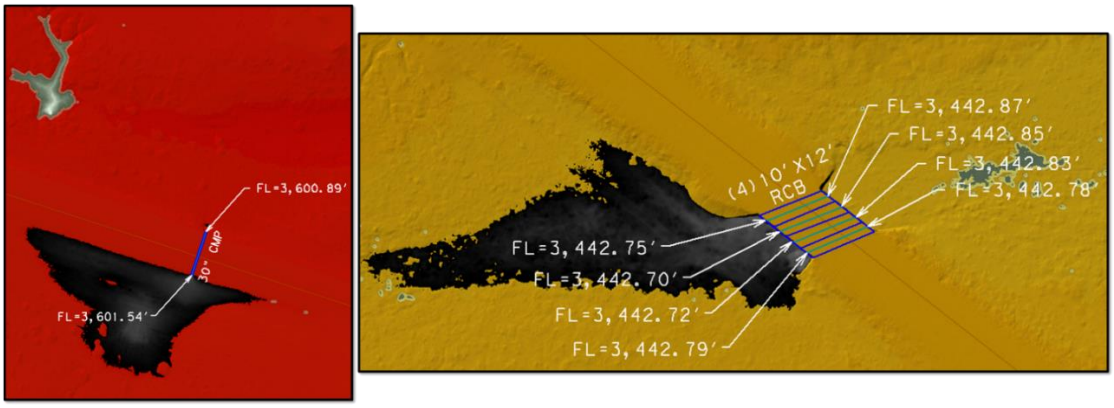

Figure B14: Areas within the DEM that are classified as artificial depressions (black) due to the damming of water at culverts (left) and bridges (right). The green outline in the left diagram denotes an actual hydrological sink with internal drainage.

Poppenga et al., (2010) suggested a workflow that uses a “least cost path analysis” as a method to remove these artificial dams in order to preserve potential real world depressions within these areas. Similarly, Doctor and Young (2013) suggested a workflow that requires manually digitized culverts to be ‘burned’ into the DEM in order to allow streams to drain across these areas. This would allow for true depressions within the filled area to be preserved. However, for the scale and scope of this research, these filled areas within 10 meters of culverts were simply removed and later field checked and re-digitized by hand if depressions did in fact exist.

Once the ‘fill-difference’ raster is created, as seen in figure B15A, some filtering must be done to remove unwanted data by providing a minimum depth threshold (Doctor and Young, 2013). All values of the ‘fill-difference’ raster that were less than the vertical accuracy of the of the LiDAR bare earth model were filtered out and removed. The LiDAR provided by TxDOT has a vertical accuracy of 0.10 m (10cm); all values less than or equal to the RMSE of the data were removed which resulted in a “cleaner” raster with less artifacts (Fig. B15B). To do this filtering, *Raster Calculator* was used with the command SetNull(“Raster”) < = 10, “Raster”) which essentially classifies all values less than or equal to 10cm to ‘null’ or ‘No Data’. The filtered depression raster cells were then converted from float to integer so they could be converted into polygons, without simplifying, so that no data was removed around the periphery of the depression (Fig. B15C). Polygons were then buffered to 0.5 meters, dissolved, and smoothed to incorporate immediately surrounding areas as a depression (Fig. B15D). Once the filtered and smoothed depression polygon was created, the attributes from the DEM can now be extracted and applied to shape file. This was accomplished through the use of the *Zonal Statistics as Table* tool.

This table contains information such as maximum sinkhole depth and area of each depression identified in the previous steps. The *Zonal Statistics as a Table* tool essentially assigns an FID number to each depression attribute row, which directly corresponds to the FID number that is already assigned to each of the depression polygons. This tool is only pulling data from the DEM in the area that is overlain by the depression polygons. Once the table was created, it was then permanently joined to the depression polygon shape file through the use of the *Field Join* tool. The depression polygon shape file now contains the max depth and area attributes (Fig. B15E). The geometry of each polygon was then calculated for each depression with the *Minimum Bounding Geometry* tool. With polygon geometry type set to *convex hull,* an idealized convex polygon was digitized around the depression polygon (Fig. B15F). These new minimum bounding geometry polygons contain geometrical attributes such as the length of the major and minor axis as well as the orientation of the major axis. Once again, by using the *Field Join* tool these new attributes can be combined to the depression polygon shape file that already contains our max depth and area attributes. Lastly, supplementary columns can be added to this polygon shape file to calculate things like area and eccentricity. The eccentricity of each depression can be calculated using the *Field Calculator* and dividing the depression width by the length resulting in a ratio that can be used to assist depression origin. As seen in figure B15G, the final output for sinkhole delineation and further analysis is a filtered and buffered depression extent shape file with geometric and depth attributes applied to each feature. The result is a polygon shape file that is a representation of the possible sinks within the study area.

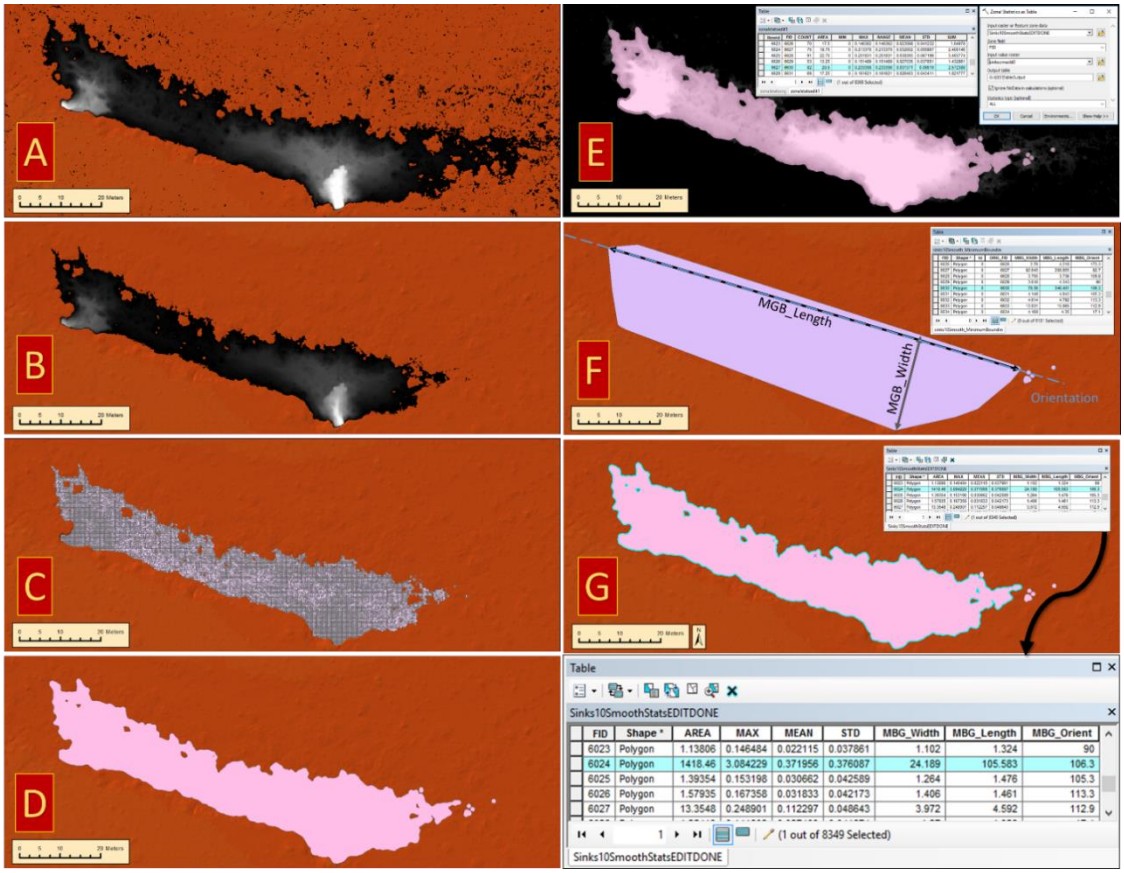

FID	Shape *	AREA	MAX	MEAN	STD	MBG_Width	MBG_Length	MBG_Orient
6023	Polygon	1.13806	0.146484	0.022115	0.037861	1.102	1.324	90
6024	Polygon	1418.46	3.084229	0.371956	0.376087	24.189	105.583	106.3
6025	Polygon	1.39354	0.153198	0.030662	0.042589	1.264	1.476	105.3
6026	Polygon	1.57935	0.167358	0.031833	0.042173	1.406	1.461	113.3
6027	Polygon	13.3548	0.248901	0.112297	0.048643	3.972	4.592	112.9

Figure B15: A) Fill difference DEM displaying depressions & their depths. B) Fill difference DEM converted to an integer displaying depressions and their depths (excluding values below the RMSE of the dataset, 10cm). C) Polygons of depression derived from the 'Raster to Polygon' tool. D) Polygon of depression buffered to .5 meters, dissolved, and smoothed for aesthetics. E) Polygon of depression overlying the original depression depth DEM and statistics for the polygon calculated into a table with the 'Zonal Statistics as Table' tool. This table displays the maximum/mean depth and area of the depression. F) Polygon of the maximum geometry of the original polygon that contains attributes such as, the length of the major and minor axis, and orientation of the major axis. V) Represents a culmination of all the previous steps; Displays the buffered and dissolved depression polygon, with the attributes from step (F) and (E), joined by the use of the 'Field Join' tool.

The previous depression identification process not only identifies sinkholes but any and all depressions located within the DEM. As previously noted, the depressions that are far too small, below the vertical accuracy of the LiDAR, or are simply artificial due to culverts/bridges

are removed to help combat this problem. However, depressions that are associated with roadways, river networks, and other man-made features such as stock and frac ponds will also be identified (Liu, 2008). Features like these that were not removed during the prep and filtering process and are known to be anthropogenic or non-karstic were removed manually; this resulted in a map that contains all karst features within the study as determined by LiDAR analyses (Fig. B16).

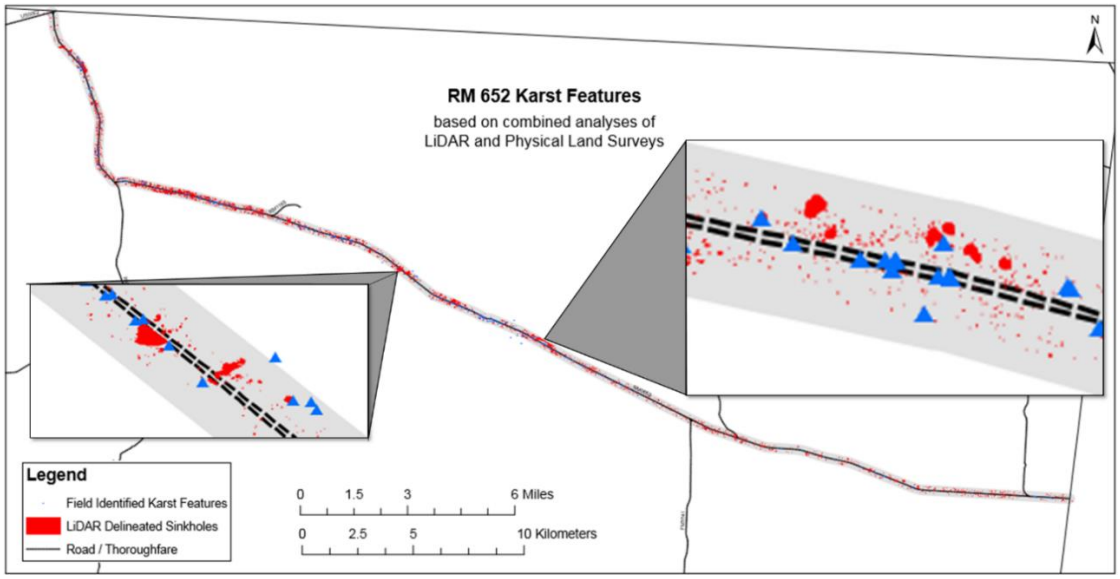

Figure B16: Filtered output shapefile of karstic features within the study area determined by LiDAR analyses and open conduits / cave identified through field survey (blue).

Creating a density map that is weighted on both sinkhole depth and area can be done to better understand the extent and frequency of karstic features within the study area. The first step to accomplishing this map is to use the *Polygon to Point* tool where the input is our filtered polygon depression shape file. Once these polygons become points they retain all of the previously assigned attributes. These attributes were then used as weighting values when computing two *Kernal Density* maps (Fig. B17a; B17b) The final Kernal Density Map made was

based on the combined analyses of physical land surveys and displayed in features per square kilometer (Figure B17c).

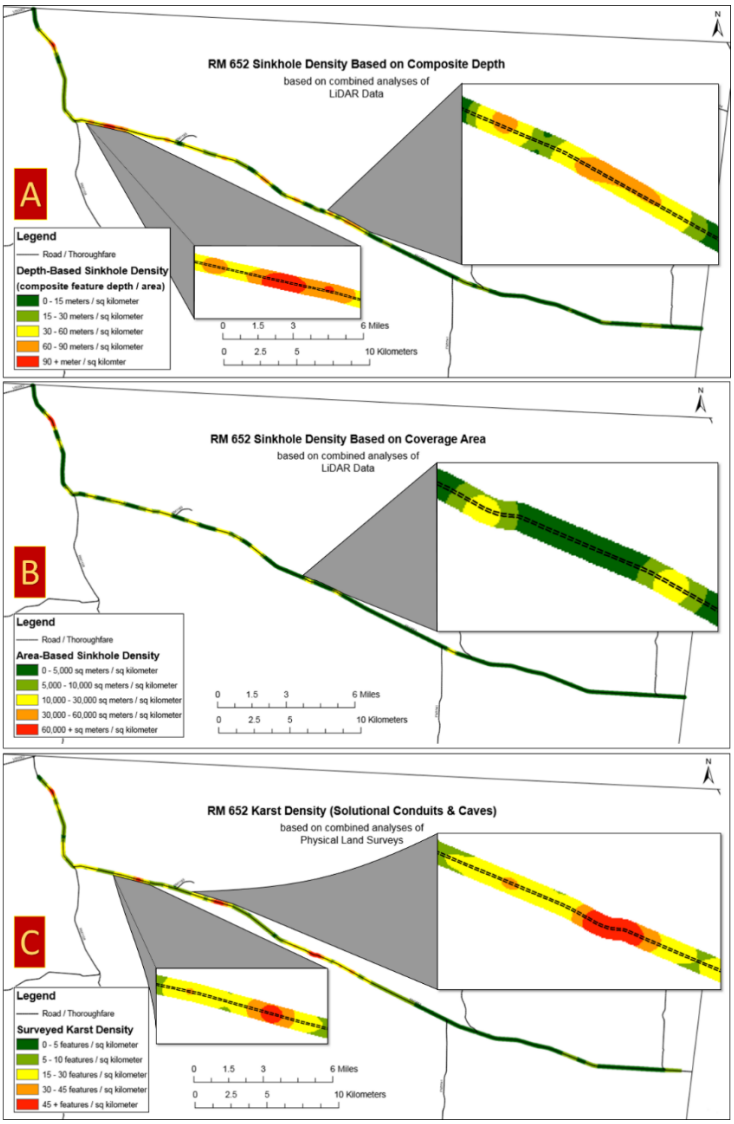

Figure B17: A) – raster map of the spatial density of sinkholes identified through LiDAR analyses that have been proportionally weighted by the maximum depth of individual sinkhole polygons delineated. Density is measured in units of meters per square kilometer. B) raster map of the spatial density of sinkholes identified through LiDAR analyses that have been proportionally weighted by the area of coverage of individual sinkhole polygons delineated. Density is measured in units of square meters per square kilometer. C) raster map of the spatial density of karst features identified through traverse-based surface surveys. Density is measured in units of individual features per square kilometer.

Depressions that were identified in the previous steps may or may not contain open conduits into the subsurface (caves). These areas that were previously identified by the DEM depression analysis were then re-investigated using the LiDAR point cloud 3D and cross sectional views located on the LAS Dataset toolbar. This view allows for the 3-dimensional visualization of the land surface, which displays if there is, in fact, an open conduit or cave. If the 3D view was interpreted to contain an open conduit, these areas were then flagged to be checked and mapped during field work. For example, by re-examining the Lillcher Cave complex, the entry passages can be seen in much higher resolution than what is seen purely on the DEM (Fig. B18).

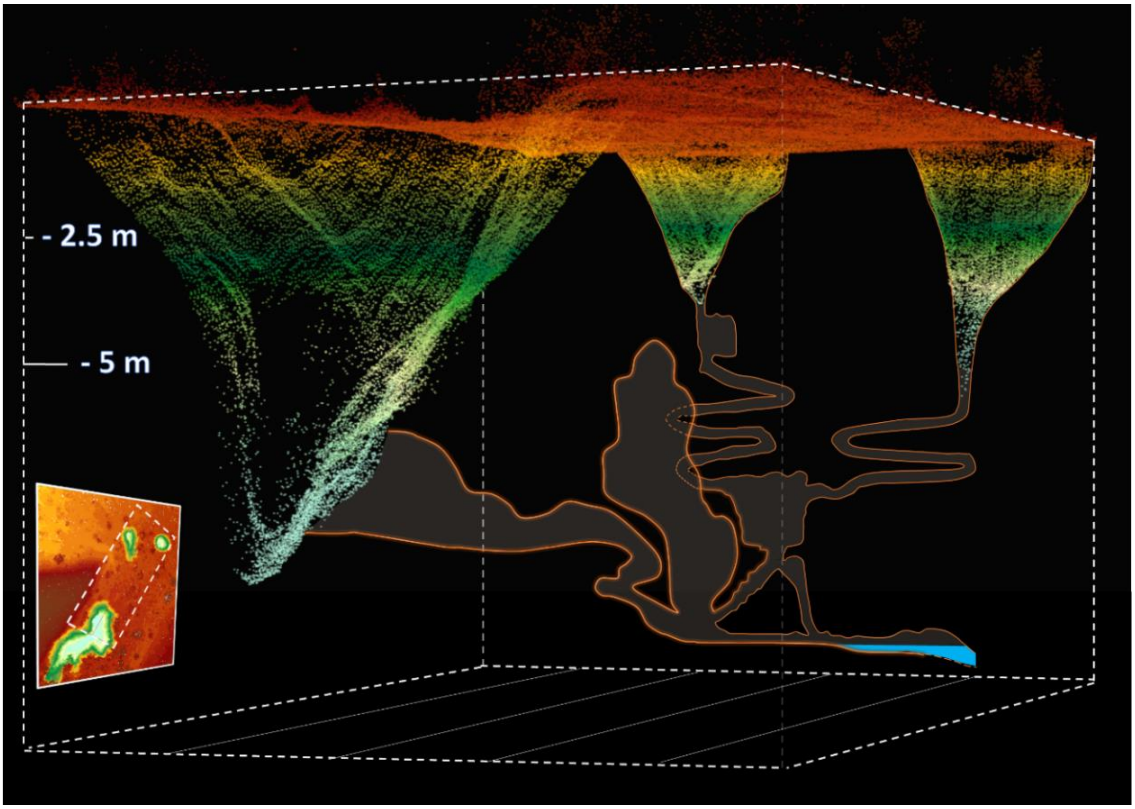

Figure B18: 3D view of LiDAR point cloud data of the entrances into Lillcher Cave with an illustration of a cave map from survey data (orange) shown with 2X vertical exaggeration.

REFERENCES

Dasher, G.R., 2011, On Station: A Complete Handbook for Surveying and Mapping Caves, National Speleological Society, p. 264.

Doctor, D.H.; Young, J.A. 2013, An Evaluation of Automated GIS Tools for Delineating Karst Sinkholes and Closed Depressions from 1-Meter LIDAR-Derived Digital Elevation Data. Proceedings of the 13th Multidisciplinary Conference on Sinkholes and the Engineering and Environmental Impacts of Karst, Carlsbad, NM, USA, 1 May–15 August 2013; p. 449–458

Liu, X., 2008, Airborne LiDAR for DEM Generation: Some Critical Issues, Progress in Physical Geography, Vol. 32, No. 1, p. 1-49

Poppenga SK, Worstell BB, Stoker JM, Greenlee SK. 2010. Using selective drainage methods to extract continuous surface flow from 1-meter lidar-derived digital elevation data. U.S. Geological Survey Scientific Investigations Report 2010–5059, p. 12.

APPENDIX C

CAVE AND KARST INVENTORY

CAVE MAPS, DESCRIPTIONS AND LIDAR RESULTS

CAVE DESCRIPTIONS

Caves were surveyed and drafted using standard cave symbology in order to determine their speleogenetic history and formation conditions. The caves within the study area represent both multi-stage epigenetic and multi-stage hypogenic processes with epigenetic overprinting.

<u>Lillcher Cave</u> (Fig. C1)

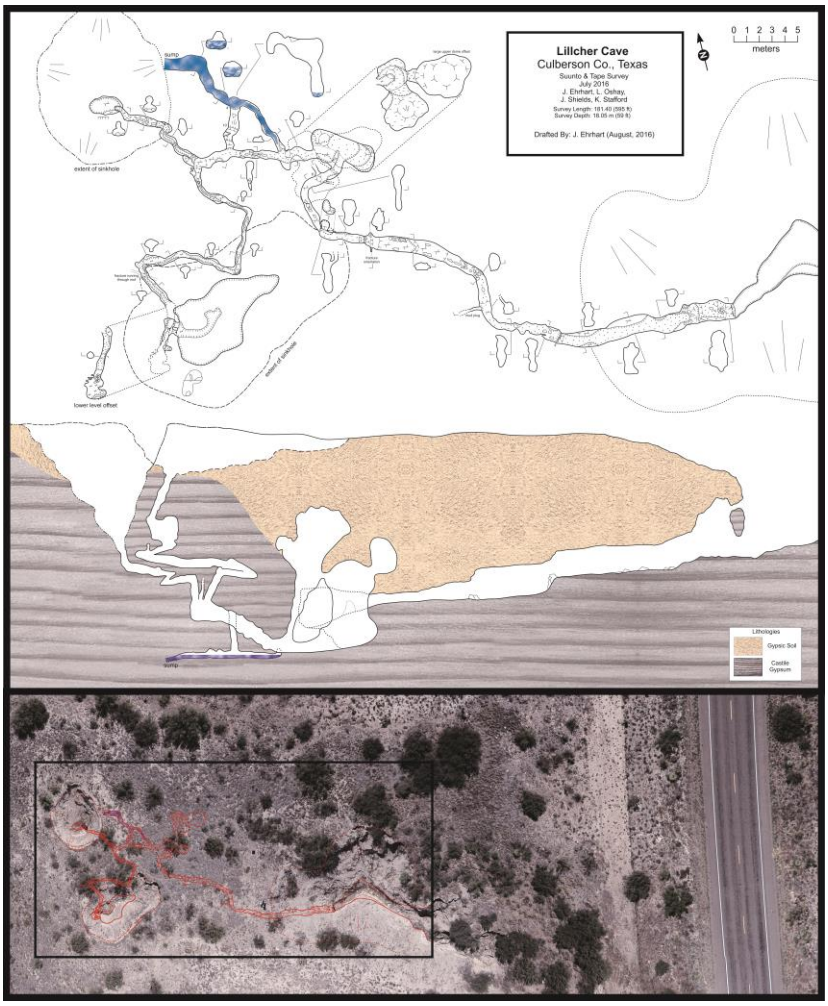

Figure C1: drafted cave map of Lillcher Cave.

Lillcher Cave is one of the largest caves proximal to RM 652 within the study area, with a surveyed length of 181 meters and depth of 18 meters below the land surface. The cave is expressed surficially by three entrances that are fed by a large 350 meter by 160-meter drainage basin. Passage height ranges half a meter in two of the entrances to eight meters within an upward stoping domal room. Passage width is relatively uniform ranging from 1.5 meters at the entrances to 3.5 meters within the dome room. Lillcher Cave is developed within the Castile Formation and the more recent Quaternary alluvium deposits. The first of the three entrances is located at the base of a large 49-meter-long by 27-meter-wide sinkhole, approximately 8.2 meters below the land surface. This main entrance is 1.5 meters tall by one meter wide. The two secondary suffusion induced collapse entrances are located within large circular sinkholes that are approximately 15 meters in diameter and 5 to 7.5 meters deep. These collapse entrances are primarily composed of gypsic soils at their widest point and transition to gypsum bedrock as they taper down into traditional cave passages.

From the primary entrance, the cave forms a mild slope with multiple floor and ceiling drops for 50 meters. The passage initially tapers down from 2.5 meters tall to a low crawl that is half a meter tall; it then tapers out again to three meters at the entrance to the major dome room. In cross section, the entry passage maintains an elliptical shape near the ceiling and tapers downward to an entrenched floor. Up until the dome room, the cave floor and walls are made of gypsum bedrock, with a thin layering of siliciclastic detritus on the floor. Along this first passage, there are a few highly elliptical blind passages and small domes which branch out from the ceiling. At the opening of the dome room, there is a large, inaccessible, one-meter diameter cave passage 2.5 meters above floor level that wraps around and connects back to the upper domes.

Within the main chamber, the majority of the domal structures and ceiling is composed of partially lithified sediment (indurated alluvial soil). The contact between the gypsum bedrock and overlying, presumably infilled, sediment is clear. Continuing north, the main chamber ceiling drops down to a one-meter-tall passage and subsequently splits. The lower passage slopes downward until leveling out as a water and mud-lined bedrock tube trending northeast. The upper passage's ceiling and floor undulate as it slopes upward and intersects an east trending passage that drops abruptly in the form of a pit, ultimately connecting to the lower passage. This lower passage continues northeast gradually filling with more and more water / sediment until reaching the sump. Continuing north along the upper passage, the ceiling begins to rise until reaching another room that is intersected at the ceiling by two passages. These passages are 3.5 meters off of the floor, average 0.5 meters in diameter, and lead to the two alternate sinkhole entrances.

This cave represents a complex morphology that is explained by multi-stage epigenetic processes. The inception or first stage of Lillcher Cave development began with the preferential dissolution of gypsum along fractures within the phreatic zone. The previously mentioned entrances and inlet tubes are morphologically comparable with phreatic tubes; having formed initially as elliptical tubes that were later entrenched and overprinted by vadose processes. Over time, fractures have solutionally widened during periods of an elevated water table, and entrenched during times, much like the present, where the water table has decreased in elevation. Initially, water percolated down through the overlying sediments and into fractures, dissolved ions into solution, and transported these ions out through the lower developing sump passage. One possibility for the formation of the currently half sediment filled domal chamber is that it originally was a large cavernous domal structure within purely gypsum bedrock. This section of the cave is one of the lowest points and is fed by many vertical to sub-vertical inlet tubes. This

significant amount of water influx likely dissolved and solutionally carved out a large dome room within the bedrock.

The contact between the gypsum and sediment within the dome room runs clear through the middle of the room and up the ceiling. This amount of bedrock dissolution, and the presence of highly brecciated and fractured bedrock at this contact suggests that this main chamber had likely collapsed and its coarse fraction (breakdown) was subsequently dissolved and transported out. Sometime after the collapse event, the area was then susceptible to suffusion and water inflow directly from the overlying surface. This inflow carried in Quaternary detritus from the surrounding area and eventually filled the main domal chamber and surrounding entrances completely with sediment, likely as breakdown material restricted flow through the outlet drain. Once this sediment had partially lithified, the surrounding cave passages began to pipe away and fill with water during rain events.

Inwardly directed scallops indicate that intense rain events would cause back-flooding of the sediment-filled domal section. This back-flooding began to fluidize the sediment and cause inward collapse and stoping upward of this room. Scallops throughout Lillcher intensify in the smaller passages (higher fluid velocity) and dissipate in the larger open rooms that likely held water (lower fluid velocity) during flood events. The series of alternating void forming stages and infilling stages represents the multi-stage epigenetic processes present in Lillcher; in current times, the water is infiltrating through conduits from multiple locations and is simply following preferential flow paths along fractures and draining into a single conduit.

Ultimately, Lillcher Cave is largely a dendritic phreatic tube complex that has been heavily overprinted by vadose entrenchment and back-flooding processes. Based on the morphology of

the cave, where small, originally elliptical entry features taper into large domed rooms that then continue into small conduits; it is not unlikely that beyond the actively-entrenching, water-filled sump, Lillcher Cave continues into additional larger bedrock rooms similar to the original domal chamber prior to its collapse.

Death Tube Cave (Headwall Cave) (Fig. C2)

Death Tube Cave, originally named Headwall Cave when it was first recorded but not explored, is the longest cave located within the study area with a total surveyed length of 231 meters and depth of 15.5 meters. The cave forms at the base of a large 10-meter-tall headwall that is located within an expansive 300-meter by 150-meter drainage basin. The lower passage is formed completely within the Castile Formation and ranges in size from four meters tall and 1.5 meters wide at the entrance to areas that are entirely elliptical and merely half a meter in diameter. The upper passage is formed within partially lithified Quaternary gypsic sediments along a contact between sediment and bedrock; it ranges in size from 0.5 meters in diameter to a dome room that is four meters tall by five meters wide. From the entrance, both passages extend to the north, where the lower passage slopes downward and the upper passage arcs upward. For the first 30 meters, the lower passage maintains a highly fracture driven morphology with very narrow walls relative to ceiling height. The passage abruptly changes from tall and narrow to an elliptical tube that is approximately 0.75 meters in diameter and trends to the west along an intercepting fracture. Continuing for eight meters, this mud- and breakdown-filled tube then branches off into a west-trending side passage that is too tight to enter. Continuing to the north, this low crawlspace is maintained with a diameter of 0.75 meters and begins to shift to a northwestern trend following a fracture. This stretch of passage has clear side passages that

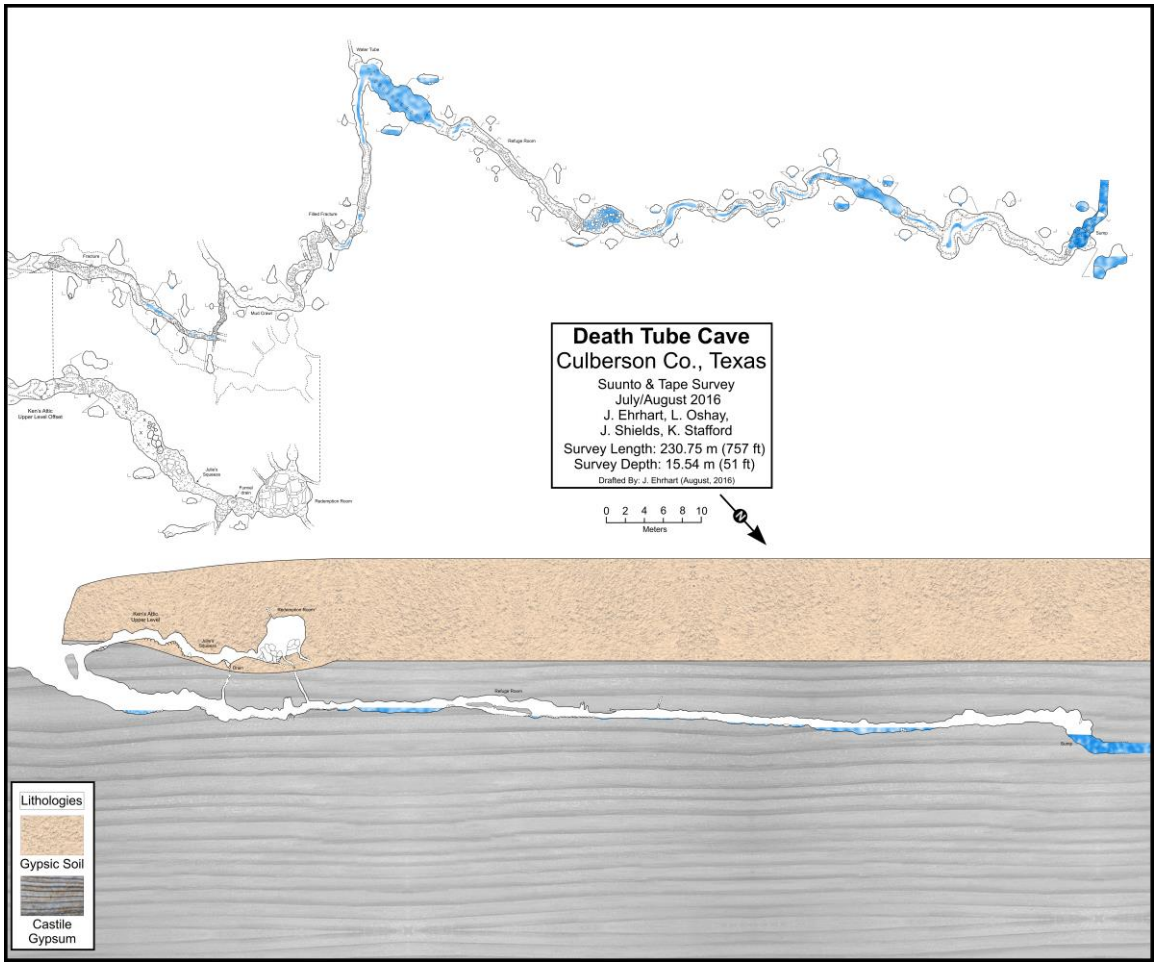

Figure C2: drafted cave map of Death Tube Cave.

are too tight to enter but are assumed to connect back into the main passage in a loop. The passage begins to widen laterally with a width of two meters and height of 0.75 meters at an area filled with 40 cm of water. The passage meanders along the axis of a fracture to the north and maintains an elliptical shape with a minor presence of entrenchment. After a series of tight crawls through tubes half filled with water and navigating around meandering passages where the walls are armored with half a meter of mud, the cave sumps out with an abrupt floor and ceiling drop.

The passage continues as a 1.5-meter diameter tube trending to the northwest completely under water.

The upper passage extends from the same bedrock opening as the lower passage and quickly changes into lithified gypsic sediment. The passage undulates with significant indurated soil breakdown for approximately 25 meters until terminating in a soil room that is four meters tall and five meters wide. At the entrance to this chamber, a tight squeeze (20 cm wide) has formed from large two-meter by three-meter breakdown blocks obstructing the passage. Within this room, several smaller passages that are too tight to explore extend in a radiating pattern downward. These passages presumably connect as piping features to the lower passage of the cave.

Death Tube Cave is a classic example of an originally epigene phreatic elliptical tube that has been overprinted by vadose processes. The distinctly elliptical morphology of the majority of the cave indicates that this cave originally formed when the water table was significantly higher than it is in modern times. Due to climatic change and regional base-level drops, the water table has since subsided and the cave has begun to undergo vadose entrenchment through the pre-existing fractures in which the phreatic tube originally formed. This entrenchment is much more significant within the first 30 meters of the cave; vadose entrenchment has yet to substantially affect the remainder of the cave where only small deviations from elliptical passages are present. The lack of distal entrenchment within the cave is not likely due to supersaturation or reduced fluid velocity as scallops are still heavily present. Vadose entrenchment is minimized due to the large amount of organic mud that has armored the floor walls reducing dissolution and ion mobilization. The inward direction and tight spacing of scallops suggest that Death Tube Cave is

periodically subject to high-velocity fluid flows that rush in during intense rain events. The water-filled sump contains very few scallops and may currently mark the maximum extent of water table recession. Throughout the cave, “bathtub rings” of organic material can be found which serve as indicators for the maximum extent of annual and short-lived flash flooding events, where backflooding is temporarily extended.

The upper passage of Death Tube Cave formed along a gypsum bedrock and gypsic soil contact; the boundary acts as a permeability horizon for the transport of water and dissolved sediment. This horizontal contact is intercepted by vertical fractures that follow a very similar trend to the lower passage. As Death Tube Cave filled during flash flooding events, the fractures within the overlying sediment and contact between sediment and bedrock became the preferential flow path for water migration. As water injected up through these fractures and soil, suffusion of the overlying sediments occurred. Fluidization of the partially-lithified sediments resulted in stoping upwards of the upper passage and initial soil cave formation. Along the ceiling in the large soil room, a series of 25-centimeter diameter inlet piping tubes follow a fracture. These inlets suggest that this soil dome could have sourced much of its water from the overlying surface. The increased influx of water down fractures and inlet tubes may have contributed to the accelerated upward stoping of this isolated soil room. The soil room outlet tubes, which are currently plugged at their openings, are likely the conduits in which the majority of the fluidized sediment transported out of the upper level and flushed through the lower passage. Based on the morphology and consistent aperture of Death Tube Cave, it is likely that past the current sump the passage continues for a considerable distance and resurges at a nearby spring (Willow Spring) or terminates in a lake room similar to what is found within Border Cave and Wiggley Cave.

Fissure Cave and Crushed Cave (Fig. C3)

Fissure Cave is located in the northern end of the Gypsum Plain and has a total surveyed length of 116 meters and depth of 10 meters. The feature is developed entirely within the Castile Formation and contains domes that are upwards of 10 meters tall and small elliptical squeezes that are less than half a meter tall. The entrance to Fissure Cave is located at the base of an arroyo and is expressed surficially as a five-meter-deep, one-meter diameter pit. From the entrance, the cave extends to the east into a fracture-controlled passage that contains a series of large domal structures. Continuing south, a fracture is intercepted and the ceiling drops to a tight squeeze approximately two meters tall by 50 centimeters wide. This area has a significant overhang which results in the humanly enterable passage being only 70 centimeters tall and 50 centimeters wide. Above the overhang, an open ceiling fracture, too tight to fit through, accounts for the other 1.3 meters to the ceiling of the squeeze passage. This squeeze ends in a small room that branches off in two directions. The north-trending passage tapers off and is solutionally widened near the ceiling and notched at the floor. Continuing south, the floor and ceiling both rise into an arcing passage that extends for 10 meters; this section contains many ceiling cupolas, small domes, elliptical inlet tubes, and is 0.75 meters wide and 1.5 meters tall. As the passage begins to slope downward, there is another small chamber that maintains a similar domal structure to the first room. The floor drops abruptly and the passage doubles back under itself continuing to slope downward following a fracture in the floor. This fracture is highly entrenched and meanders down towards the second level of the cave. The final stretch of the cave continues to the west horizontally for 30 meters and contains many ceiling dissolution features ranging from large expansive cupolas to small domes. The cave terminates after a tight squeeze

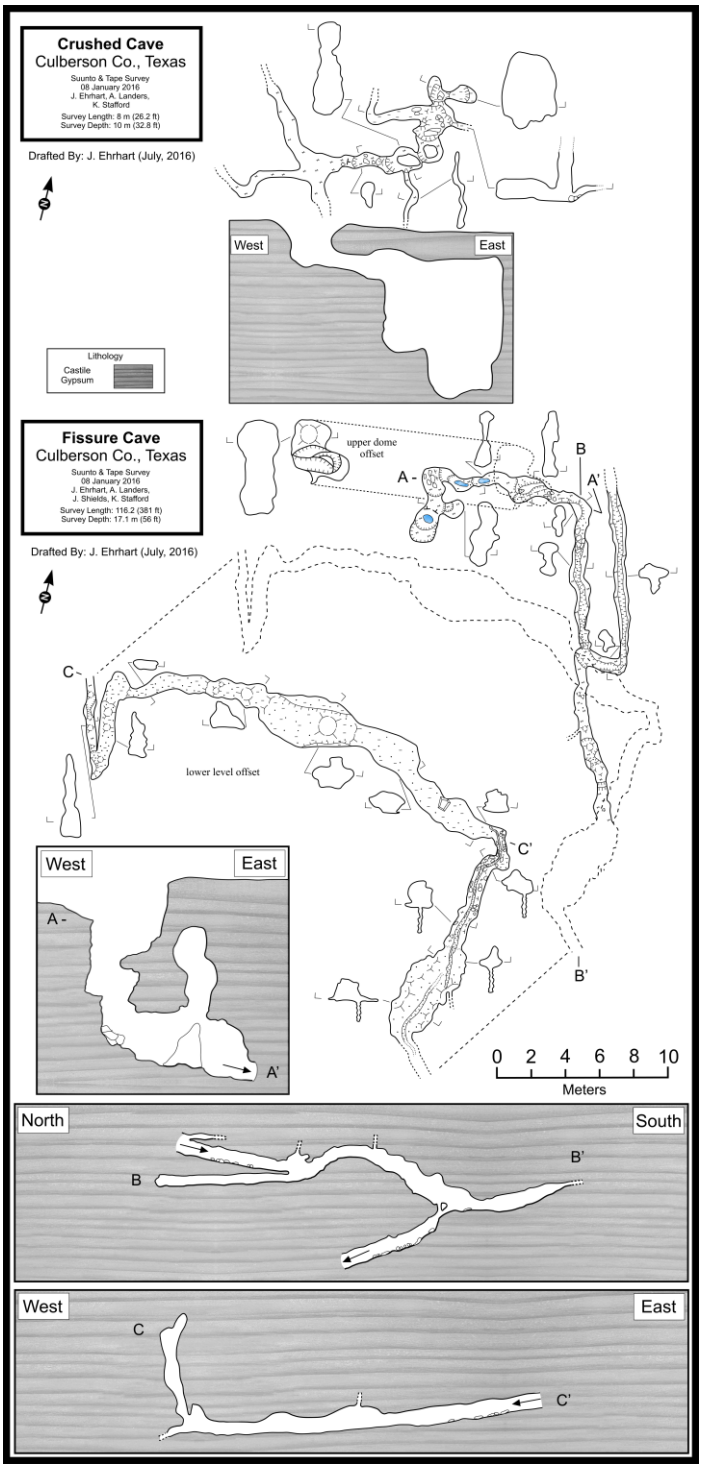

Figure C3: drafted cave map of Fissure Cave.

where a large 10-meter-tall and 2.5-meter-wide dome extends vertically.

Fissure Cave is one of three surveyed caves located within the study area that was formed primarily by hypogene processes. This cave is a multi-level, fracture-controlled hypogene cave that has been moderately overprinted by epigene vadose entrenchment. At its inception, water flowed up from depth finding the path of least resistance along fractures and began to dissolve out the first vertical dome that is present within the lowest point in the cave. Over time, this upward dissolution expanded down a series of fractures trending to the east. The lower level passages contain many morphological features such as large domes and cupolas which are indicative of a hypogene origin. Scallops within the lower passage are essentially nonexistent outside of what has been overprinted in the vadose entrenched fracture zone. Throughout Fissure Cave, the overwhelming majority of the ceiling and walls are completely smoothed from ascending waters in a sluggish flow regime.

It is likely that the entrance pit into Fissure Cave is simply a hypogene dome that has since been breached. This breach began the epigene overprinting and entrenchment found in the first room where the passage meanders and splits. This room contains large mounds of gypsum flowstone that likely deposited during periodic stages of flooding. During more significant rain events, enough water flows in through the entrance and split passage to make it down to the lower level. Once at the lower level, this influx of water funnels through the large fracture and has since entrenched this fracture zone multiple meters. Beyond this point, the lower level remains as a relict feature of the original hypogene environment; this is due to the fracture diverting all vadose epigene flow.

Crushed Cave is located just 20 meters north of Fissure Cave and has a surveyed length of eight meters and a depth of ten meters. The entrance to Crushed Cave is approximately one-meter-tall and half a meter wide; where the ceiling and floor abruptly drop down into a set of downward stepping pits. The cave is primarily one large hypogene dome where water ascended and carved out a large dome. This dome was later breached, and the epigene processes took over. Due to logistical reasons, Crushed Cave was not able to be pushed further. There is, however, a passage that contains many morphologically-similar characteristics to a split passage within Fissure Cave. Due to their close proximity and similar characteristics, it is likely that Fissure Cave and Crushed Cave are connected.

Wiggley Cave (Fig. C4)

Wiggley Cave is the deepest cave in the study area and is located just east of the well-known, Border Cave. Similarly to Border Cave, Wiggley Cave is a large and expansive feature originally formed in the hypogene environment. The cave is 189 meter long, 49 meters deep, and gives access to a lower level lake of deep phreatic water. The single entrance into Wiggley Cave is situated at the end of a 12- meter deep, 250-meter long by 145-meter wide arroyo that occasionally floods along with the cave itself. From the entrance, the cave extends to the north clearly following a fracture in the ceiling into a largely entrenched single passage with a few inlet tubes and several pools of freshwater. Wiggley Cave often abruptly changes direction as it intersects fractures but maintains a consistent width of about one meter. As the cave extends, the passage floor entrenches more and more while the ceiling remains level. Within the first 100 meters of the cave, the entrenchment is gradual but begins increasing rapidly beyond this point.

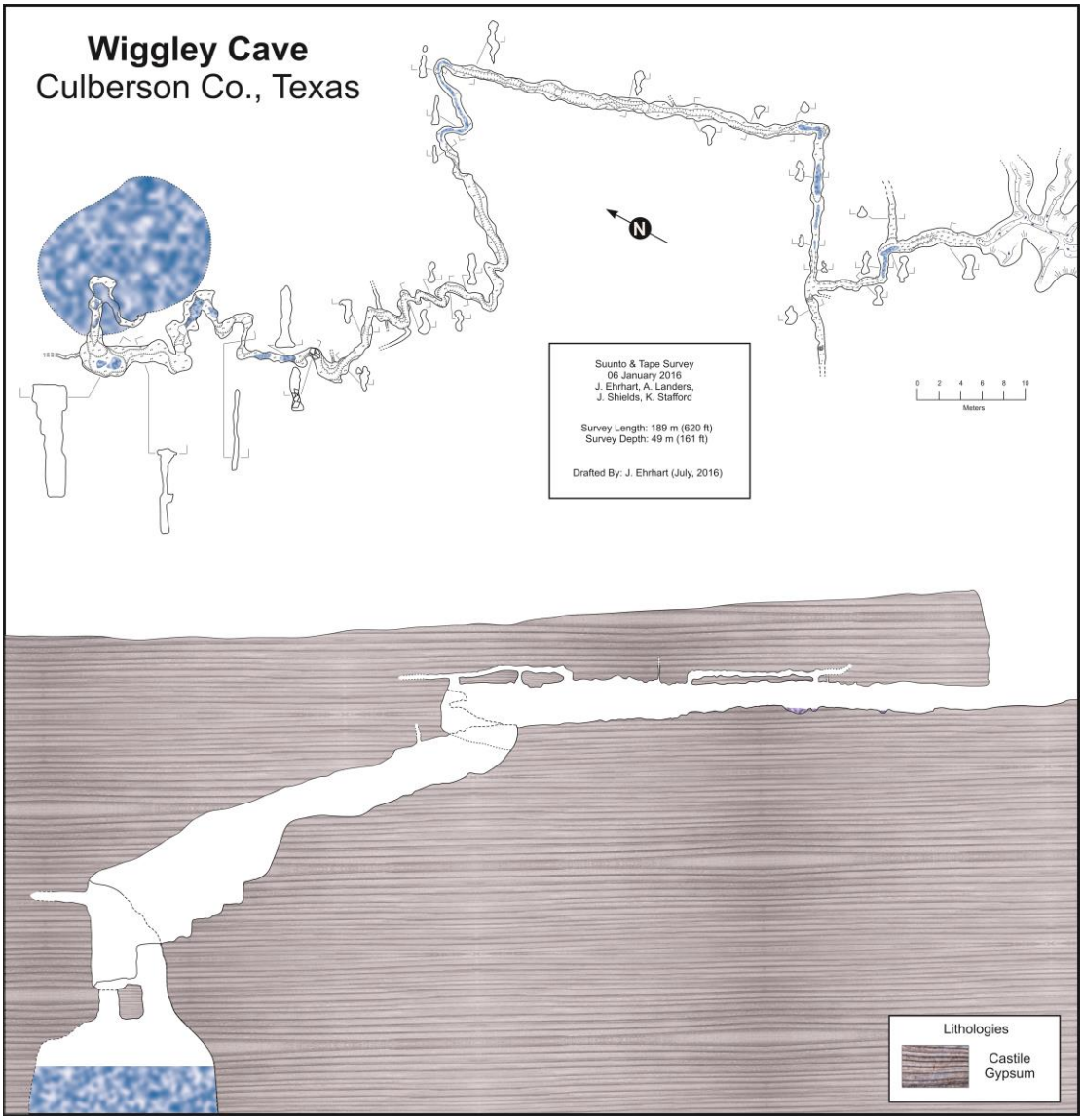

Figure C4: drafted cave map of Wiggley Cave.

As the passage meanders back and forth, the cave walls rapidly grow taller ranging from just under two meters at the entrance to over 15 meters at the lake room. In cross section, the passage maintains a primarily elliptical shape near the ceiling and wedge-like vertical trench towards the floor. After a series of floor drops, Wiggley Cave terminates in a large eight-meter drop into a

lake room that is approximately 20 meters in diameter. The elliptical nature of the upper segments of the cave passages and the presence of a large domal lake room suggest that the formation of Wiggley Cave was likely a result of ascending water within a hypogene environment. Today, this originally hypogene environment has been breached and significantly overprinted by epigene processes. The inception of Wiggley Cave began with ascending water carving out the main lake room; as this room expanded and exposed fractures, water began to inject and form solutionally widened phreatic tubes. Remnants of these tubes can be seen in the uppermost sections of the passages as nearly perfectly circular conduits. Once these solutionally-widened fractures breached at the land surface, epigenetic processes began altering and overprinting the preexisting morphology. The primary epigene process that has altered Wiggley Cave is the massive amount of vadose entrenchment from very large influxes of water; which is entirely possible with such an expansive watershed. The influxes of water that occurred during large rain events dissolved deep trenches into these once elliptical if not circular passages. Today, entrenchment similar to that which has been ongoing for thousands of years is still ongoing. Dissolved ions that are washed into the lake room are likely piping out through lower conduits in the lake floor.

Valley Cave (Fig. C5)

Valley Cave is located on the northern end of the study area within the gypsum bedrock of the Castile Formation. The cave extends nine meters in length and four meters in depth. The entrance into Valley Cave is approximately one-meter-tall, half-a-meter-wide, and is located along the periphery of a collapsed sinkhole. The cave floor is lined with breakdown and sediment , and the walls are pure gypsum bedrock that has begun to dissolve preferentially along the varved laminae. Valley Cave runs along a fracture in the ceiling and is intercepted sub-

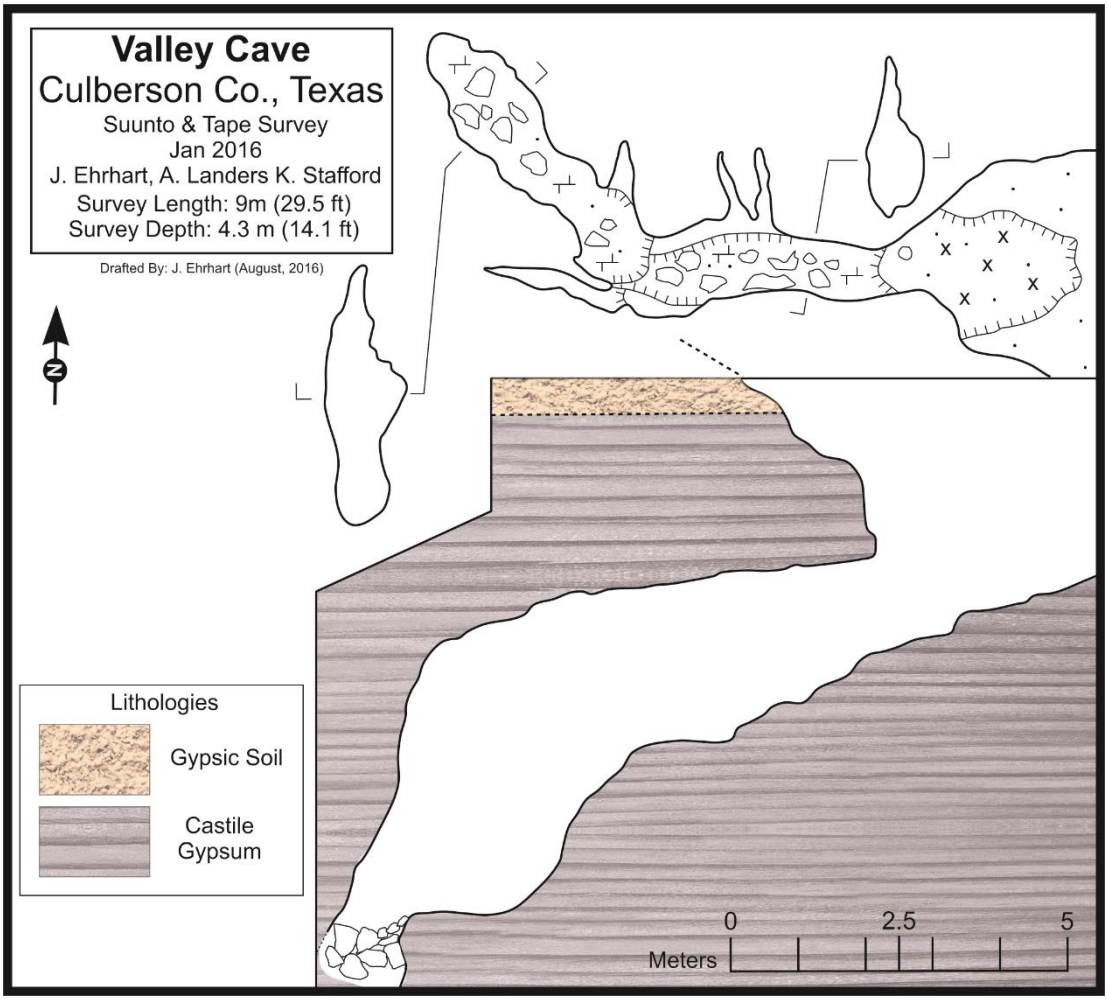

Figure C5: drafted cave map of Valley Cave.

perpendicularly by multiple other fractures that are solutionally widened. The main fracture eventually becomes too tight to enter and is filled with breakdown. Valley Cave formed under epigene conditions where a fracture has become solutionally-widened and entrenched. After the collapse of the surrounding sinkhole, fractures were exposed to surficial flows and susceptible to vadose entrenchment.

<u>Frac Soil Cave</u> (Fig. C6)

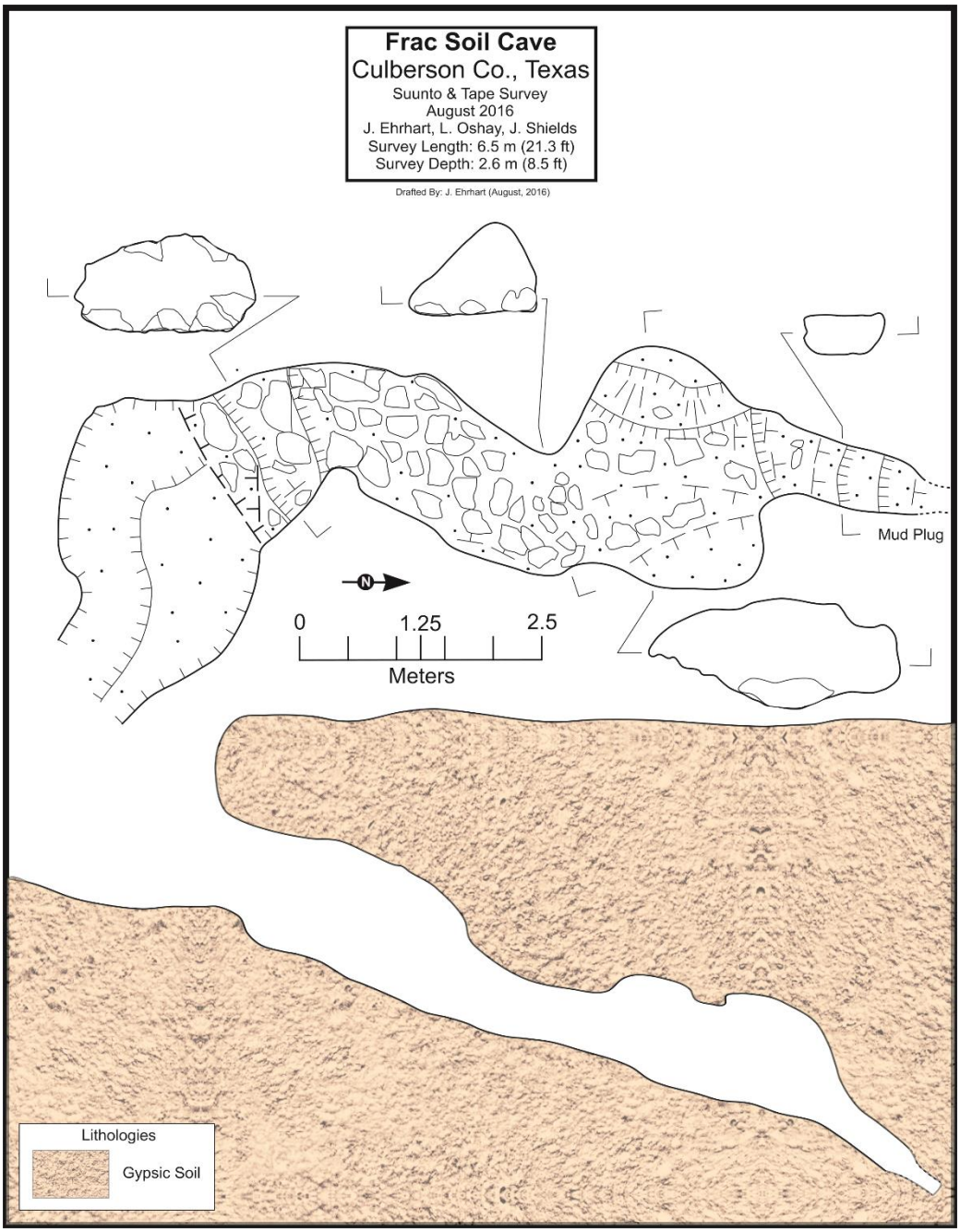

Figure C6: drafted cave map of Frac Soil Cave.

The entrance to Frac Soil Cave is located entirely within indurated gypsic soil. The entrance is at the base of a small soil collapse feature and is approximately two meters wide and 0.75 meters tall. The cave extends 6.5 meters in length and 2.6 meters in depth. The floor of the cave is composed of indurated sediments and breakdown. The cave begins at what appears to be a collapsed soil room and then widens into a soil chamber that is 1.25 meters tall and almost three meters wide. This room has a domal morphology and ultimately terminates in a small, half meter diameter, soil tube that is plugged with mud. Frac Soil Cave formed as a suffosion feature where fluidized sediments were piped down into conduits. When suffosion caves backflood, sediments rapidly dissolve which induces ceiling failure and the formation of small domes.

<u>Skylight Fracture Cave</u> (Fig. C7)

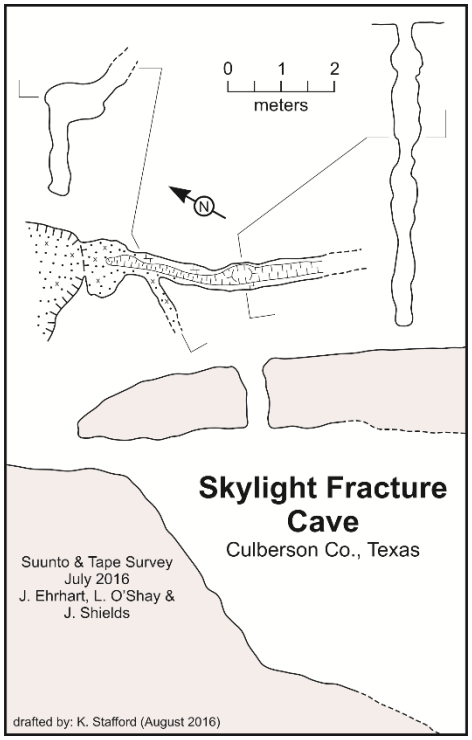

Figure C7: drafted cave map of Skylight Fracture Cave.

The surface expression of Skylight Fracture Cave is relatively small with an entrance diameter of 40 centimeters. The entrance is located at the end of a small arroyo where the cave extends for at least four meters in length and five meters in depth. The solutionally-widened fracture that makes up the primary cave passage is 40 centimeters wide and is too tight to explore more than a couple meters. A borescope was used down a second entrance tube which shows signs of the cave extending much further along this fracture. As the name would suggest, Skylight Fracture Cave clearly formed along a fracture that was solutionally-widened and entrenched by epigene vadose processes.

<u>Broken Rock Cave</u> (Fig. C8)

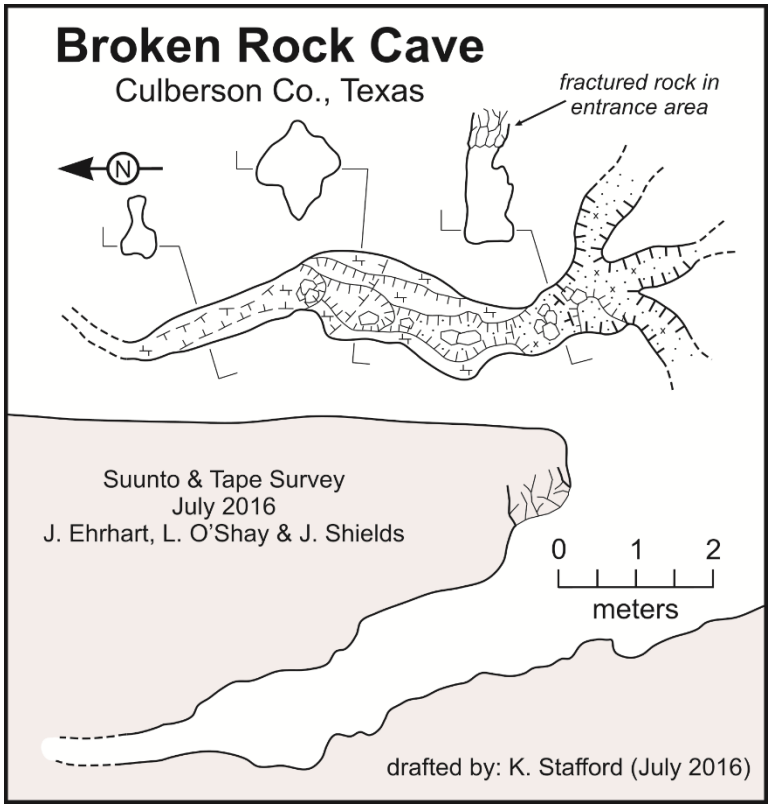

Figure C8: drafted cave map of Broken Rock Cave.

Broken Rock Cave is a small epigene feature formed as an entrenched and solutionally-widened fracture that is six meters long and three meters deep. The cave is at the base of a ten-meter diameter, three-meter-deep sinkhole that drains into an open cave with a crawlway entrance passage. The entrance is highly fractured and approximately 1.5 meters tall and 0.75 meters wide. Continuing north, the cave follows the trend of a ceiling fracture, and after a rapid aperture decrease, the cave terminates in a pinch out.

<u>Gnome Cave</u> (Fig. C9)

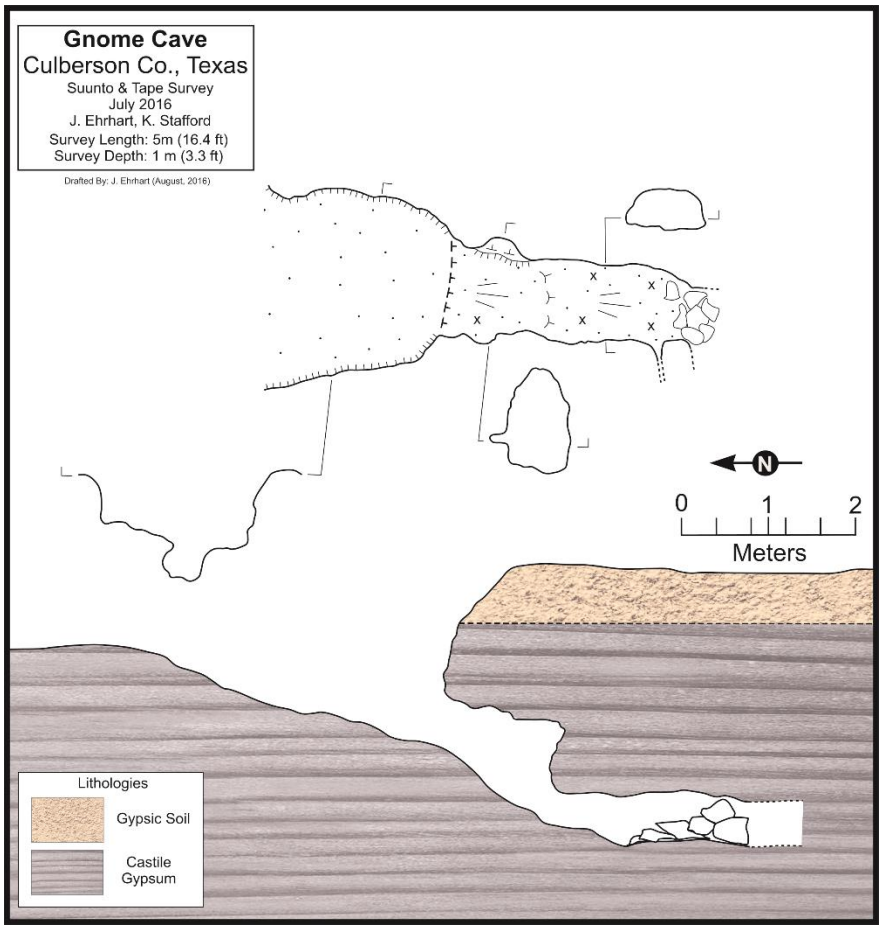

Figure C9: drafted cave map of Gnome Cave.

Gnome Cave is a small entrenched and solutionally widened fracture formed by epigene processes that begins at the base of a one-meter-deep arroyo within gypsum bedrock. The entrance is 0.5 meters tall by one meter wide and slopes downward along a widened fracture. The floor is composed of alluvium covered bedrock and the cave terminates at a breakdown junction where multiple ten-centimeter-wide fractures split off. Surficial water injection and subsequent entrenchment were the primary mechanisms that formed Gnome Cave. Some suffosion of the overlying indurated soils likely occurred as the cave was solutionally widening.

<u>Side Door Pit Cave</u> (Fig. C10)

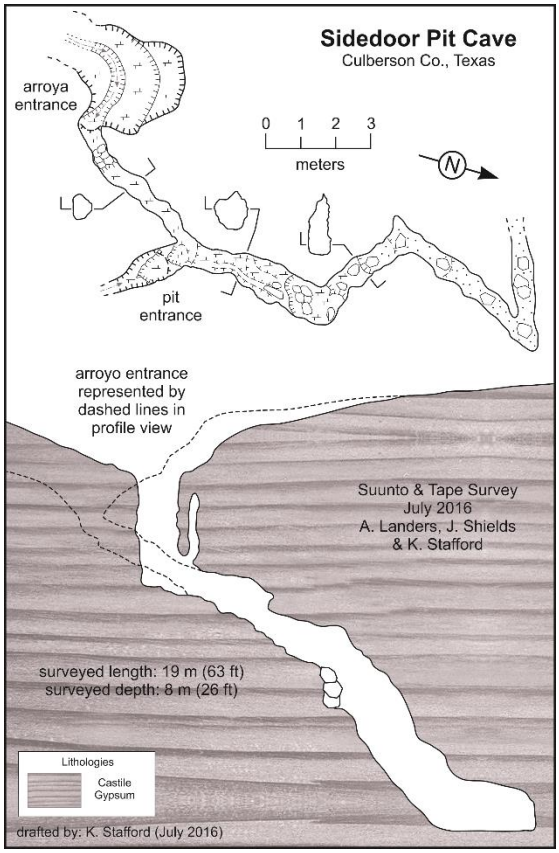

Figure C10: drafted cave map of Sidedoor pit Cave.

Side Door Pit Cave is an epigene vadose entrenchment cave that has two primary entrances within gypsum bedrock. The first entrance is surficially exposed as a one-meter diameter pit and the second entrance is a low gradient arroyo entrenched fracture. A 20-meter by 37-meter arroyo acts as the watershed for these two cave entrances. These entrances merge into a single passage that is approximately six meters long and five meters deep. The floor of the cave is composed of breakdown and lined with sediment. Floor drops and ceiling drops are common until the cave terminates in a plugged passage.

<u>Cat Widow Caves</u> (Fig. C11)

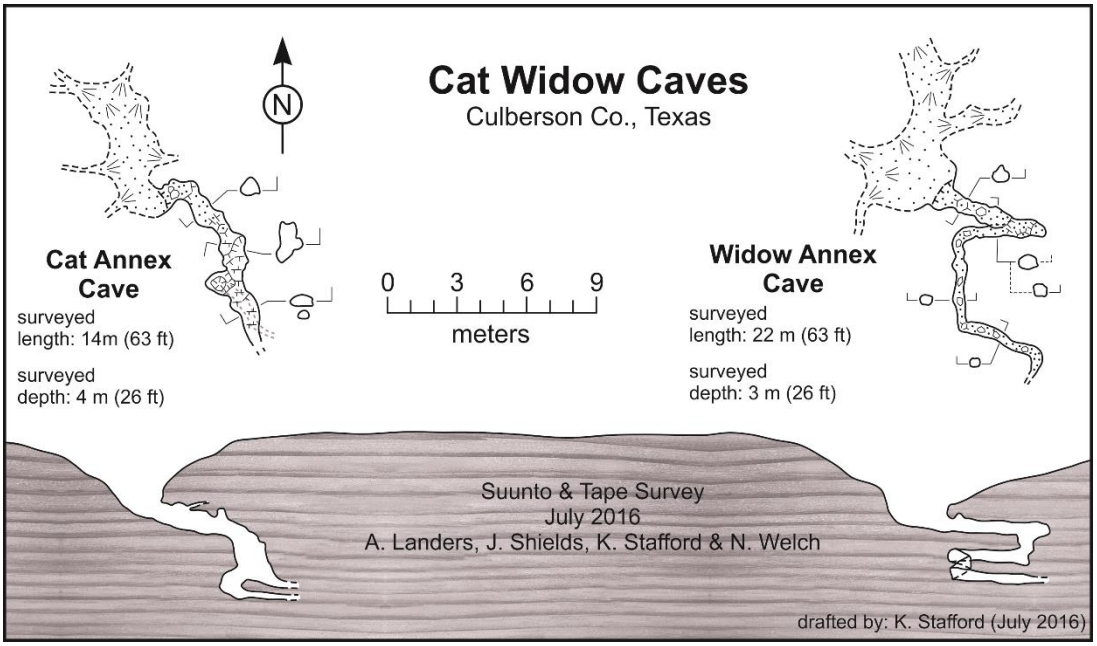

Figure C11: drafted cave map of Cat Widow Caves.

The Cat Widow Cave series consists of two separate caves named Cat Annex Cave and Widow Annex Cave. Because these caves are within such proximity, it is likely that they connect at depth. The entrance to Widow Annex is at the base of a large sinkhole with five arroyos

converging towards a single entrance that is 1.5 meters wide, 0.75 meters tall and trends sub-horizontally towards the road. The surveyed length of Widow Annex Cave is 22 meters and depth is three meters. The cave doubles back on itself following ceiling fractures. The cave floor is primarily composed of loose sediment that has washed in from the surrounding surface, but some breakdown is also present.

Similar to Widow Annex Cave, Cat Annex Cave opens at the end of a large 10-meter diameter and three-meter-deep incised sinkhole. The entrance is approximately one-meter-tall, 0.75 meters wide and trends towards the road slightly dipping as a sub-horizontal solutional conduit. Cat Annex extends 14 meters in length and four meters in depth. The passage continues to the east until splitting into two small passages and terminates in a mud plug.

Both caves within the Cat Widow Caves series are a result of epigene vadose entrenchment. Exposed fractures acted as preferential flow paths for gravity driven water migration and led to the formation of solutionally widened and entrenched passages.

The Hole Cave (Fig. C12)

As the name implies, The Hole Cave is a small, solutionally-widened and fracture-oriented, vadose-entrenchment feature that is lined with sediment. The single entrance is located at the end of a 15-meter diameter and 1.5-meter-deep sinkhole. From its 0.75-meter-tall by two-meter-wide entrance, the cave extends approximately four meters horizontally and one meter vertically. The cave floor contains some bedrock breakdown but remains relatively horizontal. At the back of the cave, one small passage continues that is too tight to enter but begins to slope upward. The Hole Cave formed by entrenchment and dissolution along a pre-existing fracture.

Due to the proximity of the overlying gypsic soil, suffosion also contributed to the inward piping of sediment.

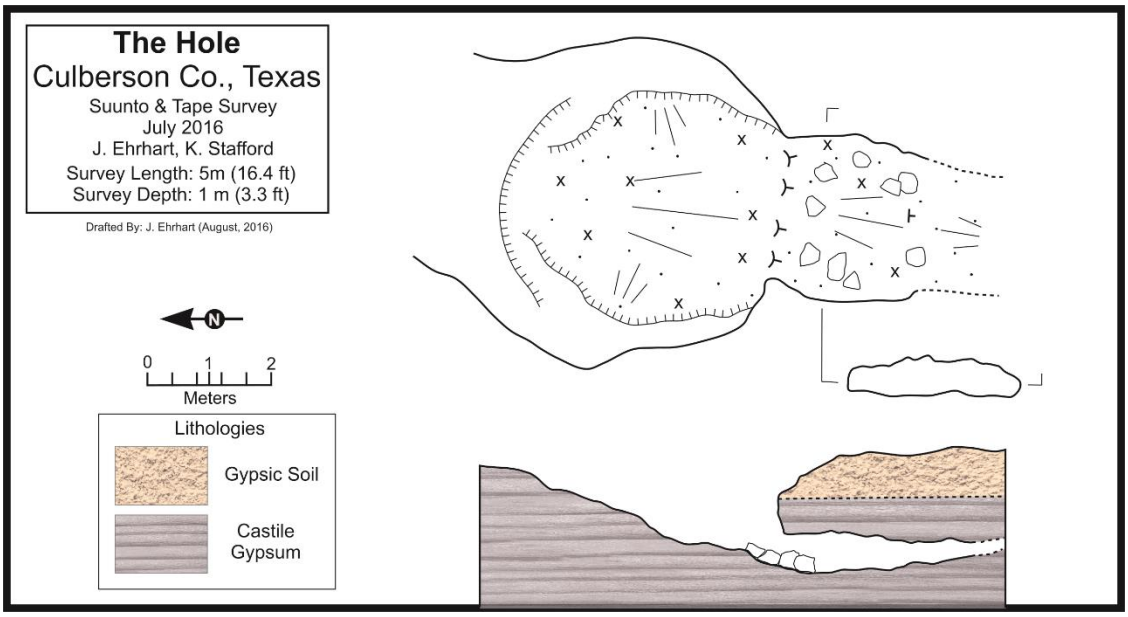

Figure C12: drafted cave map of The Hole Cave.

<u>Mousey Hole Cave</u> (Fig. C13)

Mousey Hole Cave has two entrances, one of which is on the periphery of a grass filled sink along an arroyo, and the second is in the form of a ten meter by eight meter collapsed sink. The entrances are located within the headwalls of sinkholes and are completely within indurated gypsic soil. From the arroyo entrance, the cave extends horizontally for 71 meters and vertically for three meters. The collapsed sinkhole intercepts the cave passage approximately 30 meters in. At the base of the sinkhole, the passage continues into the subsurface. Throughout Mousey Hole Cave there are a series of downward piping soil conduits that radiate out in all directions. The floor of the cave is primarily composed of gypsic soil breakdown and detritus that was carried in

by animals / water. Mousey Hole formed purely within an epigene environment. Water began to pipe through and dissolve sediments within fractures in the soil. This dissolution created void space for increased water migration. The current sinkhole entrance was likely a domal room that

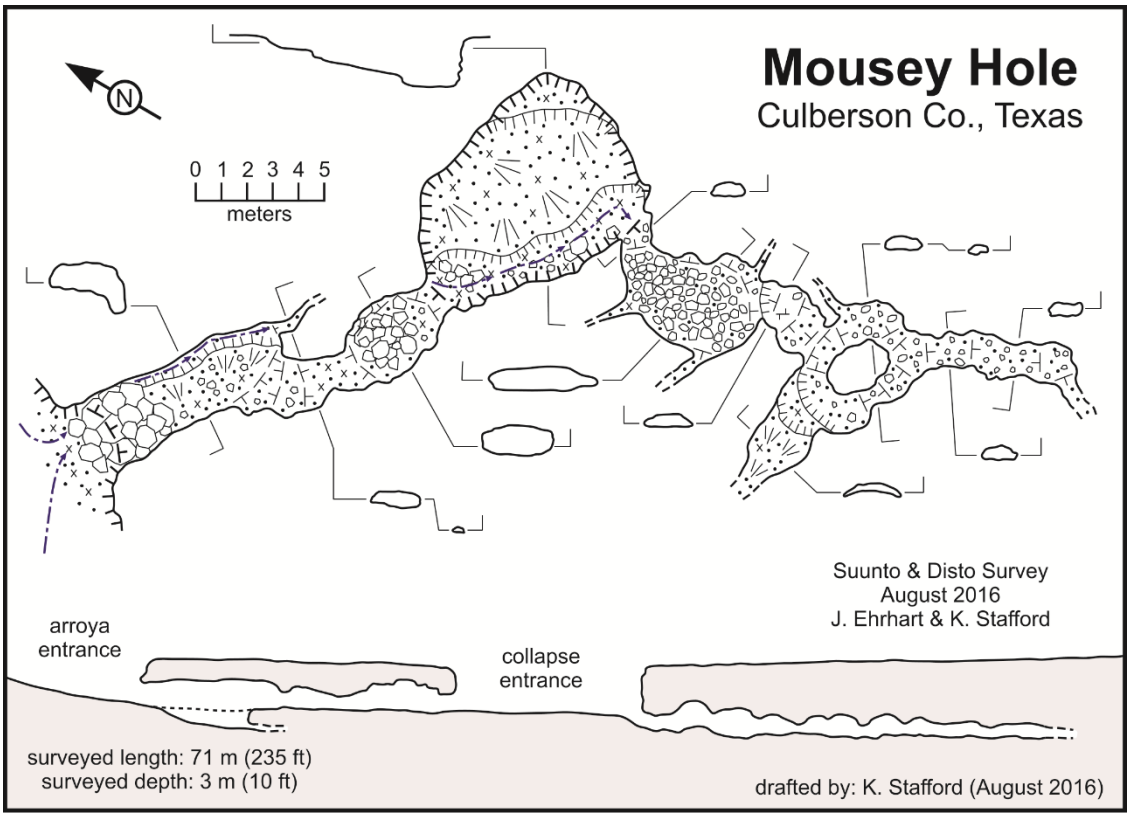

Figure C13: drafted cave map of Mousey Hole Cave.

was carved out by soil suffosion and fluidization during times of backflooding. Due to the unstable nature and reduced aperture of Mousey Hole it could not be surveyed further; however, beyond the currently surveyed passage, it is likely that a series of soil rooms with low crawlway connection passages exists.

Nikad Cave (Fig. C14)

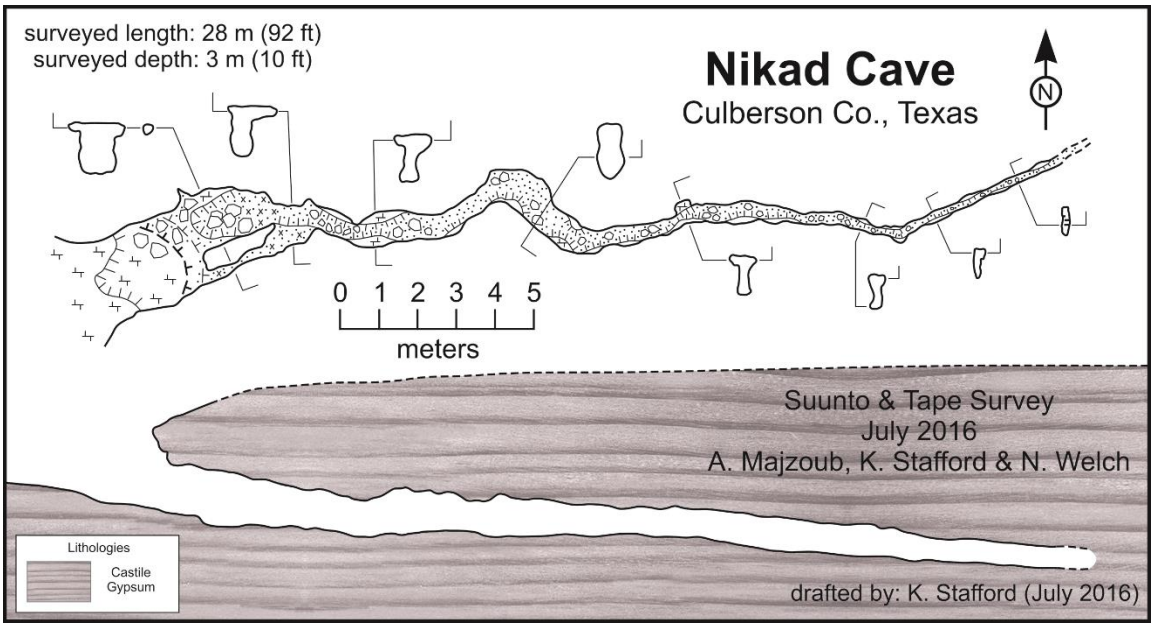

Figure C14: drafted cave map of Nikad Cave.

Nikad Cave is located at the end of a large 40-meter-long, 30-meter-wide arroyo that is 2.25 meters deep. The entrance to Nikad Cave is one meter in diameter and is located entirely within gypsum bedrock. The cave extends for 28 meters as a single, relatively straight and horizontal passage. The passage width tapers down from one-meter-wide at its entrance to less than 30 centimeters wide at the end of the survey. The cross-sectional trench like morphology is indicative of and suggests that this cave was formed as a fracture-dominated,epigene feature. As water percolated through the subsurface and solutionally-widened this fracture-dominated system, it began to channelize in the shape of an arroyo and entrench the floor of the cave. The presence of an inward-reducing aperture is a definitive indicator that a cave has formed with the vadose zone. The aperture decreases inward due to an increase in sulfate saturation and decrease in fluid velocity along the recharge flow path.

<u>Rockwall Cave</u> (Fig. C15)

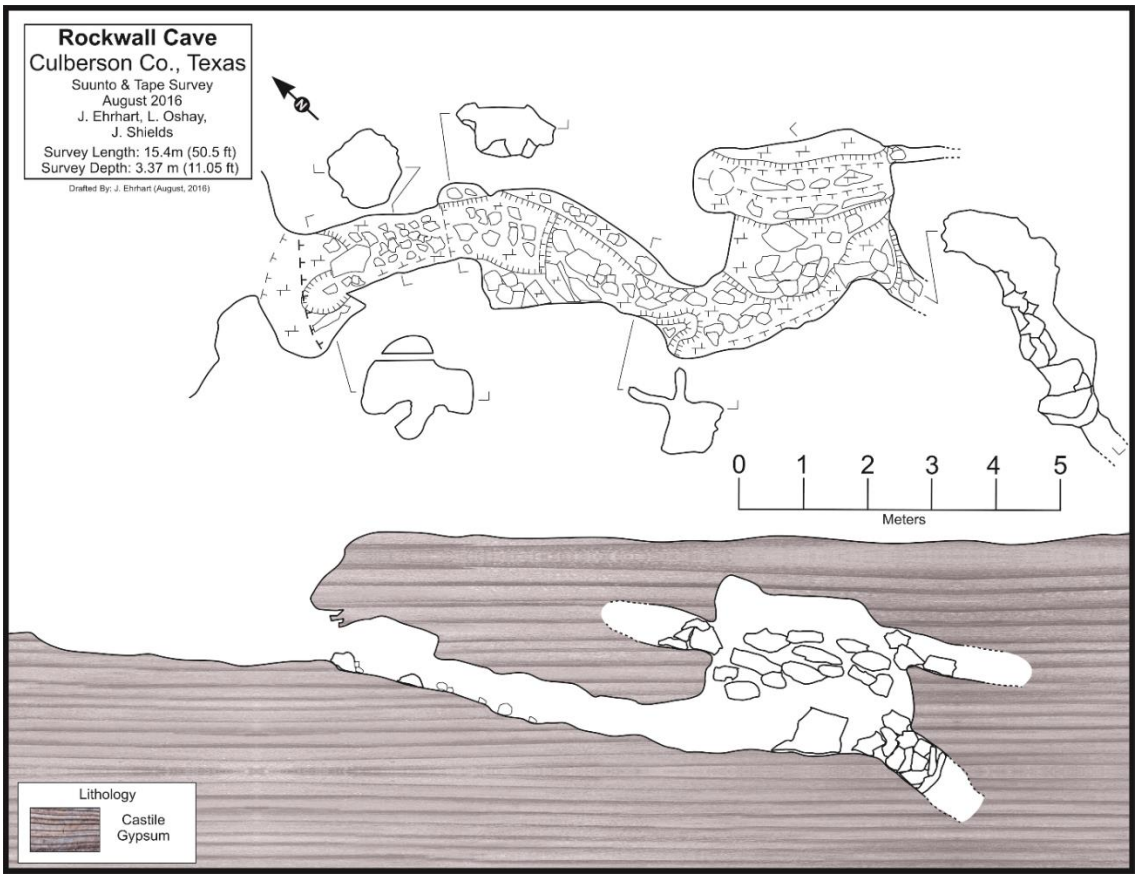

Figure C15: drafted cave map of Rockwall Cave.

Rockwall Cave is located within an arroyo that is greater than 70-meters-long and 2.5 meters deep. This arroyo leads to the cave entrance which is approximately 1.5 meters in diameter. Rockwall Cave is located wholly within gypsum bedrock and follows vertical fractures and tilted bedding planes for a total of 15.5 meters. The cave contains many floor and ceiling drops, and the floor is composed primarily of bedrock breakdown. Five meters into the cave, the ceiling begins to open up at a 45-degree angle. This slope is effectively a five-meter-tall rock wall covered in breakdown. Three, 0.75-meter diameter additional passages branch off from this room;

two exit horizontally along the ceiling and one drains through the floor but is currently blocked by breakdown.

Rockwall cave formed as water percolated down through either a sub-horizontal fracture or bedding plane of increased permeability. This downward migration of fluids dissolved out a large sloping void space. Some time later, due to the growing ability of this cave to transport water, new fractures began to widen and eventually breach at the surface. This caves morphology represents an example of a two-stage epigene dissolution history.

JC Gypsum Hole (Fig. C16)

The entrance to JC Gypsum Hole is located at the end of a 100-meter diameter by four-meter-deep sink that has a large arroyo development. The entrance is 0.5 meters wide by 1.25 meters tall and has a surveyed length of 35 meters and depth of 6.4 meters. The floor is primarily composed of detritus that has washed in but also contains the occasional breakdown block. Periodically, solutionally-widened fractures intercept the main cave passage and branch off. These fractures are much too tight to explore but represent the heavily fractured nature of the area. The cross-sectional trench like morphology suggests that this cave was formed as a fracture-dominated epigene feature. As water percolated through the subsurface and solutionally-widened this fracture-dominated system, it began to channelize in the shape of an arroyo and entrench the floor of the cave. This classic example of purely vadose entrenchment displays an inward reducing aperture as a result of an increase sulfate saturation and reduction in fluid velocity along the conduit flow gradient.

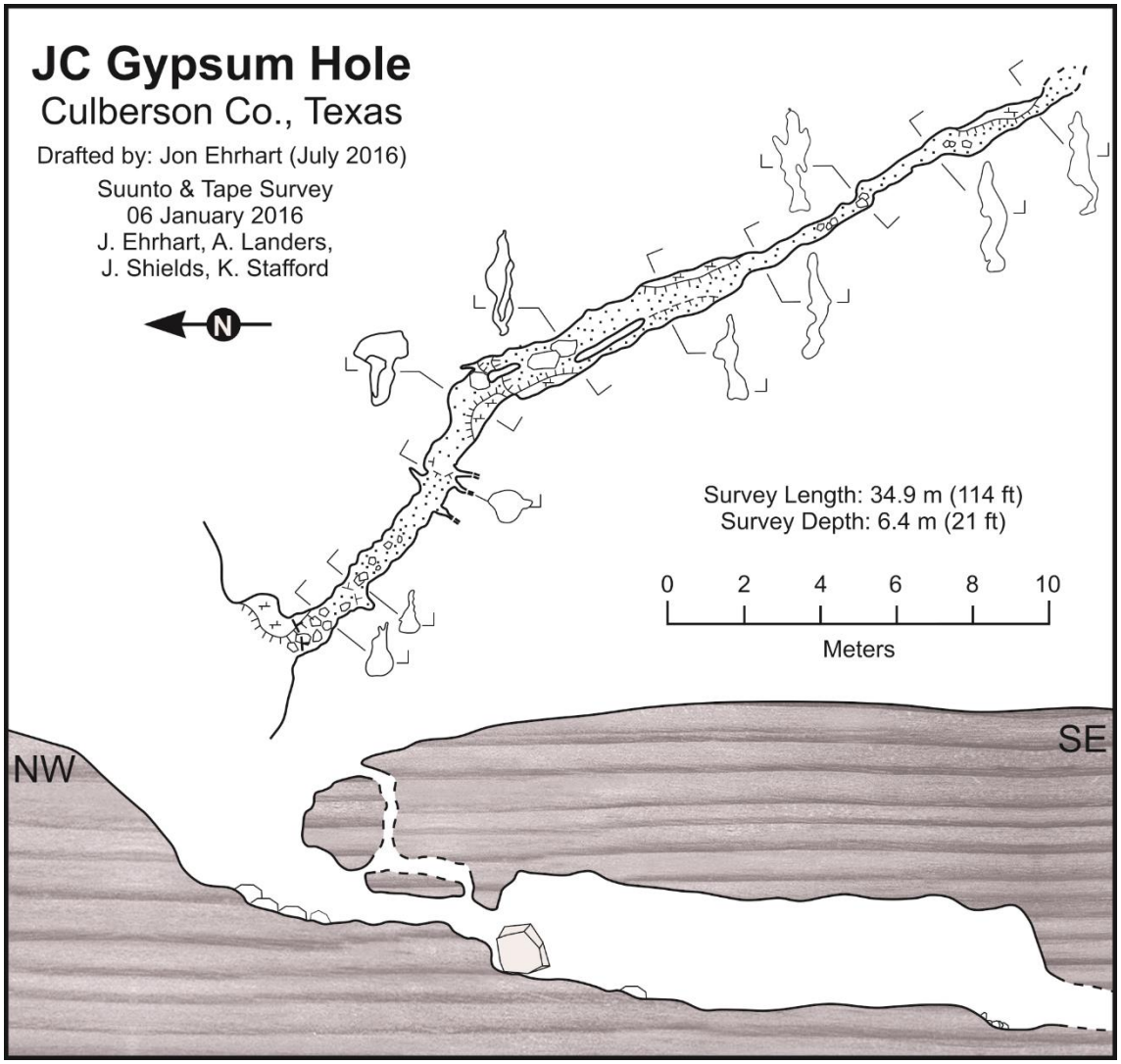

Figure C16: drafted cave map of JC Gypsum Hole Cave.

<u>Paleochannel Caves</u> (Fig. C17)

The Paleochannel Caves are split into two separate caves named West Paleochannel Cave and East Paleochannel Cave. As the name implies, these two caves are located along a gypsite soil,filled paleochannel. Along the southern periphery of this channel, suffosion induced soil caves are present. East Paleochannel Cave is the smaller of the two with a surveyed length of

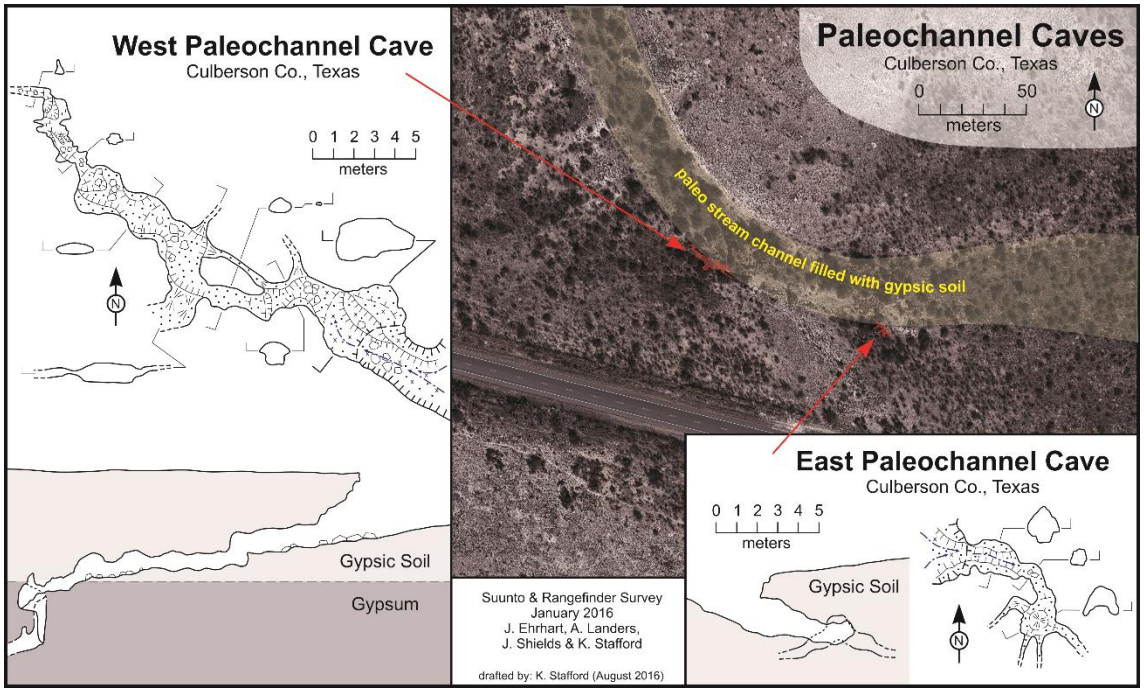

Figure C17: drafted cave map of Paleochannel Caves.

seven meters and depth of fewer than three meters. West Paleochannel Cave follows the periphery of the paleochannel and extends 12 meters horizontally and four meters vertically ultimately ending in gypsum bedrock. The entrance diameter is approximately 1.5 meters and tapers down to a passage that is less than 30 centimeters tall in bedrock at the distal end of exploration. Both of these indurated soil caves formed as soil piped through fractures transporting sediment to lower conduits within the bedrock. It appears that East Paleochannel Cave is the upgradient end of the cave system and that the intervening depression between the two caves represents approximately 80 meters of suffosion cave passage that has collapsed between the two entrances. The Paleochannel Caves are consistent with many of the other soil caves within the area. Small entry tubes expand to dome rooms that are subject to collapse; these collapse features transition into small radiating outlet tubes.

Bridge Cave (Fig. C18)

The entrance to Bridge Cave is located entirely within indurated gypsic soil. The entrance is at the base of an incised arroyo that is 35 meters long, 19 meters wide, and one meter deep. The cave extends for eight meters and is approximately one meter wide and 0.75 meters tall at the entrance. The floor of the cave is composed of indurated sediments and breakdown. The cave

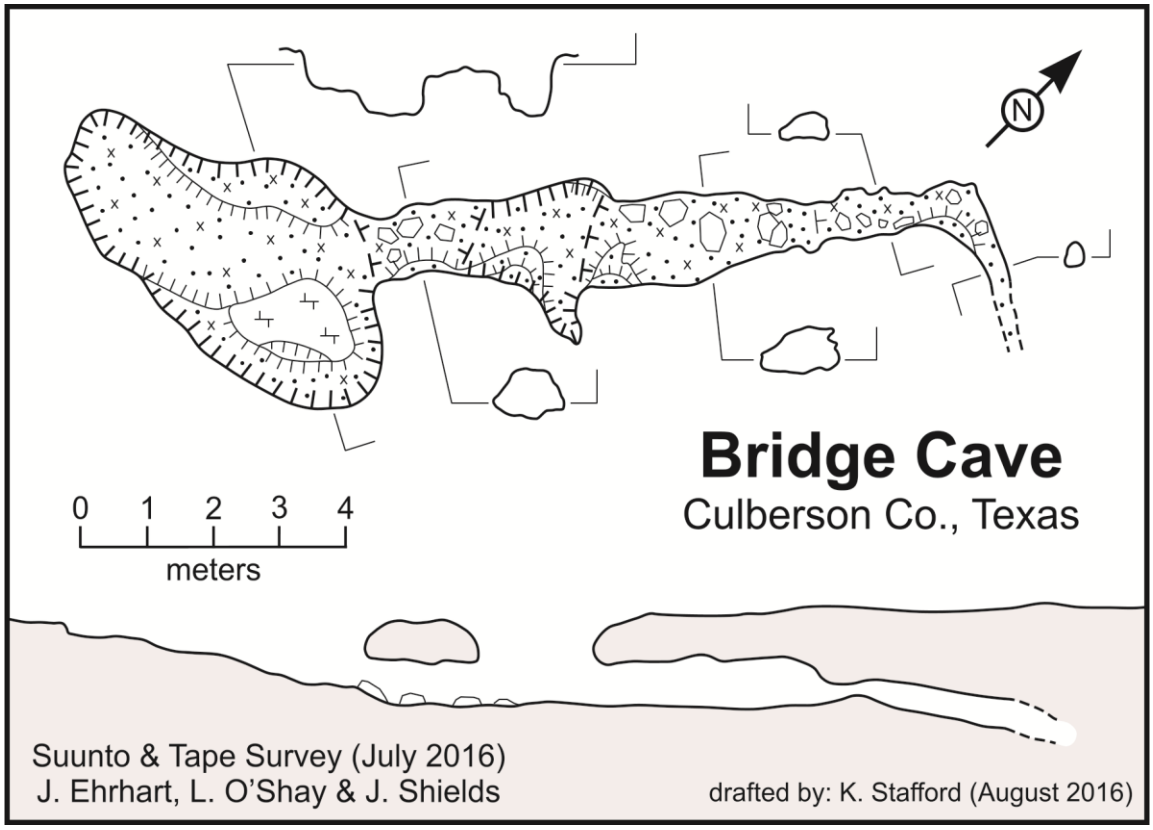

Figure C18: drafted cave map of Bridge Cave.

quickly opens into what appears to be a collapsed soil room and then continues back into the subsurface. Continuing northwest, Bridge Cave forms a domal soil room and then continually narrows from a passage that is one meter wide to 20 centimeters wide. The first room

encountered has a domal morphology and ultimately terminates in a small half-meter-diameter soil tube that is plugged with mud. Bridge Cave formed as a suffosion feature where fluidized sediments were piped down into conduits. When suffosion caves backflood, sediments rapidly dissolve and induce ceiling failure; these failures result in the formation of soil domes. With the volume of void space increased, the weight of overlying sediment becomes heavier than what can be supported by the underlying dome which results in ceiling collapse.

Airport Cave (Fig. C19)

Airport cave is located entirely within indurated soil at the end of a large 24-meter by 13-meter arroyo. The cave entrance is one meter tall by two meters wide and extends for a total surveyed length of eight meters long and depth of 3.4 meters. Similar to many of the soil caves located within the Gypsum Plain, Airport Cave is characterized by a relatively small entrance that transitions into a room that stopes upward and terminates at a small floor drain. Airport Cave formed as water began to pipe and dissolve sediments within fractures in the soil. This dissolution created void space that allowed for increased water migration and suffosion. The heavily vegetated entrance shows evidence of extensive use by local wildlife; javelinas were observed using the cave for shelter.

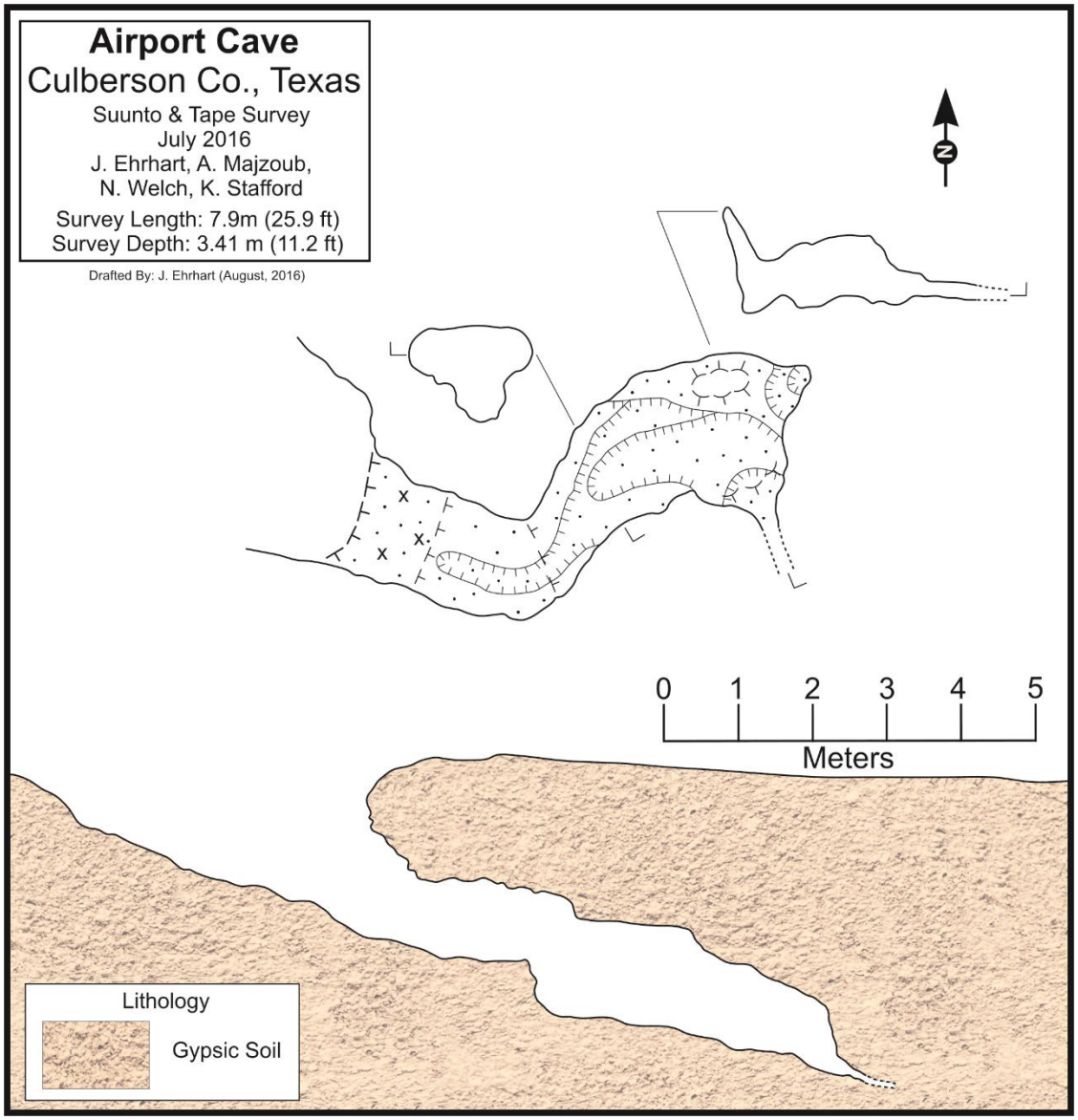

Figure C19: drafted cave map of Airport Cave.

<u>Pothole Complex</u> (Fig. C20)

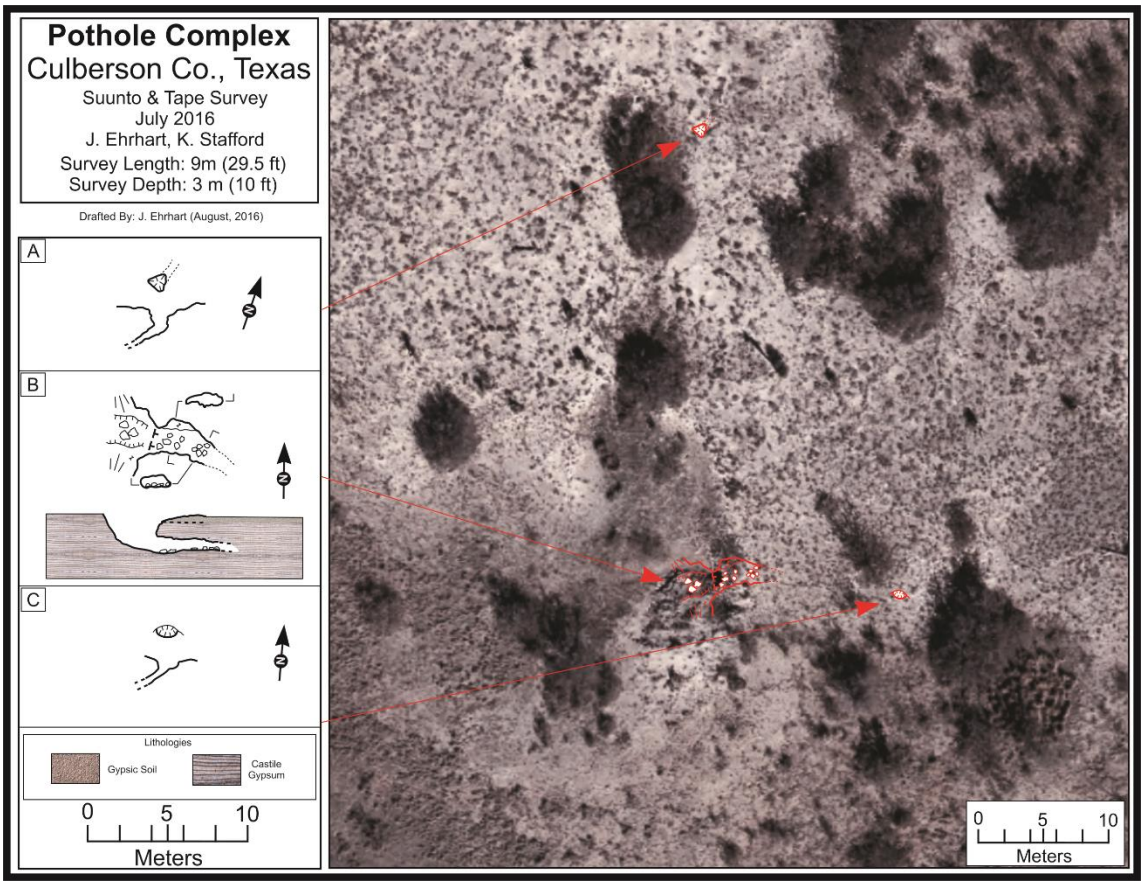

Figure C20: drafted cave map of Pothole Complex Caves.

The Pothole Complex is composed of three separate sub-horizontal caves that are surfically expressed as tubes. These tubes were formed within the gypsum bedrock of the Castile Formation and have a total measured length of nine meters and depth of three meters. The floor within these caves is composed of washed in alluvium and breakdown. The caves within the Pothole Complex are a result of epigene vadose entrenchment. Exposed fractures acted as preferential flow paths for gravity driven water migration and resulted in solutionally-widened and entrenched sub-vertical tubes.

<u>Water Tank Cave</u> (Fig. C21)

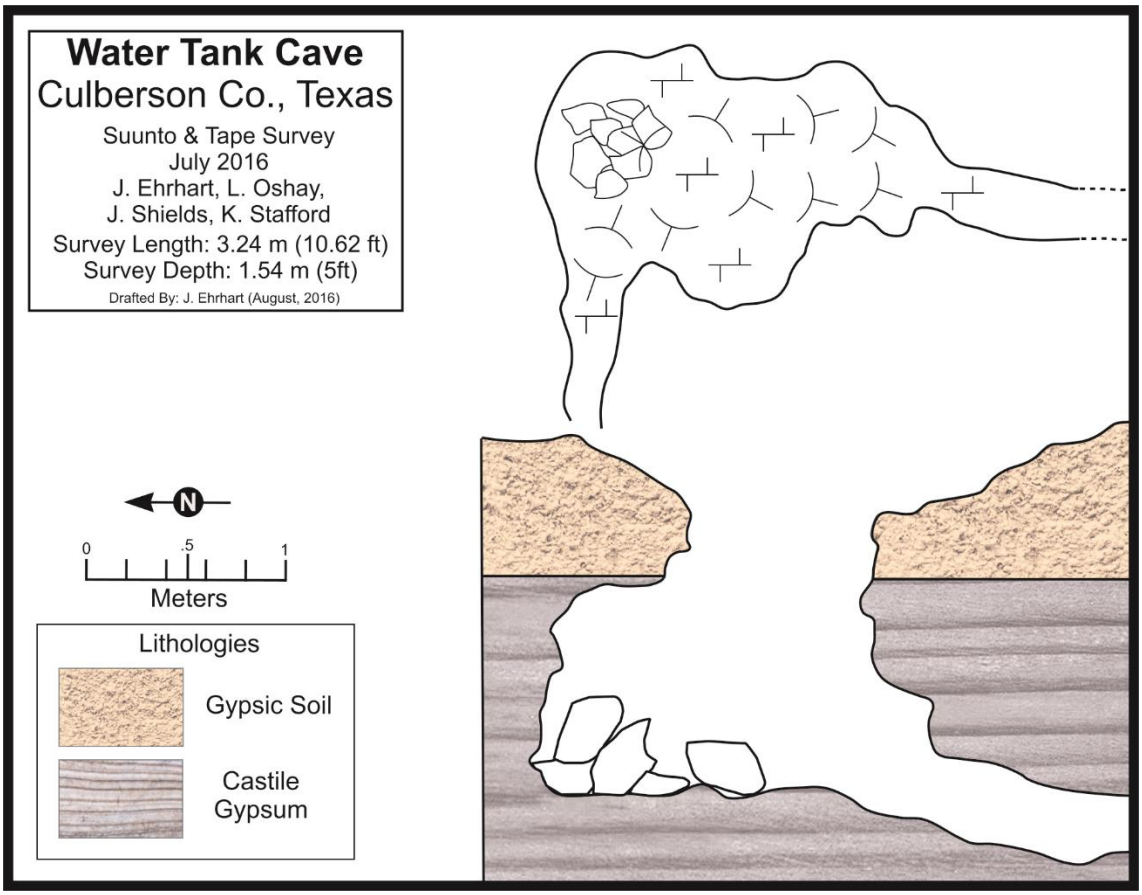

Figure C21: drafted cave map of Water Tank Cave.

Water Tank Cave is formed primarily within gypsum bedrock and represents a solutionally-widened fracture of epigene origin. The cave entrance is surfically-expressed as a pit that is one meter in diameter and 1.5 meters deep. At the base of the opening, f two passes continue to the south and west. The floor is composed of alluvium and breakdown. Although this feature appears to have a domal morphology, there is no indication that this cave was formed by ascending water. The presence of multiple fractures has allowed for the majority of surficial

water to flow vertically in a gravity driven system. When the preferential flow paths are vertical, water takes the path of least resistance, and lateral dissolution is reduced.

<u>Jon's Sink Cave</u> (Fig. C22)

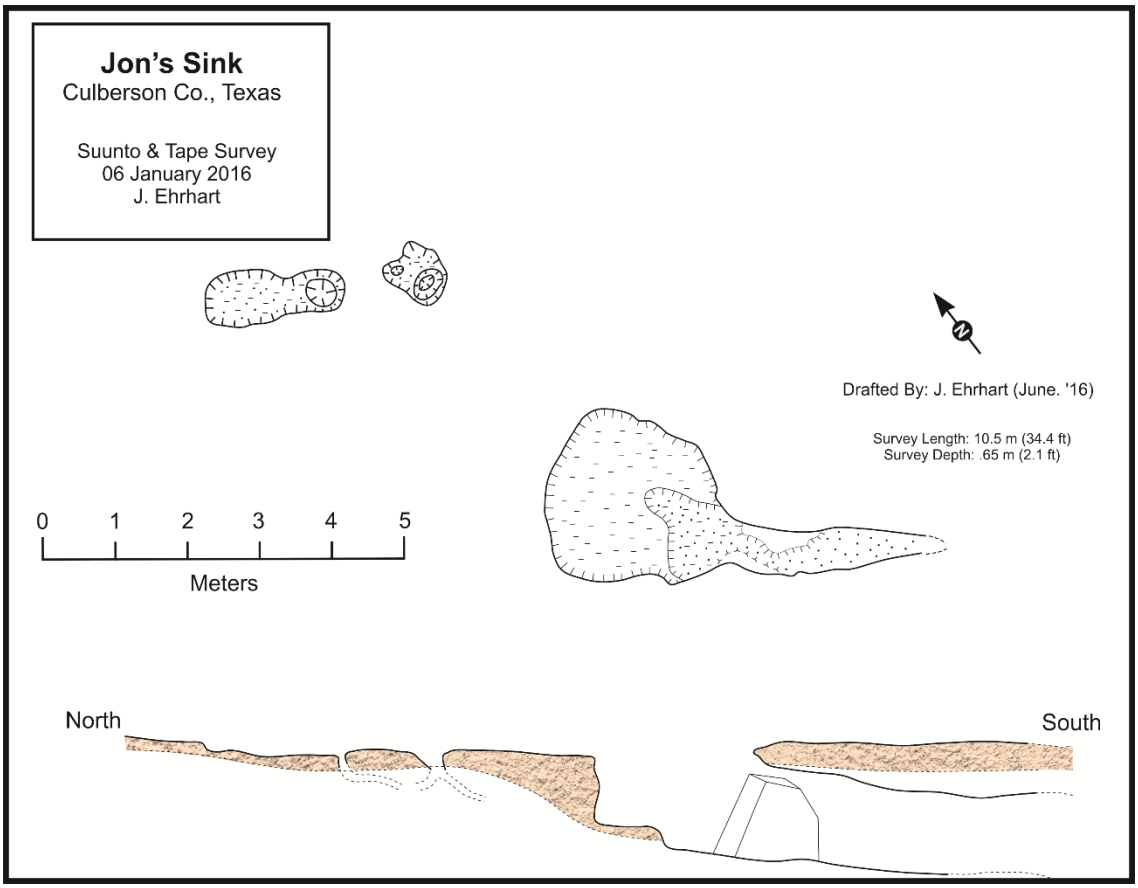

Figure C22: drafted cave map of Jon's Sink Cave.

Jon's Sink Cave is a small dissolution feature that transitions from gypsic soils at the surface into gypsum bedrock in the subsurface. The total survey length is 10.5 meters and survey depth is 0.65 meters. The floor is primarily composed of mud and organic material that is actively piping into lower conduits within the bedrock. This small dissolution feature is another classic

example of epigene erosion and entrenchment where water flows over the land surface until it intersects a descending fracture.

<u>Horizontal Tube Complex</u> (Fig. C23)

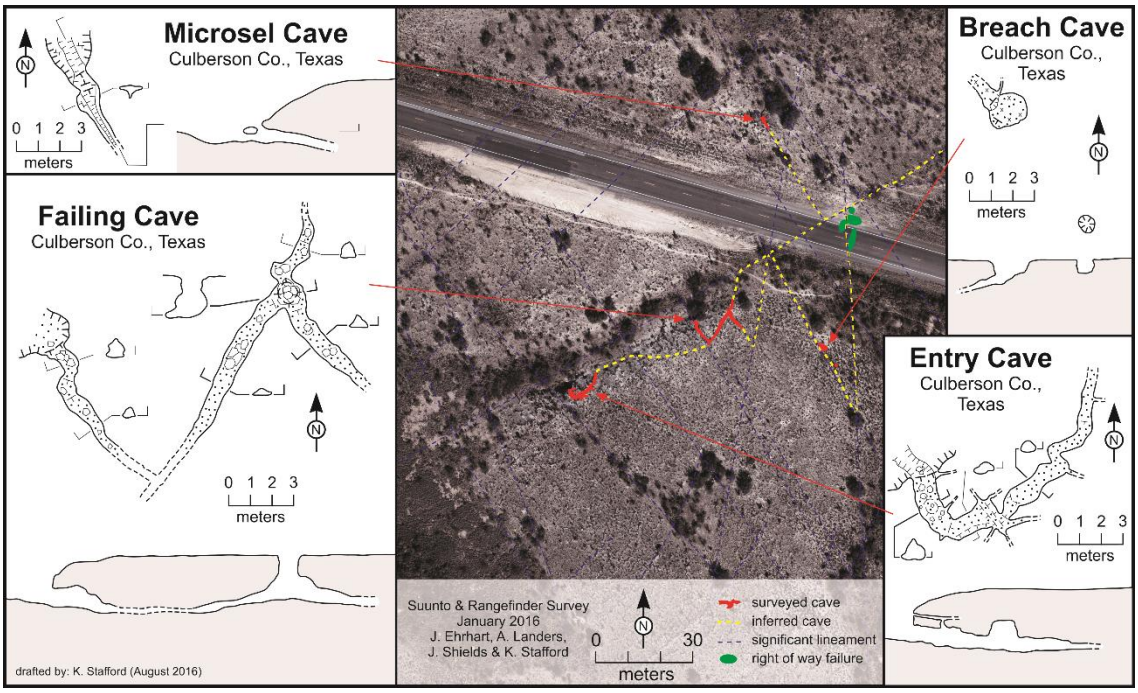

Figure C23: drafted cave map of Horizontal Tube Complex Caves.

The Horizontal Tube Complex is made up of a series of four caves within proximity of RM652. These caves are heavily controlled by the orientation of fractures within the area. They measure to total surveyed length of over 20 meters and depth of 3 meters. The average diameter of cave entrances located within the Horizontal Tube Complex is approximately 0.75 meters. The floor is primarily composed of alluvium and breakdown. The caves within the area are formed by the solutional-widening of fractures within the vadose zone. The presence of closely-spaced, inwardly-pointed scallops indicates that during rain events, high-velocity water rushes through

these passages which further entrenches and widens them. Additionally, the cross-sectional, entrenching morphology further supports the idea that epigene processes formed these caves. The Horizontal Tube Complex also contains many strong lineaments which represent potential locations of additional fracturing and sub-surface conduit development. Road subsidence and fracturing suggest that these conduits likely run under the road and connect at depth.

<u>Fracture Cave Complex</u> (Fig. C24)

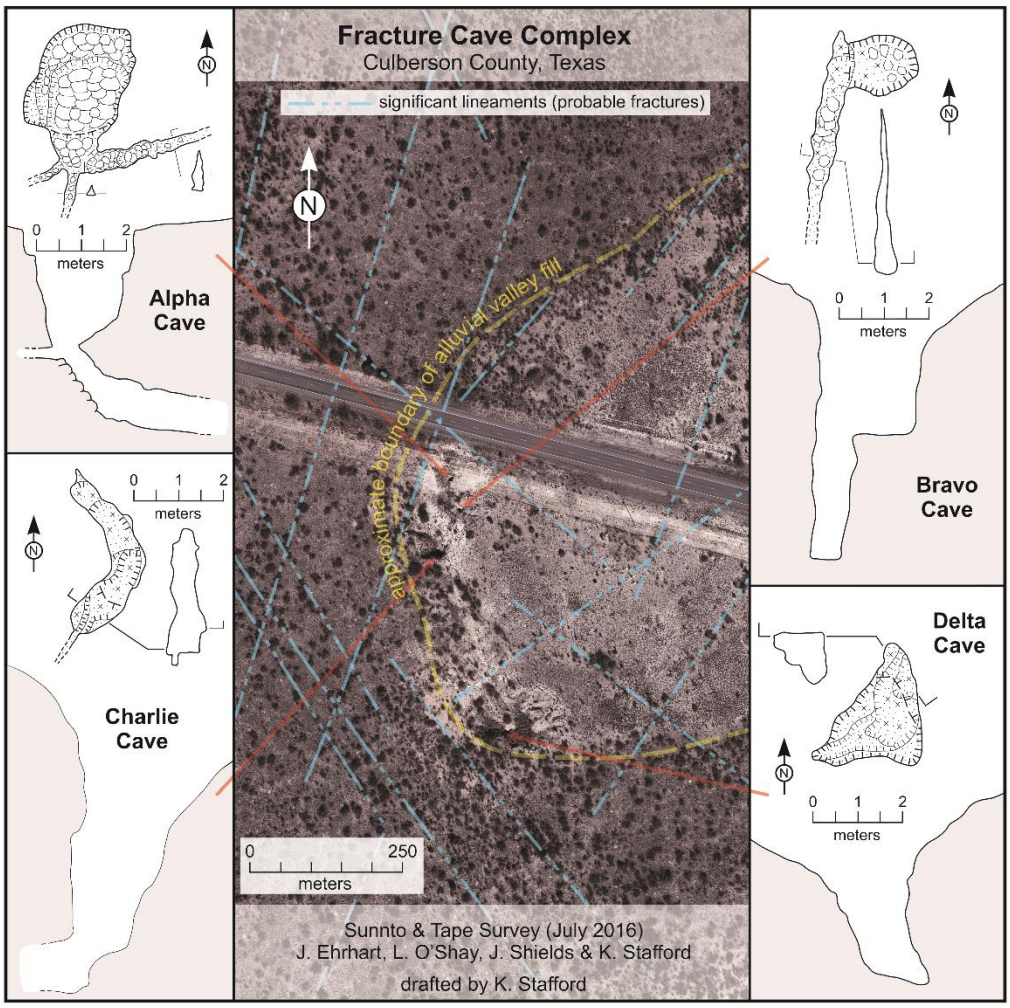

Figure C24: drafted cave map of Fracture Cave Complex.

The Fracture Cave Complex consists of four separate caves that trend in the same direction and follow a similar contact. These caves are located along the periphery of an alluvial valley fill within gypsum bedrock. The slight change in lithology, along with the abundant appearance of fractures, acted as zones where dissolution was accelerated. The surficial expression of these solutionally-widened zones is in the form of an elongated vertical pit that trends along fractures. Comparatively, the total survey length for this complex is merely five meters long while the vertical survey distance is greater than 18 meters tall. This significant variation in vertical to horizontal dissolution rates indicates that these caves likely contain multiple intersecting fractures that allow for accelerated vertical dissolution. As these fractures were solutionally-widened, water began to inject horizontally elongating these pits along the periphery of the alluvial valley fill.

<u>Lidar Density Composite Map</u> (Fig. C25)

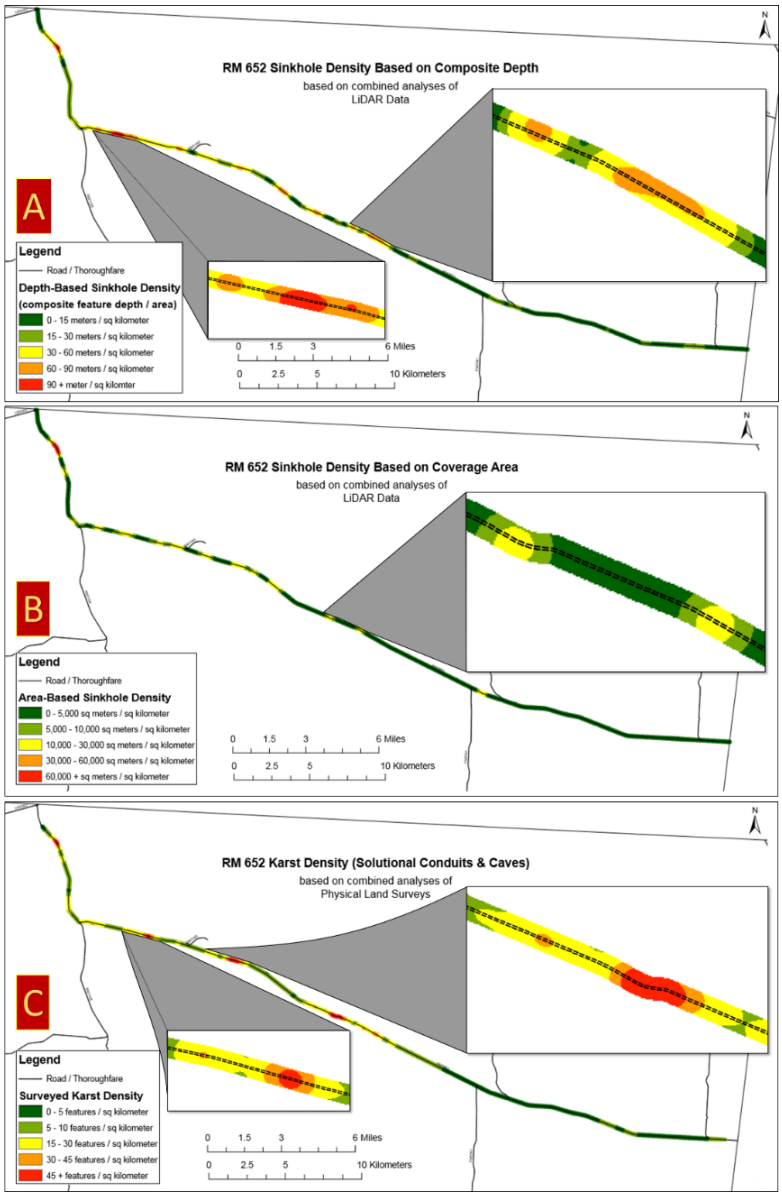

Figure C25: A) – raster map of the spatial density of sinkholes identified through LiDAR analyses that have been proportionally weighted by the maximum depth of individual sinkhole polygons delineated. Density is measured in units of meters per square kilometer. B) raster map of the spatial density of sinkholes identified through LiDAR analyses that have been proportionally weighted by the area of coverage of individual sinkhole polygons delineated. Density is measured in units of square meters per square kilometer. C) raster map of the spatial density of karst features identified through traverse-based surface surveys. Density is measured in units of individual features per square kilometer.

VITA

Jon T. Ehrhart graduated from Colleyville Heritage High School in Colleyville, Texas. In May of 2014, Jon graduated from Stephen F. Austin State University where he received his Bachelor of Science in geology. In June if 2014 he was admitted to the Graduate School of Stephen F. Austin State University and began pursuing his Master of Science degree in Geology. Jon received his Master of Science in Geology in December of 2016.

Permanent Address: 2964 Majestic Oak Dr.
Grapevine, TX 76051

Style manual designation: Geological Society of America

This thesis was typed by Jon T. Ehrhart